

# Study on Particle-based Simulations of Multiphase Flows with Heat and Mass Transfer for Reactor Safety Analysis

Aprianti, Nur Asiah

<https://hdl.handle.net/2324/1470559>

---

出版情報：九州大学，2014，博士（工学），課程博士  
バージョン：  
権利関係：

# **Study on Particle-based Simulations of Multiphase Flows with Heat and Mass Transfer for Reactor Safety Analysis**

**Nur Asiah Aprianti**

# Study on Particle-based Simulations of Multiphase Flows with Heat and Mass Transfer for Reactor Safety Analysis

by

Nur Asiah Aprianti

A thesis submitted for the degree of  
Doctor of Engineering  
in the Division of Engineering  
Kyushu University

Department of Applied Quantum Physics and Nuclear Engineering  
Kyushu University

June 2014

# Contents

Contents.....	i
List of Tables .....	iv
List of Figures .....	v
Chapter 1. Introduction .....	1
1.1. Nuclear energy.....	1
1.2. Generation IV and fast reactor development.....	2
1.3. Core disruptive accident (CDA) and safety design.....	3
1.3.1. FAIDUS concept.....	4
1.4. Safety analysis of fast reactors.....	4
1.5. Particle-based simulation.....	6
1.6. Objective and outline of the preset study.....	8
Chapter 2. Models and Methods of Particle-based Simulations .....	14
2.1. Overview of finite volume particle (FVP) method.....	14
2.2. Governing equations.....	16
2.3. Solution algorithm .....	17
2.3.1. Pressure-based solution algorithm.....	17
2.3.2. Combine and Unified Procedure (CUP) method.....	18
2.4. Boundary conditions.....	19
2.4.1. Wall boundary.....	19
2.4.2. Free surface boundary.....	20
2.5. Viscosity models.....	21
2.5.1. Effective viscosity.....	21
2.5.2. Rheological model.....	22
2.6. Surface tension model.....	23

2.6.1. Surface tension for multiphase flows.....	25
2.7. Heat and mass transfer models.....	26
2.7.1. Conductive heat transfer.....	26
2.7.2. Non-equilibrium model.....	27
2.7.3. Equilibrium model.....	30
2.7.4. Update of conservation equation.....	30
2.8. Buoyancy model.....	32
Chapter 3. Analysis of Early Fuel Discharge Behavior.....	39
3.1. Overview of EAGLE ID-1 test.....	39
3.1.1. Test results.....	39
3.1.2. Posttest analysis.....	40
3.2. Modeling of EAGLE ID-1 test conditions.....	41
3.2.1. Heat and mass transfers.....	41
3.2.2. Viscosity and buoyancy force.....	43
3.2.3. Geometrical conditions.....	44
3.2.4. Initial pool conditions.....	45
3.3. Simulation results of EAGLE ID-1 test.....	46
3.3.1. Effect of fuel crust.....	46
3.3.2. Effect of molten steel.....	48
3.3.3. Crust formation behavior.....	51
3.3.4. Duct wall failure.....	52
3.3.5. Effect of steel droplet size.....	53
3.3.6. Effect of fuel-steel mixing.....	54
3.4. Discussion.....	55
Chapter 4. Analysis of Melt Freezing Behavior.....	80

4.1. Overview of pin bundle experiment.....	80
4.2. Modeling of pin bundle conditions.....	81
4.3. Simulation results and discussions.....	83
4.3.1. Pure-melt freezing.....	83
4.3.2. Mixed-melt freezing.....	84
Chapter 5. Conclusions and Future Works.....	100
Acknowledgement .....	103
Nomenclature .....	105
References .....	109

## List of Tables

Table 1.1-1.....	10
Table 3.2-1.....	59
Table 3.2-2.....	60
Table 3.2-3.....	60
Table 3.3-1.....	61
Table 4.2-1.....	87

## List of Figures

Figure 1.3-1.....	11
Figure 1.3-2.....	12
Figure 1.4-1.....	13
Figure 2.1-1.....	34
Figure 2.3-1.....	34
Figure 2.4-1.....	35
Figure 2.4-2.....	35
Figure 2.5-1.....	36
Figure 2.6-1.....	36
Figure 2.7-1.....	37
Figure 2.7-2.....	37
Figure 2.7-3.....	38
Figure 3.1-1.....	62
Figure 3.2-1.....	63
Figure 3.2-2.....	64
Figure 3.2-3.....	64
Figure 3.3-1.....	65
Figure 3.3-2.....	66
Figure 3.3-3.....	67
Figure 3.3-4.....	68
Figure 3.3-5.....	69
Figure 3.3-6.....	70
Figure 3.3-7.....	71
Figure 3.3-8.....	72



Figure 3.3-9.....	73
Figure 3.3-10.....	74
Figure 3.3-11.....	75
Figure 3.3-12.....	75
Figure 3.3-13.....	76
Figure 3.3-14.....	76
Figure 3.3-15.....	77
Figure 3.3-16.....	77
Figure 3.3-17.....	78
Figure 3.3-18.....	78
Figure 3.4-1.....	79
Figure 4.1-1.....	88
Figure 4.2-1.....	89
Figure 4.3-1.....	90
Figure 4.3-2.....	91
Figure 4.3-3.....	92
Figure 4.3-4.....	93
Figure 4.3-5.....	93
Figure 4.3-6.....	94
Figure 4.3-7.....	95
Figure 4.3-8.....	96
Figure 4.3-9.....	97
Figure 4.3-10.....	97
Figure 4.3-11.....	98
Figure 4.3-12.....	99

# Chapter 1

## Introduction

### 1.1 Nuclear energy

The story of our understanding of nuclear energy began about 2,400 years ago, when ancient Greek conjectured that the world is made of indivisible substances called “atom”. While modern science in 18<sup>th</sup> and 19<sup>th</sup> centuries has shown that matter indeed is composed of atoms, scientists have learned that these atoms are divisible and can be split into separate parts as physicist Enrico Fermi discovered that neutrons could split many kind of atoms. With understanding that atoms could be split to release large amounts of energy, scientists believe a self-sustaining chain reaction might be possible happen. In 1942, Fermi and his group had successfully transformed the scientific theory into technological reality by constructed the world’s first nuclear reactor, Chicago Pile-1, to prove the theory of self-sustaining chain reaction. Most of early nuclear research focused on developing an effective weapon for use in World War II. In order to control nuclear energy development and to explore peaceful uses of nuclear energy, The Atomic Energy Act creates the Atomic Energy Commission (AEC) in 1946. The first electricity power from nuclear energy was experimentally produced in 1951. After intently six years research on this field, the first commercial electricity-generating plant by nuclear energy was constructed in Shippingport, Pennsylvania. The nuclear power industry was grown rapidly after that. However, in the 1970s and 1980s, demand for the electricity decreased due to grew nuclear issues on the Three Mile Island accident and Chernobyl accident, such as reactor safety, waste disposal, and other environmental considerations.

Nuclear energy, which is known as one of environmentally clean and cheap as power electricity source, has become one of promising energy for the future electricity demand. Table 1.1-1 shows the comparison of power generated from different energy sources (Jose, 2012). The applicable of nuclear energy is not only in electricity generation. Its technology has been also applied to many scientific, medical, and industrial purposes.

## **1.2 Generation IV and fast reactor development**

The present operating reactors are mostly considered Generation II, which are based on the first generation of reactors from the 1950s. Some Generation III reactors as evolutionary improvements on Generation II reactors are starting to be operated. The truly revolutionary design that offer significant breakthroughs, especially in safety and efficiency, Generation IV reactors, is under researching and may be commercially available in the years approaching mid-twenty-first. In particular, the Generation IV Forum (GIF) has selected six promising system design; Sodium-cooled fast reactors (SFR), Gas-cooled fast reactors (GFR), Lead-cooled Reactors (LFR), Molten salt reactors (MSR), Supercritical water-cooled reactors (SCWR), and Very high Temperature gas reactors (VHTR).

On fast reactor research, the development of fast breeder reactor (FBR) is now concentrated on the liquid metal-cooled reactor (LMR). Almost a dozen countries have major development and industrialization programs related to the commercialization of LMRs. The development of LMRs has been conducted for more than 60 years.

In Japan, the study for fast reactor began since the first fast reactor Joyo operated in 1977. From its study, several improvements have been applied to Monju, a prototype fast reactor construct in 1991. The application of Monju for the safety research on prevention and mitigation of severe accidents in fast reactor is essential (Sofu, 2012). Additional

safety measures have been employed in Monju as learned lesson from Fukushima accident (Konomura, 2012). In order to against tsunami attack, the Monju plant is placed at 21 m higher than the sea level. In the case of Station Black-Out (SBO), the decay heat is transferred to the air cooler of the secondary cooling system by using the natural convection of sodium in the primary and secondary cooling systems, and the transferred heat is removed from the air cooler by diffusing the heat to atmosphere by air (Takeda, 2012). As for the final stage of these existing fast reactor systems, the safety designs and assessments for the Japanese Sodium-cooled Fast Reactor (JSFR), a commercial fast reactor, have been carried out from the early stage of their development.

Several innovative techniques for the improvement in economics, safety and reliability of JSFR have been developed (Aoto *et al.*, 2011). For the safety and reliability improvement, the ideas are included such as the use of passive reactor shutdown system, the core cooling by natural sodium circulation in case of SBO and the use of special fuel assemblies with inner duct (FAIDUS) to against re-criticality events in case of severe accidents (Takeda, 2012).

### **1.3 Core disruptive accident and safety design**

In the safety assessment of LMRs, core disruptive accidents (CDAs) have played an outstanding role as the LMR core is not designed in the most reactive configuration, although the frequency of CDAs can be made very small. Overheating caused by a serious transient over power and undercooling events in CDAs will lead to formation of multicomponent, multiphase flows of disrupted core materials. The potential scenario and consequences of CDA have been actively studied to prevent such severe accident in the 70s and 80s for LMRs. Figure 1.3-1 describes the simplified path structure of CDA initiator being evaluated in nuclear safety studies. Based on this possible condition, there

are general features of the safety design requirements: 1) Achievement of higher reliability; 2) Achievement of higher inspect-ability and maintainability; 3) Introduction of passive safety features; 4) Reduction of operator action needs; 5) Design consideration against Beyond Design Basis Accidents (BDBA); 6) In-vessel retention of degraded core materials; 7) Prevention and mitigation against sodium chemical reaction; and 8) Design against external events (Kubo *et al.*, 2011).

### *1.3.1 FAIDUS concept*

FAIDUS (Fuel Assembly with Inner Duct System) is a core disruptive accident (CDA) mitigation concept design proposed by JAEA for an advance loop-type SFR, JSFR. This concept design directed to achieve an early accident termination before a large-scale fuel pool formation associated with energetic re-criticality events (Endo *et al.*, 2002; Sato *et al.*, 2011). This FAIDUS concept, as shown in Figure 1.3-2, is one of the design measures for so-called controlled material relocation (CMR). In FAIDUS, where each fuel subassembly is equipped with an inner duct, it is expected that the early failure of the inner duct wall followed by fuel discharge outside of the active core region through the inner duct. This fuel relocation can prevent the formation of critical molten fuel pool, which has a potential of severe energetics due to excessive fuel cohesion initiated by pool sloshing. In order to confirm the concept design capability, an extensive experimental program, the EAGLE (Experimental Acquisition of Generalized Logic to Eliminate re-criticalities) project, has been conducted by Japan Atomic Energy Agency (JAEA) at the facilities of IGR (Impulse Graphite Reactor) in National Nuclear Center (NNC) of Kazakhstan (Konishi *et al.*, 2008). The early fuel removal capabilities of initial FAIDUS were investigated by SIMMER-III and then by our present study on Chapter 3.

## **1.4 Safety analysis of fast reactors**

The evaluation of severe accidents has played an important role in the safety analysis of fast reactors (FRs). In order to provide help in assessing the outcomes of various accident sequences and provide guidance for the future experimental needs and mathematical model development, the computational code to solve complex multi-physics problems, involving molten core behavior, boiling of the coolant, failure of the structure, are strongly necessary. They are two major code used for the evaluation CDA, the SAS4A code and the SIMMER-III code.

The SAS system of accident analysis codes was developed in US at Argonne National Laboratory (ANL) and has played an important role in the assessment of energetics potential for postulated SFR severe accidents. The SAS4A code system is the last generation of this code system used for the analysis of the initiating phase events.

The fast reactor safety analysis code SIMMER-III has been developed and used to analyze CDAs in SFRs (Tobita *et al.*, 2002). SIMMER-III is based on two-dimensional, multi-component, multi-phase, Eulerian description, and thermal-hydraulic interaction among components and phases are modeled using conventional engineering correlation. A conceptual overall framework of SIMMER-III is shown in Figure 1.4-1. The entire code consists of three elements: the fluid-dynamics model, the structure (fuel pin) model, and the neutronics model. The fluid-dynamics portion, which constitutes about two thirds of the code, is interfaced with the structure model through heat and mass transfer at structure surfaces. The neutronics portion provides nuclear heat sources, based on the time-dependent neutron flux distribution in consistent with mass and energy distributions calculated by the other code elements (Kondo *et al.*, 2000).

Although the SIMMER-III calculations might represent macroscopic fluid-dynamics behaviors of multi-component, multi-phase flows reasonably, this code based on the Eulerian method hardly models local and discrete multi-phase flow behaviors involved in

a set of heat transfer processes. On the other hand, particle-based simulations based on a fully Lagrangian framework might be one of the promising computational fluid dynamics (CFD) methods to directly simulate multi-component, multi-phase flows without empirical models such as flow regime map and heat-transfer correlations. This method is more appropriate for fluid-fluid and fluid-solid interphase simulations since the interphases can be clearly represented in calculations compared with conventional Eulerian mesh methods.

### **1.5 Particle-based simulation**

Presently, the moving particle method is widely applied in many fields. They are a wide variety of particle-based simulation method proposed to solve complex multi-physics problems in engineering.

The smoothed particle hydrodynamics (SPH) was originally introduced by Lucy *et al.* (1977) to simulate astrophysical problems including gal axial collisions and the dynamics of star formation. In the SPH method, a spatial distribution of physical quantity is represented by the superposition of kernels that are multiplied by variables retained by the particles. Motion and density of particles are explicitly simulated; pressure is thus explicitly estimated according to particle density. In contrast to Eulerian methods, grid is unnecessary at all and thus there is no numerical diffusion in the SPH method. Fluids are presented as a certain number of moving particles, whose sizes are much larger than a molecule one.

Some review papers by Benz *et al.* (1987) and Monaghan *et al.* (1988) cover the early development of SPH. As a flexible grid less particle method, the original SPH can only solve compressible fluid flow. After the extensive study during the past thirty years, several extensions have been proposed to allow simulation of incompressible fluids with

SPH called incompressible SPH (ISPH). The SPH method has recently been successfully and widely applied to many engineering field problems, including heat and mass transfer, molecular dynamics, and fluid and solid mechanics. Because of success of the SPH method, moving particle methods presently become one of the focuses in CFD researches.

The moving particle semi-implicit (MPS) method (Koshizuka *et al.*, 1995) was originally invented to analyze incompressible viscous fluids with free surface. In the MPS method, a semi-implicit algorithm is employed. The motion of each particle is calculated through interactions with neighboring particles covered with a kernel function. All terms in the govern equations, such as gradient and Laplacian terms, are represented by the deterministic particle interaction models that do not need a mesh. A particle number density, which is the summation of the kernel values of the neighboring particles, is forced to be constant to satisfy the continuity equation. Free surface are detected from the decrease in the particle number density since no particles detected outside the surface. The MPS method has been used successfully in solving many problems, such as the 2D breaking wave, water sloshing in a tank and tracking the free surface (Koshizuka *et al.*, 1996; Wang *et al.*, 2005).

Recently, a new moving particle method for incompressible fluids, which is named as the finite volume particle (FVP) method, was invented (Yabushita and Hibi, 2005). The FVP method is derived based on the finite volume method by assuming that each particle occupies a certain volume. Govern equations of incompressible fluids are discretized on the surface of particle control volume. The FVP method is one of the particle methods in which continuum mechanics is analyzed using concept of particle.

In our group study, the FVP method was extended to analyze complex thermal-hydraulic problems in nuclear engineering. It has been successfully developed and applied to solve free surface flows, convective heat transfer, fluid-solid mixture flow and



gas-liquid flow simulations as well as the phase change model simulation (Zhang *et al.*, 2006; Guo *et al.*, 2010; Mahmudah *et al.*, 2011).

## **1.6 Objective and outline of the present study**

The present study focuses on application of particle-based simulation using the FVP method to the key phenomena in CDAs for detail understandings of thermal-hydraulics behaviors involved in them. They include behaviors of heat transfer from molten pool to structural wall, and melt freezing and blockage formation in a narrow flow channel.

The one of the applications is the analysis of heat transfer behavior from the molten pool of fuel and steel mixture to an adjacent steel wall. The EAGLE-1 ID-1 test experiment was selected in order to evaluate the condition of early fuel discharge in terms of the FAIDUS concept that is one of safety strategies to mitigate severe accident of SFR. Expected mechanism of heat transfer between molten fuel and steel mixture to duct wall was analyzed by the 2D particle-based simulation.

Another application is the analysis of melt freezing experiment in a pin bundle. This was selected in order to clarify local meso-scale freezing and penetration behavior of melt flowing into narrow channel geometry using 3D particle-based simulations in detail. Reasonable evaluation of relocation and freezing of molten core materials is of importance in the safety analysis of LMRs.

In simulating both EAGLE-1 ID-1 test and the melt freezing experiment, the main constitutive models to solve thermal-hydraulic phenomena of multiphase flows were formulated based on the previous works (Guo *et al.*, 2010; Mahmudah, *et al.*, 2011). We employed the viscosity model, the surface tension model, the phase change model and the buoyancy model, of which fundamental validity has been verified, with appropriate

modification and adjustment against specific thermal-hydraulic phenomena involved in the problems.

The present thesis is divided into five chapters. The first chapter focuses on the background and objective of the study. The second chapter explains models and methods of particle-based simulation including overview of the FVP method and the numerical approach to solve mathematical models for multi-component, multi-phase flows. The third chapter describes particle-based simulations on heat transfer behaviors relevant to early fuel discharge observed in EAGLE-1 ID-1 test, including overviews of the previous posttest analysis using the SIMMER-III code. In the fourth chapter, numerical simulations using the FVP method is presented on melt freezing experiments in a seven-pin bundle. Finally, in the fifth chapter, the present study is concluded and some future works are indicated.

Table 1.1-1 Comparison of the power generated from different energy sources

Fuel	Power (kWh)	Amount required (ton a year) for a 1,000 MWe thermoelectricity plant
	generated by 1kg of fuel	
Fuel wood	1	3,400,000
Coal	3	2,700,000
Fuel oil	4	2,000,000
Uranium	50,000	30

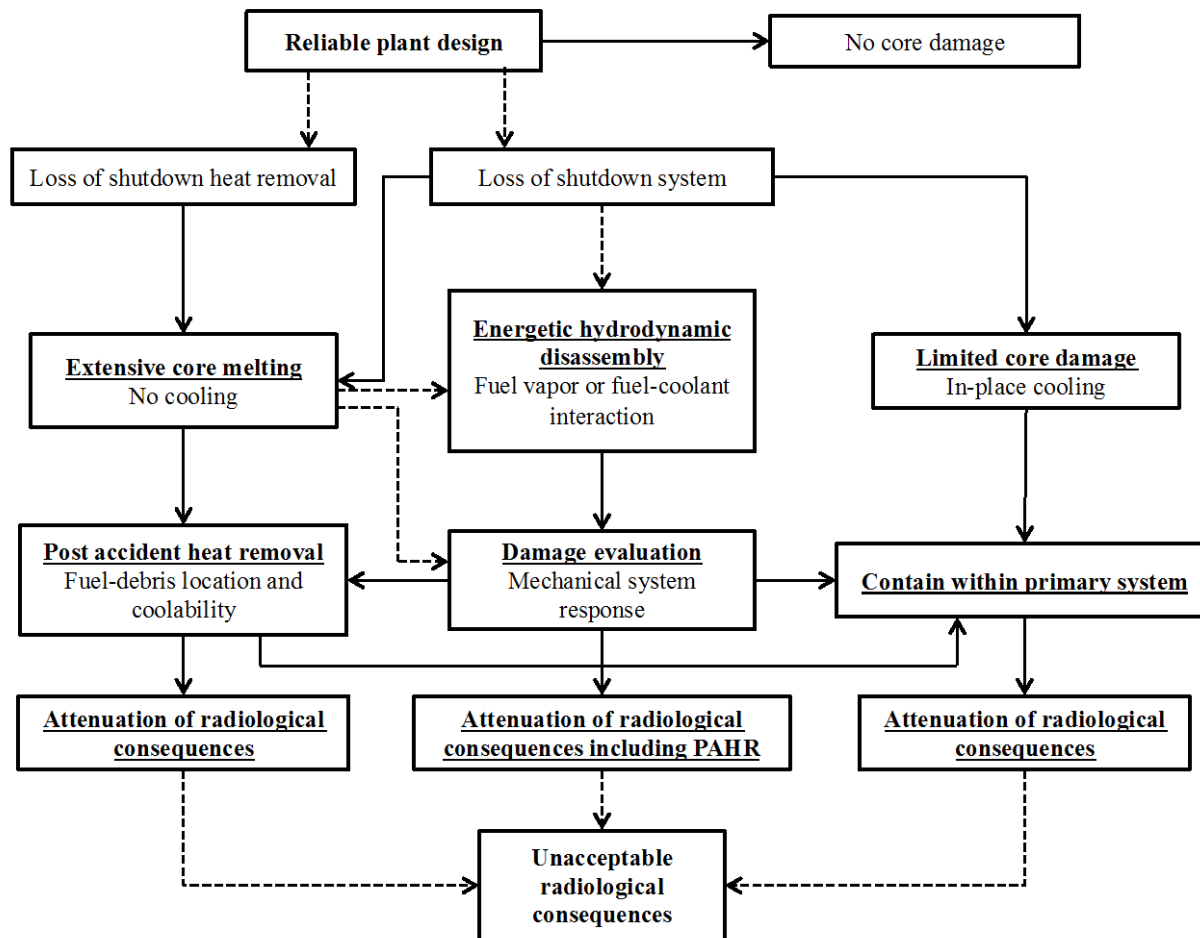


Figure 1.3-1 Simplified of path structure of CDA initiator

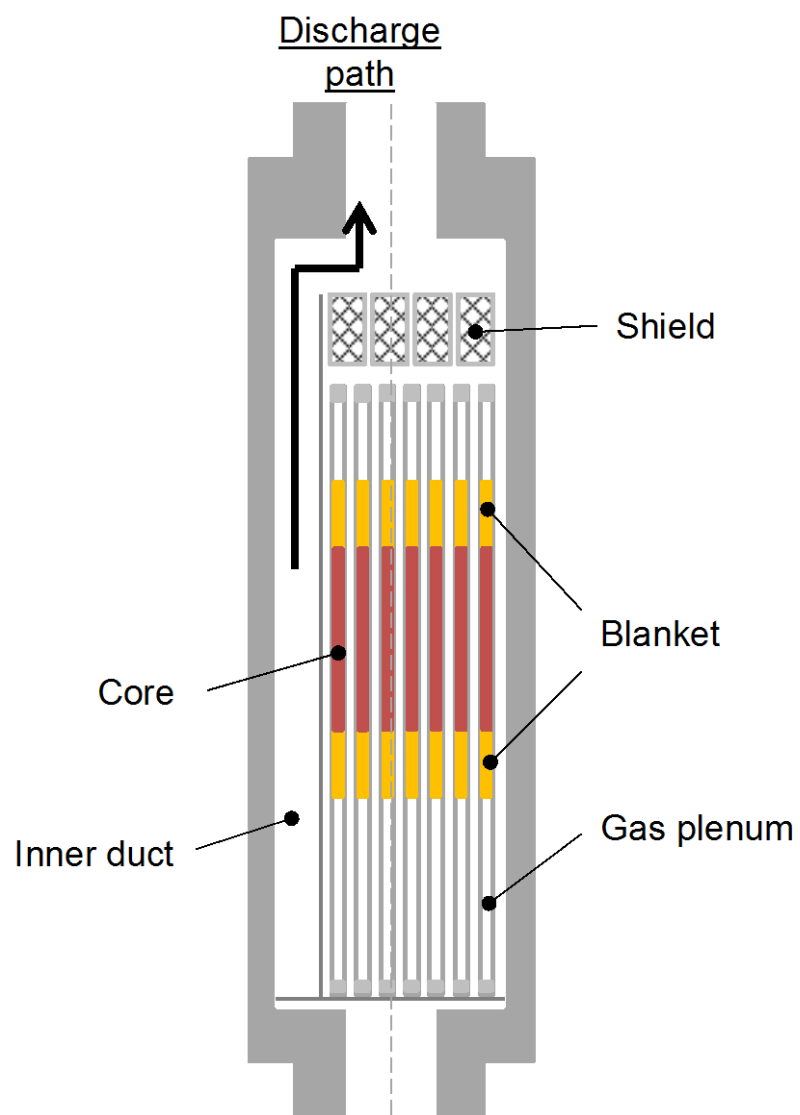


Figure 1.3-2. FAIDUS concept

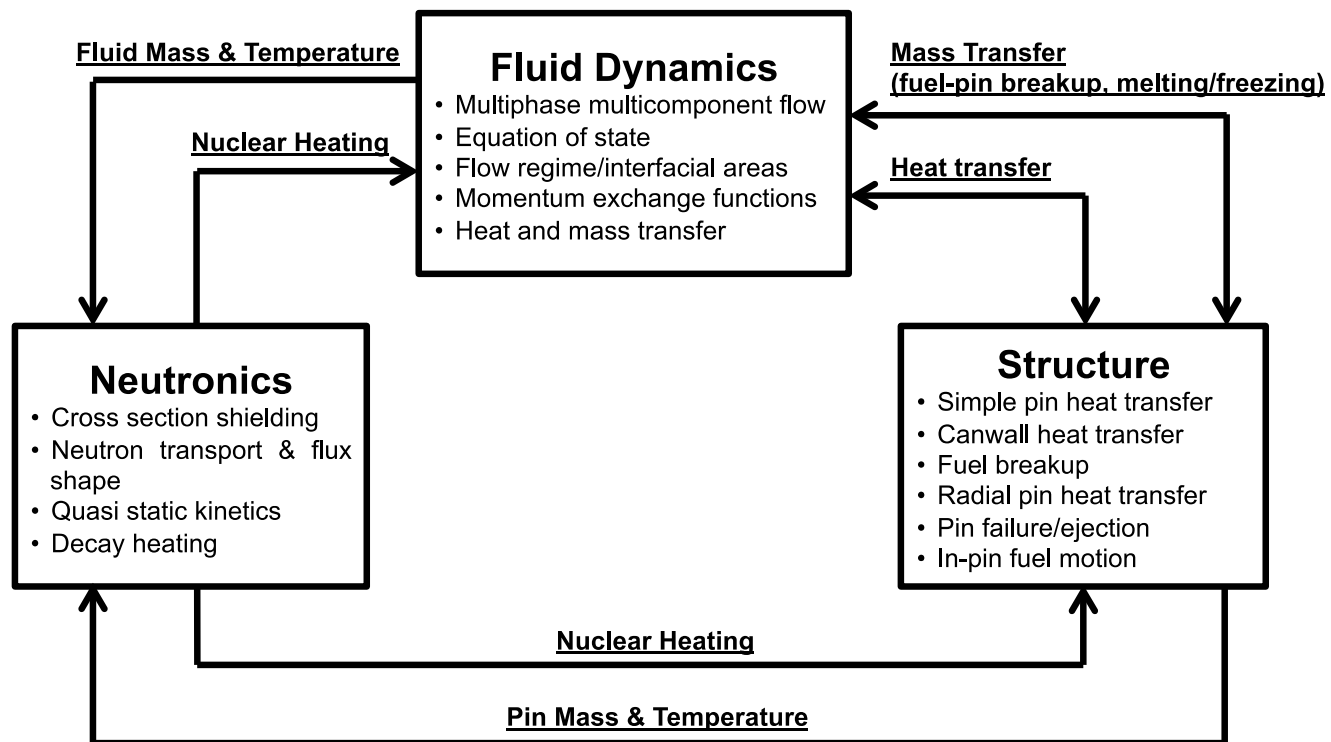


Figure 1.4-1 Overall framework of SIMMER-III code

## Chapter 2

### Models and Methods of Particle Based Simulations

#### 2.1 Overview of finite volume particle (FVP) method

In the FVP method, the calculation domain is represented by a set of discrete numerical particles, which are not only the interpolation points, but also carry the material properties. The velocity and energy of each particle are calculated through interactions with neighboring particles covered with a kernel function. The neighboring particle interactions schematically can be seen in Figure 2.1-1. All terms in governing equations, such as gradient and Laplacian terms, are discretized using a deterministic particle interaction model, which will be simply introduced in the following.

The numerical particles, which are used to discretize governing equations, are assumed to occupy a certain volume, where the control volume of one moving particle is a circle in 2D simulations, and a sphere in 3D simulations:

$$S = 2\pi R, V = \pi R^2 = (\Delta)^2 \quad \text{for 2D} \quad (2.1a)$$

$$S = 4\pi R^2, V = \frac{4}{3}\pi R^3 = (\Delta)^3 \quad \text{for 3D} \quad (2.1b)$$

where  $S$ ,  $V$ ,  $R$  and  $\Delta$  are the particle surface area, the particle control volume, the radius of particle control volume and the initial particle distance, respectively. According to Gauss's law, the gradient and Laplacian operators acting on arbitrary scalar function  $\phi$  are expressed by

$$\nabla \phi = \lim_{R \rightarrow 0} \frac{1}{V} \oint_V \nabla \phi dV = \lim_{R \rightarrow 0} \frac{1}{V} \oint_S \nabla \phi \cdot \bar{n} dS \quad (2.2)$$

$$\nabla^2 \phi = \lim_{R \rightarrow 0} \frac{1}{V} \oint_V \nabla^2 \phi dV = \lim_{R \rightarrow 0} \frac{1}{V} \oint_S \nabla \phi \cdot \bar{n} dS \quad (2.3)$$

where the gradient and Laplacian terms of particle  $\mathbf{i}$  can be approximated as

$$\langle \nabla \phi \rangle_i = \left\langle \frac{1}{V} \oint_S \nabla \phi \bar{n} dS \right\rangle_i = \frac{1}{V} \sum_{j \neq i} \phi_{sur} \cdot \bar{n}_{ij} \cdot \Delta S_{ij} \quad (2.4)$$

$$\langle \nabla^2 \phi \rangle_i = \left\langle \frac{1}{V} \oint_S \nabla \phi \cdot \bar{n} dS \right\rangle_i = \frac{1}{V} \sum_{j \neq i} \left( \frac{\phi_j - \phi_i}{|\bar{r}_{ij}|} \right) \cdot \Delta S_{ij} \quad (2.5)$$

where  $\langle \phi \rangle_i$  is the approximation of  $\phi$  with respect to particle  $\mathbf{i}$  and  $|\bar{r}_{ij}|$  is the distance between particles  $\mathbf{i}$  and  $\mathbf{j}$ , and  $\bar{n}$  is the unit vector. The function value  $\phi_{sur}$  on the surface of particle  $\mathbf{i}$ , can be evaluated using a linear function as

$$\phi_{sur} = \phi_i + \frac{\phi_j - \phi_i}{|\bar{r}_{ij}|} R \quad (2.6)$$

The unit vector  $\bar{n}_{ij}$  of distance between particles  $\mathbf{i}$  and  $\mathbf{j}$  is defined as

$$\bar{n}_{ij} = \frac{\bar{r}_{ij}}{|\bar{r}_{ij}|} = \frac{(\bar{r}_j - \bar{r}_i)}{|\bar{r}_{ij}|} \quad (2.7)$$

The interaction surface  $\Delta S_{\bar{y}}$  between particle  $\mathbf{i}$  and particle  $\mathbf{j}$ , can be estimated as

$$\Delta S_{\bar{y}} = \frac{\omega_{\bar{y}}}{\sum_{j \neq i} \omega_{\bar{y}}} S \quad (2.8)$$

where  $\omega_{\bar{y}}$  is the kernel function. It can be defined as

$$\omega_{ij} = \begin{cases} \sin^{-1} \left( \frac{R}{|\bar{r}_{ij}|} \right) - \sin^{-1} \left( \frac{R}{r_e} \right) & |\bar{r}_{ij}| \leq r_e \\ 0 & |\bar{r}_{ij}| \geq r_e \end{cases} \quad (2.9)$$

where  $r_e$  is the cut-off radius, which is chosen as 4.1  $\Delta$  for 2D system and 2.1  $\Delta$  for 3D system. This cut-off radius is used to define the limitation area of neighboring



particles around particle  $i$ . Through these neighboring fluid particle interactions, the fluid movement and heat and mass transfer are modeled.

## 2.2 Governing equations

The governing equations to be solved for incompressible fluids are the following Navier-Stokes equation, the continuity equation and energy equation:

$$\rho \frac{D\vec{u}}{Dt} = -\nabla p + \nabla(\mu \nabla \cdot \vec{u}) + \vec{f} \quad (2.10)$$

$$\nabla \cdot \vec{u} = 0 \quad (2.11)$$

$$\rho \frac{DH}{Dt} = \nabla \cdot (k \nabla T) + Q \quad (2.12)$$

where  $\rho$  is the density,  $\vec{u}$  is the velocity,  $t$  is the time,  $p$  is the pressure,  $\mu$  is the dynamic viscosity,  $H$  is the specific enthalpy,  $k$  is the thermal conductivity and  $T$  is the temperature. The third term  $\vec{f}$  in the right-hand side of Eq. (2.10) represents other forces per unit volume, such as surface tension and gravity. The second term  $Q$  in the right-hand side of Eq. (2.12) includes heat and energy transfer rate at the interface between different phases and volumetric heat sources.

The integral forms of Eqs. (2.10), (2.11) and (2.12), respectively, are

$$\frac{D}{Dt} \int_V \vec{u} dV = -\frac{1}{\rho} \oint_S p \cdot \vec{n} dS + \frac{1}{\rho} \oint_S (\mu \nabla \cdot \vec{u}) \cdot \vec{n} dS + \int_V \vec{f} dV \quad (2.13)$$

$$\oint_S \vec{u} \cdot \vec{n} dS = 0 \quad (2.14)$$

$$\frac{D}{Dt} \int_V \rho e dV = \oint_S (k \nabla T) \cdot \vec{n} dS + \int_V Q dV \quad (2.15)$$

By using the same approach as the FVP method described in Section 2.1, the integral form of Navier-Stokes equation, Eq. (2.13), can be discretized as

$$\left(\frac{D\bar{u}}{Dt}\right)_i = -\frac{1}{\rho\pi R^2} \sum_{j=1, j \neq i} \left( p_i + \frac{p_j - p_i}{|\bar{r}_{ij}|} R \right) \Delta \bar{S}_{ij} + \frac{\nu}{\pi R^2} \sum_{j=1, j \neq i} \frac{|\bar{u}_j - \bar{u}_i|}{|\bar{r}_{ij}|} |\Delta \bar{S}_{ij}| + \bar{f} \quad (2.16)$$

## 2.3 Solution algorithm

### 2.3.1 Pressure based solution algorithm

There are several solution algorithms to solve the Navier-stokes equation. In the original FVP method, the pressure implicit with splitting operators (PISO) algorithm (Issa, 1985), which is a pressure based fully implicit algorithm, is used to solve the equation. The disadvantage of the PISO algorithm is that it consumes a lot of computation time. In the present study, for time efficiency, an explicit-implicit algorithm was adopted to solve the Navier-Stokes equation.

The flowchart of the explicit-implicit algorithm can be seen in Figure 2.3-1. In the explicit step, particle's velocity is explicitly updated with the viscosity, surface tension and external forces as

$$\bar{u}^* = \bar{u}^n + \Delta t \left[ \frac{1}{\rho} \nabla \hat{\mu} \cdot \nabla \bar{u}^n + \frac{\hat{\mu}}{\rho} \nabla^2 \bar{u}^n + \bar{g} + \bar{f}^n \right] \quad (2.17)$$

where  $\Delta t$  is the time step width. Then particle's position is also explicitly updated as

$$\bar{r}^* = \bar{r}^n + \Delta t \bar{u}^* \quad (2.18)$$

In the next step, particle's velocity is implicitly updated with the solved pressure equation as

$$\bar{u}^{n+1} = \bar{u}^* - \Delta t \frac{1}{\rho} \nabla p^{n+1} \quad (2.19)$$

Then finally, particle's position is also updated as

$$\bar{r}^{n+1} = \bar{r}^n + \Delta t \bar{u}^{n+1} \quad (2.20)$$

### 2.3.2 Combined unified procedure method

To solve the pressure Poisson equation, the combined unified procedure (CUP) method is introduced to the FVP method. The key of CUP method is linking the changes in pressure and density by introducing a sound speed and deducing an implicit expression for the pressure (Xiao et al, 1997). From the continuity equation, it can be derived as

$$\frac{D\rho}{Dt} = -\rho \nabla \cdot \bar{u} \quad (2.21)$$

It can be further arranged as

$$\nabla \cdot \bar{u} = -\frac{1}{\rho} \frac{D\rho}{Dt} = -\frac{1}{\rho} \frac{\partial \rho}{\partial p} \frac{Dp}{Dt} - \frac{1}{\rho} \frac{\partial \rho}{\partial e} \frac{De}{Dt} \quad (2.22)$$

where  $e$  is the internal energy. For the incompressible flows, by assuming there are no heat conduction and dissipation, the differential form of internal energy is become

$$\frac{De}{Dt} = 0 \quad (2.23)$$

In addition, it is known that the sound speed can be calculated as

$$c_{sound}^2 = \frac{\partial p}{\partial \rho} \quad (2.24)$$

Therefore, by combining Eqs. (2.21) and (2.24), we can obtain the following equation

$$\nabla \cdot \bar{u} = -\frac{1}{\rho c_{sound}^2} \frac{Dp}{Dt} \quad (2.25)$$

that can also be expressed by

$$\nabla \cdot \bar{u}^{n+1} = -\frac{1}{\rho c_{sound}^2} \frac{p^{n+1} - p^n}{\Delta t} \quad (2.26)$$

with  $c_{sound}^2$  is the smoothed square value of the sound speed. While Eq. (2.19) can be rewritten as the following

$$\nabla \cdot \vec{u}^{n+1} = \nabla \cdot \vec{u}^* - \nabla \cdot \left[ \Delta t \frac{1}{\rho} \nabla p^{n+1} \right] \quad (2.27)$$

The pressure equation can be obtained by combining Eqs. (2.26) and (2.27) that expressed as

$$-\frac{1}{\rho c_{sound}^2} \frac{p^{n+1} - p^n}{\Delta t} = \nabla \cdot \vec{u}^* + \frac{\Delta t}{\rho^2} \nabla \rho \cdot \nabla p^{n+1} - \frac{\Delta t}{\rho} \nabla^2 p^{n+1} \quad (2.28)$$

In order to obtain a symmetrical formulation, Eq. (2.28) can be rearranged into

$$-\frac{1}{\rho c_{sound}^2} \frac{p^{**} - p^*}{\Delta t} = \nabla \cdot \vec{u}^* + \frac{\Delta t}{\rho^2} \nabla \rho \cdot \nabla p^* - \frac{\Delta t}{\rho} \nabla^2 p \quad (2.29)$$

where  $p^*$  is initially set to be equal to  $p^n$ , and  $p^{**}$  is solved with the above equation. The value of  $p^{**}$  is then given to  $p^*$  and Eq. (2.28) is solved again. As a result, iteration is generated. After convergent,  $p^{**}$  is equal to  $p^*$ , and this value is given to  $p^{n+1}$  and can be solved by the Incomplete Cholesky Conjugate Gradient (ICCG) algorithm (Ajiz M. A. and Jennings A., 1984).

## 2.4 Boundary condition

It is necessary to consider how to represent the boundary conditions in the FVP method, since the cut off radius would not be comparable with geometry boundaries. In the present study, wall boundary and free surface boundary that are implemented into the system will be described in the following.

### 2.4.1 Wall boundary

In the present study, the virtual or dummy particles are utilized to provide the flexibility of direct application of the Dirichlet and Neumann conditions to the boundary, which are required by a physical problem. The particles are generated by reflecting fluid particles to the wall. Hence no need to present fixed outer particles in order to satisfy the

number of density calculation of wall and nearby fluid particles. Fluid particles interact with wall particles, dummy particles and other fluid particles that are in its support domain according to the cut-off radius. The illustration of this treatment can be seen in Figure 2.4-1.

#### 2.4.2 Free surface boundary

Particle contacting in the free surface is estimated with the following equation, which is discretization form of Poisson equation:

$$\begin{aligned} & \frac{1}{\rho_i} \sum_{j=1, j \neq i} \frac{p_j - p_i}{|\vec{r}_{ij}|} |\Delta \vec{S}_{ij}| + \frac{p_{free} - p_i}{\rho R} |\Delta \vec{S}_{free}| \\ &= \frac{1}{\Delta t} \sum_{j=1, j \neq i} \left( \vec{u}_i + \frac{\vec{u}_j - \vec{u}_i}{|\vec{r}_{ij}|} R \right) \cdot \Delta \vec{S}_{ij} + \frac{1}{\Delta t} \left[ \vec{u}_i + \left( \frac{\partial \vec{u}}{\partial n} \right)_{free} R \right] \cdot \Delta \vec{S}_{free} \end{aligned} \quad (2.30)$$

where  $p_{free}$  is the pressure on the free surface, and  $\left( \frac{\partial \vec{u}}{\partial n} \right)_{free}$  is the velocity gradient on the free surface.

By the approximation of the zero Dirichlet and homogenous Neumann conditions for pressure  $p_{free}$  and velocity divergence  $\left( \frac{\partial \vec{u}}{\partial n} \right)_{free}$ , respectively, Eq. (2.30) will be

$$\frac{1}{\rho} \sum_{j=1, j \neq i} \left( \frac{p_j - p_i}{|\vec{r}_{ij}|} \right) |\Delta \vec{S}_{ij}| - \frac{p_i}{\rho R} |\vec{S}_{free}| = \frac{1}{\Delta t} \sum_{j=1, j \neq i} \left( \vec{u}_i + \frac{\vec{u}_j - \vec{u}_i}{|\vec{r}_{ij}|} R \right) \cdot \Delta \vec{S}_{ij} + \frac{1}{\Delta t} \vec{u}_i \cdot \vec{S}_{free} \quad (2.31)$$

where the vector  $\vec{S}_{free}$  is referred to the interaction surface on free surface that can be calculated as follows:

$$\vec{S}_{free} = - \sum_{j \neq i} \Delta S_{ij} \cdot \vec{n}_{ij} \quad (2.32)$$

Thus, the Laplacian and gradient of the pressure, as well as the divergence of the velocity for the particles on the free surface, can be expressed as

$$\nabla^2 p_i = \frac{1}{V} \left( \sum_{j \neq i} \frac{p_j - p_i}{|\vec{r}_{ij}|} \Delta S_{ij} - \frac{p_i}{R} |\vec{S}_{free}| \right) \quad (2.33)$$

$$\nabla p_i = \frac{1}{V} \left( \sum_{j \neq i} \frac{p_j + p_i}{2} \vec{n}_{ij} \Delta S_{ij} + \frac{p_i}{2} \vec{S}_{free} \right) \quad (2.34)$$

$$\nabla \cdot \vec{u}_i = \frac{1}{V} \left( \sum_{j \neq i} \left( \vec{u}_i + \frac{\vec{u}_j - \vec{u}_i}{|\vec{r}_{ij}|} R \right) \cdot \vec{n}_{ij} \Delta S_{ij} + \vec{u}_i \cdot \vec{S}_{free} \right) \quad (2.35)$$

The treatment of the boundary condition for particle  $i$  lying on the free surface is shown by Figure 2.4-2.

## 2.5 Viscosity models

Choosing an appropriate viscosity model could help to deal with velocity suppression when liquid particles become solid. This is because the Navier-Stokes equation is being solved for the whole domain, thus a special treatment is needed to make solidified particle velocity simulated more reasonably in the system. The simplest and most straightforward approach is to assign the particle velocity to zero when its temperature is below the solidification or solid temperature (Usmani *et al.*, 1992). Another method is to set the viscosity as a function of fluid temperature (Voller, 1987). If liquid turns into solid, the viscosity increases to a large value, which suppresses the velocity. There are many viscosity-temperature equations to be chosen from a lot of literature. In the present study two types of viscosity models are described as implemented in our simulations; a theoretical effective viscosity model based on solid fraction and a rheology model based on material enthalpy.

### 2.5.1 Effective viscosity

The theoretical model for effective viscosity (Frankel N. A. and Acrivos A., 1967) is described by

$$\frac{\mu_{eff}}{\mu_0} = \begin{cases} 1 + 2.5\alpha + 6.2\alpha^2 & \text{for } 0 < \alpha < 0.3 \\ \frac{9}{8} \frac{(\alpha / \alpha_{max})^{1/3}}{1 - (\alpha / \alpha_{max})^{1/3}} & \text{for } 0.3 < \alpha < \alpha_{max} \end{cases} \quad (2.36)$$

where  $\mu_0$  is viscosity of the medium,  $\mu_{eff}$  is effective viscosity,  $\alpha$  is volume/packing fraction of solid phase, and  $\alpha_{max}$  is the maximum volume/packing fraction of solid phase. In the present 2D simulations, the values for  $\alpha_{max}$  was chosen as 0.9. This above equation yields very large viscosity as  $\alpha$  approaches to  $\alpha_{max}$ .

### 2.5.2 Rheological model

Figure 2.5-1 shows the rheological model present in this section. Guo *et al.* (2010) proposed an empirical law to approximate viscosity changes during melting and solidification, which has been used to study rheological phenomena as

$$\mu_{app,i} = \min \left\{ \mu_{max}, \mu_i \exp \left[ - \frac{A(H_i - H_{liq})}{C_p} \right] \right\} \quad (2.37)$$

where  $\mu_{app,i}$  is the dynamic viscosity of particle  $i$  during melting and solidification,  $H_{liq}$  is the specific enthalpy at the liquidus point,  $H_i$  is the specific enthalpy of particle  $i$ ,  $A$  is the rheology parameter to be adjusted by experimental data with unit of  $K^{-1}$ , and  $C_p$  is the specific heat capacity. The upper limit value  $\mu_{max}$  is introduced to maintain numerical stability:

$$\mu_{max} = \mu_{liq} \exp \left[ - \frac{A(H_{\alpha=0.375} - H_{liq})}{C_p} \right] \quad (2.38)$$

where  $\mu_{liq}$  is the viscosity at the liquidus point and  $H_{\alpha=0.625}$  is the enthalpy at the solid volume fraction of 0.625. This was obtained from experimental results in the previous work (Thomas, 1965).

In simulation of melt flow with freezing, the melt rheological behavior has obvious influences on solid and fluid dynamics. They are considered as an increase in viscosity simply. In the present study, the apparent viscosity was reformulated as the following empirical equation, which is a similar one as described above:

$$\mu_{app,i} = \min[\mu_{max}, \mu_l \exp(-A' \alpha_i)] \quad (2.39)$$

where  $A'$  is the dimensionless model parameter. The solid volume fraction  $\alpha_i$  of particle  $i$  is defined as

$$\alpha_{s,i} = \min \left\{ 1.0, \max \left[ 0.0, \frac{(H_{liq} - H_i)}{H_f} \right] \right\} \quad (2.40)$$

where  $H_f$  is the latent heat of fusion.

In the present simulations, we assume that all numerical particles expect for those representing static structures are governed by Eq. (2.11) with  $\mu_{app,i}$  instead of  $\mu_i$ . To maintain numerical stability, the same upper limit value as Eq. (2.38) is used for  $\mu_{app,i}$ :

$$\mu_{max} = \mu_{liq} \exp(-A' \alpha_{max}) \quad (2.41)$$

where  $\alpha_{max}$  ( $= 0.625$ ) is the maximum solid volume fraction that yields the upper limit of  $\mu_{app,i}$ .

## 2.6 Surface tension model

In the present study an efficient and easily applied model based on the free surface energy for moving particle method simulation (Kondo *et al.*, 2007) were applied to the systems. The schematic description of the surface free energy between two blocks A and B is shown in Figure 2.6-1. In this model, the energy needed to separate blocks A and B is equal to



$$\Phi_{free} = \frac{1}{2} \sum_{i \in A, j \in B} E(|\vec{r}_{ij}|) \quad (2.42)$$

where  $\Phi_{free}$  is surface free energy and  $E(|\vec{r}_{ij}|)$  is potential energy between particle  $i$  and its neighbors. The potential energy itself can be modeled as

$$E(|\vec{r}_{ij}|) = C_l e(|\vec{r}_{ij}|) \quad (2.43)$$

where

$$e(|\vec{r}_{ij}|) = \begin{cases} \frac{1}{3} \left( |\vec{r}_{ij}| - \frac{3}{2} \Delta l + \frac{1}{2} r_e \right) \left( |\vec{r}_{ij}| - r_e \right)^2 & |\vec{r}_{ij}| < r_e \\ 0 & |\vec{r}_{ij}| > r_e \end{cases} \quad (2.44)$$

As we know that the surface tension coefficient  $\sigma$  is defined as

$$\sigma_l = \frac{\partial \Phi_{free}}{\partial S} \quad (2.45)$$

By combine Eqs. (2.42) and (2.45), the parameter  $C$  for liquid-liquid particles contact can be defined as

$$C_l = 2 \frac{(\Delta l)^2}{\sum_{i \in A, j \in B} e(|\vec{r}_{ij}|)} \sigma_l \quad (2.46)$$

where

$$\sigma_l = \begin{cases} \sigma_a + \sigma_b - 2\sqrt{\sigma_a \sigma_b} & \text{material } a \neq \text{material } b \\ \sigma_a = \sigma_b & \text{material } a = \text{material } b \end{cases} \quad (2.47)$$

Equation (2.47) can be used for limited three phases that are all nonpolar (Carey, 2008).

Finally, the interaction forces between two particles due to the potential energy can be calculated as

$$\vec{f}_{ij} = -\frac{1}{\rho(\Delta l)^3} \frac{\partial E(|\vec{r}_{ij}|)}{\partial(|\vec{r}_{ij}|)} \vec{r}_{ij} \quad (2.48)$$

As a result, the surface tension force acting on particle  $i$  can be calculated as

$$\vec{f}_{i,tension} = \sum_{j \neq i} \vec{f}_{ij} \quad (2.49)$$

A smoothing algorithm was proposed to overcome the numerical instability problem in simulating the surface tension force using the present model when particles positions were irregular (Kondo *et al.*, 2007):

$$\vec{f}_{i,tension}^{smooth} = \vec{f}_i + C_{smooth} \frac{d}{n^0} \sum_{j \neq i} \frac{(\vec{f}_{j,tension} - \vec{f}_{i,tension}) \cdot \vec{r}_{ij}}{|\vec{r}_{ij}|^2} \vec{r}_{ij} w_{ij} \quad (2.50)$$

where  $C_{smooth}$  is the tuning parameter and set to be 1.0 in the present simulations.

### 2.6.1 Surface tension for multi-phase flows

The surface tension coefficient  $\sigma_l$  between liquid-liquid particles and  $\sigma_{ls}$  between solid-liquid particles are defined by Young equation (Joly *et al.*, 1976):

$$\sigma_s - \sigma_{ls} - \sigma_l \cdot \cos \theta = 0 \quad (2.51)$$

where  $\theta$  is the contact angle between solid-liquid particles. Equation (2.46), can be rearranged as

$$\frac{2\sigma_l}{C_l} = \frac{\sum e(|\vec{r}_{ij}|)}{(\Delta l)^2} \quad (2.52)$$

and the surface tension coefficient between solid-liquid particles can be calculated as

$$\sigma_s + \sigma_l - \sigma_{ls} = \frac{\sum e(|\vec{r}_{ij}|)}{(\Delta l)^2} C_{ls} \quad (2.53)$$

Therefore, by combining Eqs. (2.51), (2.52) and (2.53), the function parameter  $C_{ls}$  between solid-liquid particles can be calculated by

$$C_{ls} - \frac{C_l}{2} (1 + \cos \theta) = 0 \quad (2.54)$$

where the contact angle  $\theta$  varies depending on materials contact. For example, in case of steel material in contact UO<sub>2</sub> material, the contact angle  $\theta$  itself vary between 60° (wetting) – 120° (non-wetting). In the present study, the contact angle  $\theta$  set as 120° for the solid-liquid particles contact in accordance with non-wetting conditions of steel-UO<sub>2</sub> contact.

## 2.7 Heat and mass transfer model

In the present study, the heat and mass transfer processes of materials are modeled as non-equilibrium and equilibrium transfers as well as heat conduction. The governing equation to be solved in this module is the energy equation as described in Eq. (2.12). Phase changes occurring at interfaces between two different materials or between two different phases are modeled as a non-equilibrium process because the bulk temperature does not generally satisfy the phase-change condition when the mass transfer occurs at the interface (Mahmudah *et al.*, 2011). On the other hand, the equilibrium process of melting or freezing occurs when the bulk energy of the phase satisfies the phase-change condition (Guo *et al.*, 2010).

### 2.7.1 Conductive heat transfer

Using the Laplacian model of the FVP method, the conductive heat transfer for the particle  $i$  is approximated as

$$\left[ \nabla \cdot (k \nabla T) \right]_i = \frac{1}{V} \sum_{j \neq i} k_{ij} \frac{T_j - T_i}{|\vec{r}_{ij}|} \Delta S_{ij} \quad (2.55)$$

In Eq. (2.55), the effective thermal conductivity  $k_{ij}$  between particles  $i$  and  $j$  is given by

$$k_{ij} = \frac{2k_i k_j}{k_i + k_j} \quad (2.56)$$

where  $k_i$  is the thermal conductivity of particle  $i$ . Equation (2.55) should be applied to the conductive heat transfer between particles with a same material and phase.

### 2.7.2. Non-equilibrium model

The basic concept of the non-equilibrium mass transfer model is described in a binary contact interface of the energy particles  $i$  and  $j$  as shown in Figs. 2.7-1 and 2.7-2. This model is a heat transfer-limited process where the phase transition rate is determined from energy balance at the interface (Morita K., 1998). Detail explanations of this model are described in the following A and B sections.

#### A. Interfacial heat transfer

The term  $Q^h$  is modeled to calculate the heat transfer at the interface between particles with different materials or phases. The heat transfer rate from the interface between particles  $i$  and  $j$  to particle  $i$  and particle  $j$  are formulated as

$$Q_{i,j}^h = \alpha_{ij} h_i (T_{ij}^I - T_i) \quad (2.57)$$

$$Q_{j,i}^h = \alpha_{ij} h_j (T_{ij}^I - T_j) \quad (2.58)$$

where  $\alpha_{ij}$  is the heat transfer area per unit volume between particle  $i$  and  $j$ ,  $h_i$  is the heat transfer coefficient of particle  $i$ ,  $h_j$  is the heat transfer coefficient of particle  $j$  and  $T_{ij}^I$  is the temperature of the interface between particles  $i$  and  $j$ . For particle  $i$ , the term  $Q^h$  is calculated as

$$[Q^h]_i = \sum_{j \neq i} Q_{i,j}^h \quad (2.59)$$

In 2D systems,  $\alpha_{ij}$ , which is defined as binary contact area per unit volume between particles  $i$  and  $j$ , is calculated as

$$a_{ij} = \begin{cases} \frac{\Delta l}{V} & \text{for } \frac{|\bar{r}_{ij}| - \Delta l}{\Delta l} \leq \delta \\ 0 & \text{otherwise} \end{cases} \quad (2.60)$$

where  $\delta$  is the model parameter, which measures the binary contact between particles  $i$  and  $j$ .

Although  $h_i$  should be modeled so as to represent effective heat transfer depending on flow conditions, it is simply approximated as

$$h_i = \frac{2k_i}{\Delta l} \quad (2.61)$$

where  $k_i$  the thermal conductivity of the solid and liquid mixture is calculated by

$$k_i = \alpha_{s,i} k_s + (1 - \alpha_{s,i}) k_l \quad (2.62)$$

The fraction of solid phase in particle  $i$  given by

$$\alpha_{s,i} = \frac{m_{s,i}}{m_{s,i} + m_{l,i}} = \frac{m_{s,i}}{m_i} \quad (2.63)$$

where  $m_{s,i}$  and  $m_{l,i}$  are the solid and liquid mass of particle  $i$ , respectively, and  $m_i$  is the mass of particle  $i$ .

The interface temperature  $T_y^I$  should be the phase change temperature when occurrence of phase change is predicted at the interface. The phase change processes occurring at the interfaces are called non-equilibrium transfers because the bulk conditions of a particle are generally not at the phase-change temperature. If particles  $i$  and  $j$  consist of the same material,  $T_y^I$  can be expressed by

$$T_y^I = \min[T_{liq,M(i)}, \max(T_{ij}^N, T_{sol,M(i)})] \quad (2.64)$$

where  $T_{sol,M(i)}$  and  $T_{liq,M(i)}$  are the solidus and liquidus temperatures of the material that constitutes of particle  $i$ , respectively, and  $T_{ij}^N$  is given by

$$T_{ij}^I = T_{ij}^N \equiv \frac{h_i T_i + h_j T_j}{h_i + h_j} \quad (2.65)$$

Equation (2.65) represents the temperature of the interface where no phase change occurs. For the interface between different materials, an alternative phase change occurring at its interface can be also considered. If we assume that either freezing or melting is dominant at the interface between different materials,  $T_{ij}^I$  is defined as

$$T_{ij}^I = \max[T_{ij}^N, T_{sol, \mathbf{M}(i)}] \quad \text{for freezing} \quad (2.66)$$

$$T_{ij}^I = \min[T_{ij}^N, T_{liq, \mathbf{M}(i)}] \quad \text{for melting} \quad (2.67)$$

Otherwise, phase change is suppressed at this interface by always assigning

$$T_{ij}^I = T_{ij}^N \quad (2.68)$$

In the present study, super cooling effect is not considered for simplification.

### B. Non-equilibrium mass transfer

The net heat flow rate at the interface is given by

$$\mathcal{Q}_{ij}^I = \mathcal{Q}_{i,j}^h + \mathcal{Q}_{j,i}^h \quad (2.69)$$

Once  $\mathcal{Q}_{ij}^I$  is determined, the melting/freezing rate can be calculated. If  $\mathcal{Q}_{ij}^I > 0$  and the particle  $i$  contains liquid phase, it will freeze partly into the solid phase. Its freezing rate per unit volume is calculated by

$$\Gamma_{i, \text{Freezing}} = \sum_{j \neq i} \frac{\mathcal{Q}_{ij}^I}{H_{l, \mathbf{M}(i)}} \quad (2.70)$$

where  $H_{l, \mathbf{M}(i)}$  is the specific latent heat of fusion given by

$$H_{l, \mathbf{M}(i)} = H_{liq, \mathbf{M}(i)} - H_{sol, \mathbf{M}(i)} \quad (2.71)$$

If  $\mathcal{Q}_{ij}^I < 0$  and the particle  $i$  contains solid phase, it will melt partly into the liquid phase.

Its melting rate per unit volume is calculated by

$$\Gamma_{i, \text{Melting}} = - \sum_{j \neq i} \frac{Q_{ij}^l}{H_{f, M(i)}} \quad (2.72)$$

Otherwise only sensible heat will be exchanged for the particle  $i$  by applying  $T_{ij}^N$  to the interface. As a result, to conserve the energy of particle  $i$ , the energy transfer rate of particle  $i$  should be expressed by

$$[Q^m]_i = \sum_{j \neq i} Q_{i,j}^h = \sum_{j \neq i} (\Gamma_{i, \text{Melting}} - \Gamma_{i, \text{Freezing}}) H_{f, M(i)} \quad (2.73)$$

### 2.7.3 Equilibrium model

Figure 2.7-3 shows the melting phase change diagram in equilibrium heat transfer. The phase change is determined when the solid particle's temperatures exceed the melting temperature or when the liquid particle's temperatures drop below solidification temperature. The temperatures of interface between liquid and solid phases, where phase change occurs, are the melting/solidification temperature of phase change material

$$T_i = T_{m/f} \quad 0 < \alpha_{i,l} < 1 \quad (2.74)$$

where  $T_i$  is the temperature of particle  $i$ ,  $T_{m/f}$  is the melting/solidification temperature, and  $\alpha_{i,l}$  denotes the liquid volume fraction of particle  $i$ , defined as

$$\alpha_{i,l} = \begin{cases} 1 & \text{for } H_{liq} < H_i \\ \frac{H_i - H_{sol}}{H_f} & \text{for } H_{sol} \leq H_i \leq H_{liq} \\ 0 & \text{for } H_i < H_{sol} \end{cases} \quad (2.75)$$

where  $H_{sol}$  and  $H_{liq}$  are the solidus and liquidus enthalpies, respectively,

### 2.7.4 Update of conservation equations

For the time step size  $\Delta t$ , the enthalpy of particle  $i$  can be updated by

$$H_i^{n+1} = H_i^n + \frac{\Delta t}{\rho_i} \left\{ \left[ \nabla \cdot (k \nabla T) \right]_i + [Q^h]_i + [Q^m]_i \right\} \quad (2.76)$$

where  $\rho_i$  is the density of particle  $i$ . The updated enthalpy of particle  $i$  is related to its temperature using the following relationships:

$$T_i = \begin{cases} \frac{1}{c_{l,M(i)}} (H_i - H_{liq,M(i)}) + T_{liq,M(i)} & \text{for } H_{liq,M(i)} < H_i \\ T_{sol,M(i)} + \frac{T_{liq,M(i)} - T_{sol,M(i)}}{H_{l,M(i)}} (H_i - H_{sol,M(i)}) & \text{for } H_{sol,M(i)} \leq H_i \leq H_{liq,M(i)} \\ \frac{1}{c_{s,M(i)}} (H_i - H_{ref,M(i)}) + T_{ref} & \text{for } H_i < H_{sol,M(i)} \end{cases} \quad (2.77)$$

where  $c_s$  and  $c_l$  are the specific heat capacities of solid and liquid phase, respectively, and  $H_{ref}$  is the specific enthalpy, which corresponds to that at the reference temperature  $T_{ref}$ . If the enthalpy of liquid particle becomes lower than  $H_{sol}$ , this particle is converted into the solid phase, while the solid particle becomes liquid one when its enthalpy exceeds  $H_{liq}$ .

Using the phase change rates, Eqs. (2.70) and (2.72), due to non-equilibrium transfers, the liquid and solid masses of particle  $i$  can be updated by

$$m_{l,i}^{n+1} = m_{l,i}^n + \Delta t (\Gamma_{i,Melting} - \Gamma_{i,Freezing}) V \quad (2.78)$$

$$m_{s,i}^{n+1} = m_{s,i}^n + \Delta t (\Gamma_{i,Freezing} - \Gamma_{i,Melting}) V \quad (2.79)$$

When the enthalpy of a liquid particle drops below the liquidus point or when the enthalpy of a solid particle exceeds the solidus point, it is assumed that the equilibrium melting/freezing processes occur. After the equilibrium transfers, the liquid and solid masses of particle  $i$  are redefined as

$$m_{l,i}^{n+1} = \frac{H_i^{n+1} - H_{sol,M(i)}}{H_{l,M(i)}} m_i \quad (2.80)$$



$$m_{s,i}^{n+1} = \frac{H_{liq,M(i)} - H_i^{n+1}}{H_{L,M(i)}} m_i \quad (2.81)$$

## 2.8 Buoyancy model

In present study, we assumed incompressible flows in the governing equations, and hence natural convection that is driven by the buoyancy force was considered by the Boussinesq approximation for the gravity term involved in  $\bar{f}$  of Eq. (2.10):

$$\bar{f}_g = \rho[1 - \beta(T - T_0)]\bar{g} \quad (2.82)$$

where  $\bar{g}$ ,  $\beta$  and  $T_0$  are the gravity, the volumetric thermal expansion coefficient and the reference temperature, respectively.

Shirakawa *et al.* (2013) suggested that particle methods would underestimate the buoyancy force caused by density deference between two phases, and introduced a buoyancy term in the pressure gradient term. In the present study, a similar idea is applied by adding a correction term to Eq. (2.10). For particle  $i$ , the modified buoyancy term is calculated as follows:

$$\bar{f}_{g,i} = \rho_i[1 - \beta_i(T_i - T_0)]\bar{g} - \sum_{i \neq j} c_B (\rho_j - \rho_i) \bar{g} w_{ij} \quad (2.83)$$

where  $c_B$  is the adjustable parameter.

In the CUP algorithm of the present code, the first and second terms in the right side of Eq. (2.83) are used to update the velocity separately. The first one is used in the explicit step to update the particle velocity without the pressure term as

$$\bar{u}_i^* = \bar{u}_i^n + \frac{\Delta t}{\rho_i} \left[ \nabla(\mu \nabla \cdot \bar{u}) + \bar{f}_s + \rho_i[1 - \beta_i(T_i - T_0)]\bar{g} \right] \quad (2.84)$$

where  $\vec{u}_i^*$  and  $\vec{u}_i^n$  are the intermediate velocity and the  $n$ -th time-step velocity of particle  $i$ , respectively. After the pressure calculation in the implicit step, the next time-step value of velocity is evaluated including the correction term to the buoyancy force:

$$\vec{u}_i^{n+1} = \vec{u}_i^* + \frac{\Delta t}{\rho_i} \left[ -\nabla p^{n+1} - \sum_{i \neq j} c_B (\rho_j - \rho_i) \vec{g} w_{ij} \right] \quad (2.85)$$

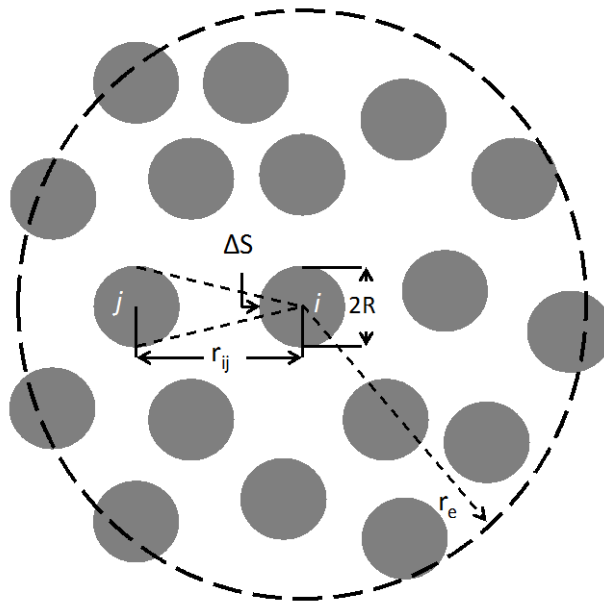


Figure 2.1-1 Neighbor particles of particle  $i$  in the cut-off radius

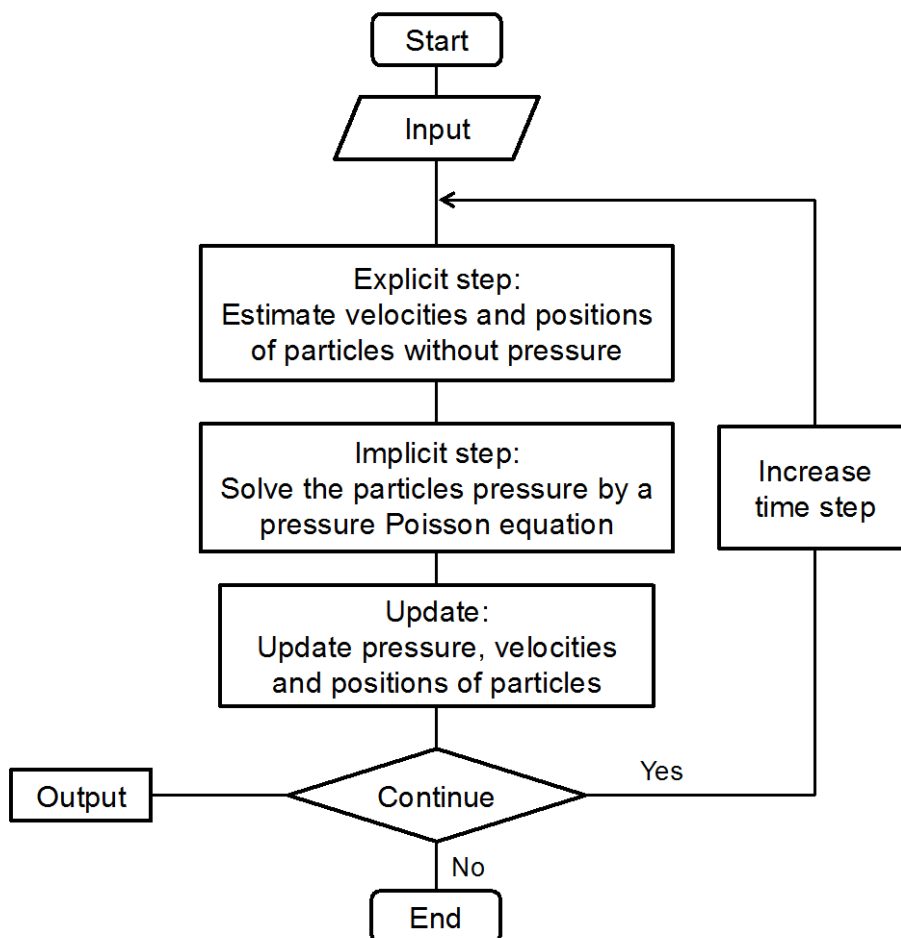


Figure 2.3-1 Explicit-implicit algorithms

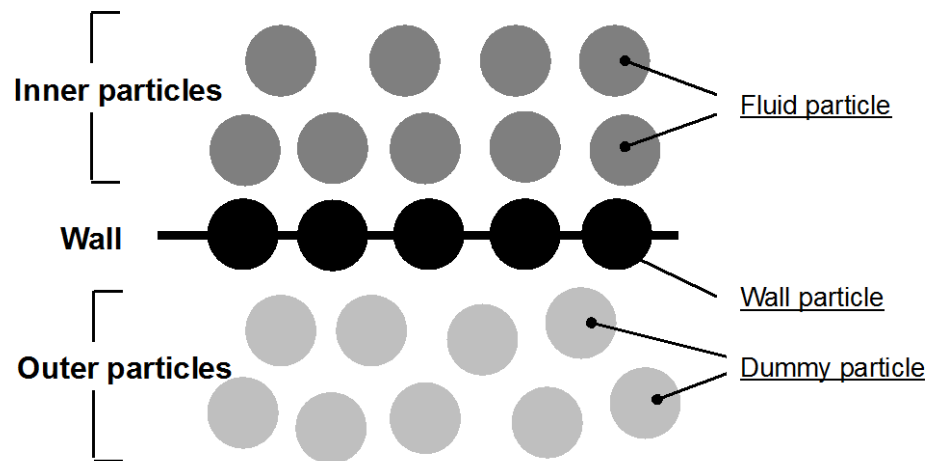


Figure 2.4-1 Wall boundary with dummy particles

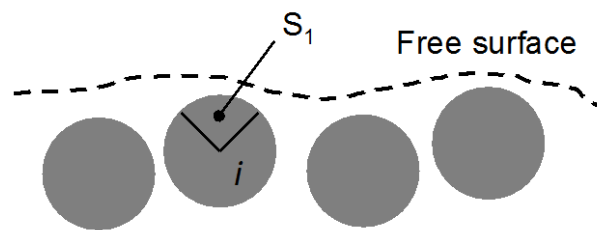


Figure 2.4-2 Free surface boundary

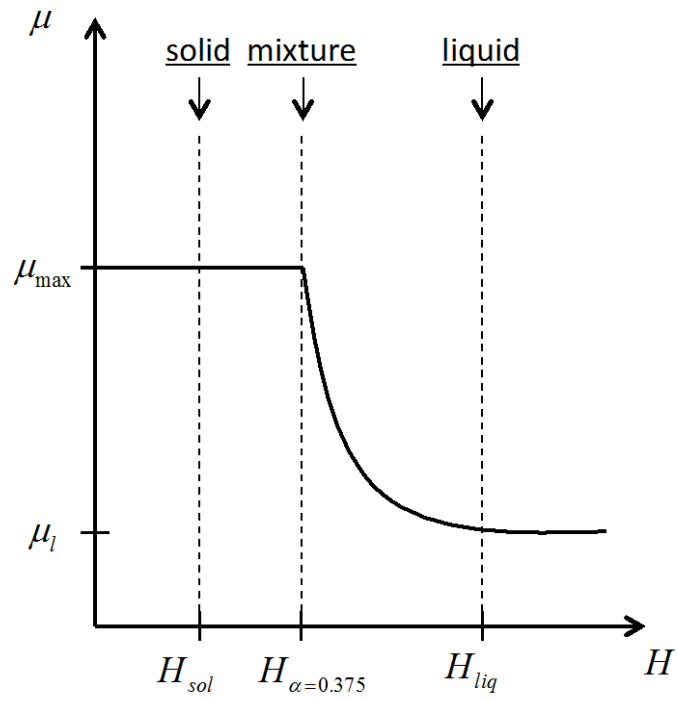


Figure 2.5-1 Rheology model

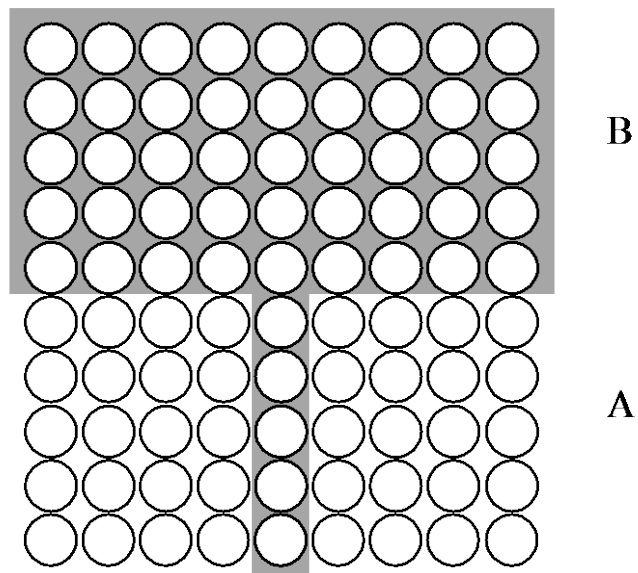


Figure 2.6-1 Schematic description of free surface energy between two blocks A and B

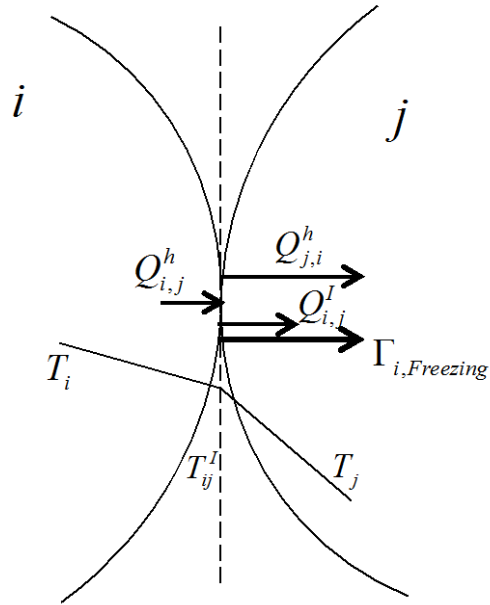


Figure 2.7-1 Mass transfer possibilities at interface between particles  $i$  and  $j$  with net heat flow to the interface from particle  $i$

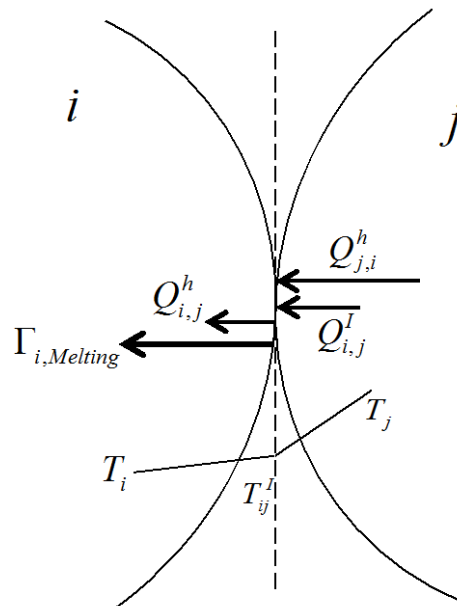


Figure 2.7-2 Mass transfer possibilities at interface between particles  $i$  and  $j$  with net heat flow to the interface from particle  $j$

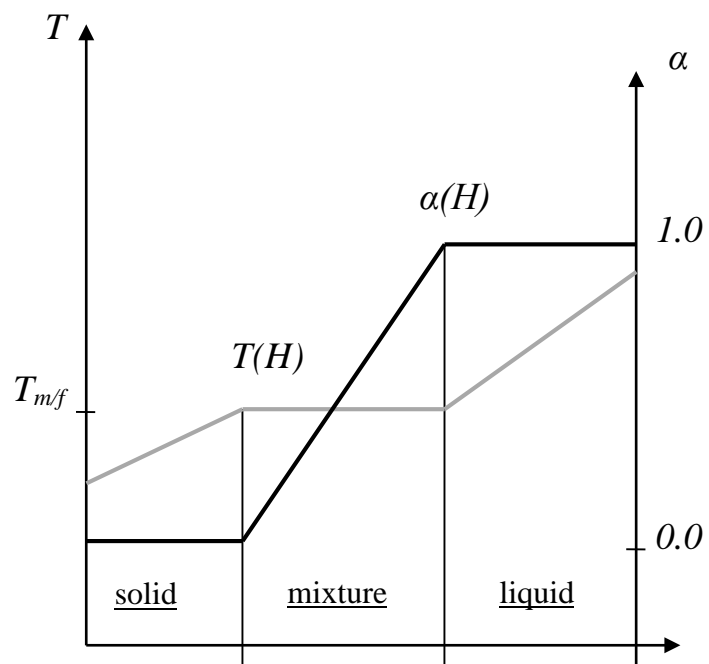


Figure 2.7-3 Phase change diagram

## Chapter 3

# Analysis of Early Fuel Discharge Behavior

### 3.1 Overview of EAGLE ID-1 test

#### 3.1.1 Test results

The in-pile large-scale test ID1, which was one of the integral demonstration experiments in the EAGLE project, was intended to generate a molten fuel/steel mixture, which simulated the relatively high-power subassembly under reactor accident conditions. Figure 3.1-1 shows the schematic of the main test section for the ID1 test. It consisted of the discharge cylindrical duct and the fuel assembly. The duct wall was made of stainless steel with inner diameter of 40 mm and thickness of 2 mm. The inner duct initially filled with liquid sodium was installed vertically at the central part through the annular structure of a fuel assembly jacket. A 75-pin fuel assembly surrounded the duct in three columns with 400-mm fissile height giving total fuel ( $\text{UO}_2$ ) amount of about 7.1 kg. The test section was inserted into the central experimental channel of the IGR core, and was heated up to around 570 - 670 K first.

The nuclear energy was then put into the fuel up to its temperature of about 3,270 K by the high neutron flux from the IGR core. In the ID1 test, the molten fuel at the temperature beyond its melting point exposed a duct wall, which simulated the inner duct wall of FAIDUS, to high heat flux of about  $10 \text{ MW/m}^2$ . The duct wall finally failed following the molten fuel penetration into the relocation path within a short period ( $\sim 1 \text{ s}$ ) after its melting even when the duct was initially filled with liquid sodium at around 700 K.



One of the key behaviors observed in the ID1 test is the early duct wall failure caused by high heat flux conditions. Therefore, mechanism of heat transfer from the molten fuel/steel mixture fuel to the duct wall must be well understood to demonstrate the effectiveness of FAIDUS as a design measure for CMR under reactor conditions. The heat transfer characteristics relevant to the duct wall failure have been investigated by integral thermal-hydraulic calculations using a fast reactor safety analysis code, SIMMER-III (Toyooka *et al.*, 2010; Toyooka *et al.*, 2013).

In this chapter, the heat transfer characteristics from the molten pool materials to outer surface of inner duct wall observed in the EAGLE ID-1 test were investigated through analyses using the particle-based simulations using the FVP method. Mechanisms of heat transfer with large thermal load to the duct wall as well as fuel crust formation were evaluated through comparison with the experimental data and the posttest analyses. Heat transfer characteristics involved in the ID1 test will be also discussed based on a phenomenological consideration.

### *3.1.2 Posttest analysis*

To clarify mechanism of the duct wall failure measured in the experiment, the posttest analyses were performed using the TAC2D and SIMMER-III codes.

#### *A. TAC2D test analysis*

TAC2D, which is a general-purpose heat conduction code, was used to estimate the wall temperature when the duct wall failure occurred in the test. In this calculation, by reproducing the temperature response locally measured at the inner surface of duct wall, the temperature of duct-wall outer surface was estimated to reach 1,625 K when the duct wall failure occurred in the experiment. It was also deduced that the average heat flux from the start of heat transfer until the duct wall failure was 10.7 MW/m<sup>2</sup>. Based on these estimations, integral thermal-hydraulic calculations were then performed to simulate the

whole process of ID1 test including the fuel-pin disruption, molten pool formation and duct wall failure behaviors using the SIMMER-III code.

### *B. SIMMER-III analysis*

In the SIMMER-III calculations, the ID1 test section of inner duct and fuel assembly was modeled in a 2D cylindrical coordinate system. The calculation results indicated that the outermost fuel pins started melting first at 4.2 s after the start of energy insertion into the test fuel. The following other fuel-pin disruption formed a fuel/steel mixture pool. Fuel crust formation on the colder duct wall surface was predicted to occur mostly in the lower pool region at the early stage of fuel melting. This built a thermal resistance layer suppressing the heat transfer from the mixture materials to the duct wall. On the other hand, in the upper pool region, the duct wall surface was exposed directly by the molten steel with rather high thermal conductivity. As a result, in the SIMMER-III calculation, the duct wall failure, which was defined to occur when the duct wall surface temperature reached 1,625 K according to the TAC2D estimation, was predicted at 0.7 s after the start of the pool-wall heat transfer. This early failure timing is comparable with the experimental result. In the calculation, the average heat flux from the start of heat transfer until the duct wall failure was about 10 MW/m<sup>2</sup> at the wall failure location. Such high heat flux, which is consistent with the TAC2D result, might be enhanced by a relatively larger fraction of molten steel, which accumulated in the upper pool region due to density difference between fuel and steel.

## **3.2 Modeling of EAGLE-1 ID1 test conditions**

### *3.2.1 Heat and mass transfer*

#### *A. Phase change processes*

In the present study, to analyze heat transfer characteristics from the molten pool materials to the outer surface of inner duct wall in the ID-1 test, the molten pool simulations, which initially start the calculation from a molten pool condition, were performed using the particle-based method. It was assumed that the molten pool can consist of molten fuel, molten steel and solid fuels including crust formed on the duct wall surface. The heat will be transferred from the molten pool to the sodium through the steel duct wall.

In the present simulations, the phase changes after the molten pool formation were modeled by the non-equilibrium model as well as the conventional equilibrium phase-change model (Guo *et al.*, 2010). Table 3.2-1 shows the non-equilibrium phase changes calculated in the present molten pool simulations. Seven binary interfaces were considered among liquid and solid fuel, liquid steel, steel wall and sodium. At the interfaces between different materials, liquid fuel/liquid steel and liquid fuel/steel wall contacts, fuel freezing was assumed dominant. Although, at the latter interface, both fuel freezing and steel wall melting are possible to occur, it was considered that the effect of crust formation on the steel wall on pool-wall heat transfer should be identified by the crust formation model with the non-equilibrium phase change model. Interface temperatures are defined based on the model formulas for interfacial heat transfer described in Chapter 2. Figure 3.2-1 presents the possible phase changes modeled as non-equilibrium transfers in the present molten pool simulations.

#### *B. Mathematical models for crust formation*

The fuel crust formation on the steel wall could deteriorate the heat transfer from the molten pool to the duct wall due to low thermal conductivity of the crust fuel. To model this effect reasonably, at the liquid fuel/steel wall and liquid fuel/fuel crust interfaces,

considering the thickness of solid crust formed on the duct wall, the heat transfer coefficient of liquid fuel side is calculated instead of Eq. (2.58) by:

$$h_i = \frac{1}{\frac{\min(\delta_{c,i}, \Delta l/2)}{k_{s,fuel}} + \frac{\Delta l/2 - \min(\delta_{c,i}, \Delta l/2)}{k_{l,fuel}}} \quad (3.1)$$

where  $k_{s,fuel}$  and  $k_{l,fuel}$  are the thermal conductivity of solid and liquid fuel, respectively.

The crust thickness of particle  $i$  is defined by

$$\delta_{c,i} = \frac{m_{s,i}}{m_i} \Delta l \quad (3.2)$$

where  $m_i$  and  $m_{s,i}$  are the total and solid masses of particle  $i$ , respectively. Equation (3.2) is formulated by considering the thickness of solid crust formed on the duct wall.

### 3.2.2 Viscosity and buoyancy force

The rheological behavior in melt under melting and freezing has obvious influence on solid and fluid dynamics. In the present study, based on Eq. (2.37), it was considered as change in viscosity of melt as a function of melt enthalpy based on our previous works (Guo *et al.*, 2010; Mahmudah *et al.*, 2011). In addition, the effective viscosity of solid-liquid mixture in the molten pool was also considered by the Frankel-Acrivos model, Eq. (2.36) separately. This will be discussed in Section 3.3.

In the present simulations, natural convection flows in the sodium channel and the molten pool were considered by Eq. (2.80). The value of adjustable parameter  $c_B$  was determined based on a specific test calculation for a single SS droplet with the diameter of 25 mm rising in a stagnant liquid UO<sub>2</sub> pool. Based on the calculation results shown in Fig. 3.2-2, its value was adjusted and determined as 0.01. The test calculation demonstrated that the modified buoyancy term with  $c_B = 0.01$  can reproduce the terminal

velocity of SS droplet, which can be evaluated by an empirical correlation (Grace *et al.*, 1976), accurately.

### 3.2.3 Geometrical conditions

According to discussion on experimental results, which show that the duct wall failure occurred by less than 1 s after the fuel and steel materials started melting, the molten pool calculations were performed for 1 s from the molten pool mixture under several conditions. Since in the present simulations the initial conditions were different from those of the ID-1 test, we performed 2D calculations based on equivalent geometrical conditions for the molten pool, the duct wall and the sodium channel after the start of molten pool-duct wall heat transfer. Figure 3.2-3 shows the schematic of the geometrical conditions used in the present molten pool simulation.

Main physical phenomena to be simulated were heat transfer from the molten pool to the sodium channel through the duct wall, heat transfer among pool materials, and molten fuel freezing on the duct wall as solid crust. In the present simulations, the initial particle distance  $\Delta l$  was set at 1.0 mm, and the time step size was chosen as  $1.0 \times 10^{-4}$  s. We assumed adiabatic geometrical boundaries, neglecting the effect of heat transfer from the system to surroundings. This might be acceptable for a short period time of the present simulations. In the following discussion, time zero corresponds to the start of the molten pool-duct wall heat transfer.

Table 3.2-2 shows the calculation conditions for the present molten pool simulation of the ID-1 test. The experimental geometry was represented by an x-z Cartesian system with a mixture pool of 192 mm in height, which is equivalent to the height of disrupted 75-pins in the annual volume with 26-mm width. The width of the pool region in the calculations was determined based on the ratio of contact area between the mixture pool and the duct wall to the mixture volume. Although the resultant pool width of 41 mm is

different from the experimental one, an equivalent thermal load to the duct wall, which is induced by the mixture pool, can be represented approximately using the same volume of the pool mixture per unit area of the duct wall as that in the experiment. The hydraulic diameter of the sodium channel (10 mm) was taken from the experimental condition.

#### *3.2.4 Initial pool conditions*

In the posttest analysis (Toyooka *et al.*, 2010; Toyooka *et al.*, 2013), it was discussed that the presence of steel in the mixture pool played key roles in quite high heat flux to the duct wall, which might lead to the early wall failure. Therefore, it is of importance to clarify which pool conditions can contribute to the thermal load to the duct wall with high heat flux. In the present study, several initial conditions of the duct wall contact to the mixture pool, fuel crust formation on the duct wall, and steel droplet size were considered as the key parameters, which could have a large impact on the thermal load to the duct wall.

##### *A. Mixture pool composition*

The history of nuclear energy generation in the fuel of the ID1 test suggests that the total energy input into the fuel by the start of molten pool-wall heat transfer was just about the energy necessary to heat the fuel up to the enthalpy at its liquidus temperature (Konishi *et al.*, 2006). This energy should be expended not only to melt the fuel pellets and steel claddings of the pins, but also to increase their temperatures as well as those of the duct wall and the sodium. Therefore, in the present simulations, it was roughly assumed that the mixture pool consisted of fuels in liquid and solid phases and steel in liquid phase at the start of the pool-wall heat transfer. Here, we considered three cases of initial solid-fuel temperature, 1,750 K, 2,250 K and 2,500 K to specify the mass fraction of solid phase in the fuel. In addition, we assumed that the temperatures of molten fuel and steel were 3,150 K and 1,750 K, respectively, which are just beyond their melting

points, when the mixture pool was formed. By simple energy balance calculations using appropriate thermo physical properties of fuel and steel (IAEA, 2008), we obtained the initial conditions of solid fuel in the mixture pool as shown in Table 3.2-3. It can be seen that the solid fuel occupies almost half of the fuel mass in the mixture pool even if we assume that the temperature of solid fuel is the same as that of molten steel. In addition, transient molten-pool calculations under these initial conditions showed that there is no remarkable difference in average temperature increase of the mixture pool among the three cases. Therefore, hereafter, we took the mass fraction 47% of solid phase at 1,750 K in fuel as a reference condition.

### *B. Nuclear heating*

In the ID1 test, adequate nuclear power to the fuel in the test section was given to form the fuel/steel mixture pool by the power pulse transient of IGR. In the present simulations, we used the total nuclear heat to the fuel equivalent to that of the ID-1 test after the mixture pool formation. It was assumed that the average nuclear heating rate per unit fuel volume is given as the following linear function of time approximately:

$$Q^n[\text{W/m}^3] = 1.15 \times 10^9 (t + 4.2) \quad (3.3)$$

where  $t$  [s] is the time after the start of the molten pool-duct wall heat transfer. In the simulations, Eq. (3.3) was included in the term  $Q$  of the energy equation, Eq. (2.12). The axial and lateral nuclear power profiles were also considered based on the experiment.

## **3.3 Simulation results of EAGLE ID-1 test**

### *3.3.1 Effect of fuel crust*

In the posttest analyses (Toyooka *et al.*, 2010; Toyooka *et al.*, 2013), time variations of duct-wall surface temperature on the pool side were predicted by the SIMMER-III

code. The results indicated that the crust formation on the duct wall surface deteriorated the pool-wall heat transfer largely. In the present study, to find the typical initial pool conditions from the viewpoint of pool-wall heat transfer, the local temperature of duct wall surface predicted by the SIMMER-III code was compared with those calculated by the present particle-based simulation. Although the initial pool compositions were determined based on the above discussion, we simply considered a homogeneous mixture of solid fuel, liquid fuel and liquid steel with initial random arrangement. Two parametric cases were calculated to preliminary know the characteristics of pool-wall heat transfer. One case assumed the surface of the duct wall initially contacting the homogeneous fuel/steel mixture directly, and the other was the duct wall surface covered by the fuel crust with thickness of 1 mm. hereafter, these calculations are called the cases of pool mixture contact and fuel crust contact, respectively. In the former case, about 25% of the duct-wall surface contacted the molten steel according to the volume fraction of steel in the pool.

Figure 3.3-1 shows the two calculation results of duct-wall surface temperature in comparison with the result predicted by the SIMMER-III code (Toyooka *et al.*, 2013), which was obtained as the temperature of duct wall surface covered by re-frozen fuel crust. Here, in the present calculations, the duct-wall surface temperatures were evaluated by extrapolating the inside temperatures of the duct wall to the depth of 0.2 mm from the duct surface facing to the pool at the axial position of 100 mm from the pool bottom. This definition of duct-wall surface temperature is consistent with that in the SIMMER-III calculation. It can be seen that the time variation of duct-wall surface temperature in the case of fuel crust contact reasonably agrees with the SIMMER-III prediction after the start of molten pool-wall heat transfer ( $t = 0$ ), although the crust thickness of 1 mm was specified arbitrary. On the other hand, in the case of pool mixture contact, the temperature



change is overestimated due to relatively higher thermal conductivity of molten steel. The present result suggests that some fuel crust might be formed on the duct-wall surface when the duct-wall heat transfer was initiated.

Figure 3.3-2 indicates the axial distributions of heat flux through the duct wall at 0.1 s, 0.3 s, 0.5 s and 0.7 s in the cases of pool mixture contact and fuel crust contact, respectively. Here, they were graphed using the average heat fluxes for every 2.0 cm axial length along the duct wall. The heat flux obtained in the case of fuel crust contact is fairly smaller than that at the duct wall failure, which was predicted to be more than 10 MW/m<sup>2</sup> by the calculations using TAC2D and SIMMER-III (Toyooka *et al.*, 2013). On the other hand, the case of pool mixture contact shows larger heat flux due to good pool-wall heat transfer. As suggested by the posttest analysis (Toyooka *et al.*, 2013), during the pool formation process after the pin disruption, the phase separation between fuel and steel materials can occur in their mixture pool due to their density difference. In addition to the crust formation on the duct wall surface, this effect might also play a key role in heat transfer from the pool to the duct wall due to the difference in thermal conductivity between fuel and steel. Therefore, in the present study, we assumed that the steel material accumulates more in the upper pool region due to its smaller density, while it was considered that the fuel crust was formed on the duct-wall surface in the lower pool region during the early stage of pool-wall heat transfer. Based on this idea, in the following simulations, the mixture pool was divided into two regions, the upper steel-rich region and the lower fuel rich region, in which the fuel crust was formed initially on the duct wall surface.

### 3.3.2 Effect of molten steel

In the present simulations, the heights of the lower and upper pool regions were arbitrarily defined as 130 mm and 62 mm, respectively. The duct-wall surface in the

lower pool region was covered by the fuel crust of 1 mm in thickness. To consider the effect of steel fraction in the mixture pool on the pool-duct wall heat transfer, at first we performed four parametric calculations using different steel fractions. Table 3.3-1 shows the volume fractions of molten steel in the upper and lower pool regions for the four cases, Cases A, B, C and D. We assumed that in the upper pool region the molten steel was mixed with the fuel in one-third of the volume in Case A, and two-third in Case B. For the lower pool region, the volume fraction of steel was also varies among the cases since the total volumes of the fuel and steel in the pool were kept at constant. In Cases A and B, the area fractions of liquid steel-wall contact were nearly identical to the volume fractions of molten steel in the upper pool regions, while only the fuel crust contacted the duct wall in the lower pool region.

Figure 3.3-3 indicates the initial material configurations in Cases A and B. On the other hand, in Cases C and D, the duct wall surface in the upper pool region initially contacted the molten steel at the area fraction of 70% and 30%, respectively. These intentional fractions in Cases C and D were similar to those in Cases B and A, respectively. It is noted that initial material fractions in the upper- and lower-pool regions in Cases C and D were the same as those in Cases A and B, respectively. These two cases were calculated to investigate the effect of the local steel-wall contact on the pool-wall heat transfer. A homogeneous mixture of solid fuel, liquid fuel and liquid steel was specified with initial random configuration except for the pool adjacent to the wall in Cases C and D. The other initial conditions of mixture materials were the same as those considered in the previous discussion.

In Fig. 3.3-4, the calculation results on the average temperatures of molten fuel and steel in the mixture pool are compared with those of SIMMER-III (Toyooka *et al.*, 2013). The molten fuel temperature increases are slow because the nuclear heat in the fuel is

consumed to heat up and melt the solid fuel, which occupies about half of fuel initially. In the SIMMER-III calculation, the molten steel temperature increases rapidly at around 0.65 s due to development of whole mixing of fuel and steel in the pool after all of the pins disrupted finally. This cannot be represented by the present molten pool simulation on the assumption of the initial homogeneous fuel/steel mixture. Nevertheless, the present simulations show reasonable results on the average temperature increases of the mixture pool in comparison with the SIMMER-III results.

Figure 3.3-5 shows the axial distribution of heat flux through the duct wall at 0.1 s, 0.3 s, 0.5 s and 0.7 s after the start of pool-wall heat transfer in Cases A and B. In both cases, the duct wall is exposed by higher heat flux in the upper pool region, and the highest heat flux in Cases A is smaller than that in Case B, where the initial steel volume fraction is twice larger than that in Case A. In addition, in both cases, the highest heat flux appears in the early stage of heat transfer due to initial large temperature difference between the pool and the wall. On the other hand, the pool-wall heat transfer in the lower pool region with fuel crust on the duct wall is fairly smaller than that in the upper pool region relatively.

The time variations of averaged heat fluxes over the upper and lower pool regions in Cases A and B are indicated in Fig. 3.3-6. It can be seen that the duct wall in the upper pool region is exposed to quite high heat flux more than  $10 \text{ MW/m}^2$  during the early stage of pool-wall heat transfer. As the duct wall temperature increases, the heat flux decreases gradually. The time-averaged heat flux in the upper and lower pool regions are  $9.5 \text{ MW/m}^2$  and  $10.4 \text{ MW/m}^2$  in Cases A and B, respectively, during the first period of 0.3 s. These values are good agreement with the result predicted by the SIMMER-III code.

The axial heat-flux distributions in Cases C and D are presented in Fig. 3.3-7. In these cases, the heat fluxes in upper pool region also exceed  $10 \text{ MW/m}^2$  during the early

stage of pool-wall heat transfer. However, in Case C, regardless of smaller molten-steel concentration in the upper pool, the heat flux there is larger than that in Case D. Figure 3.3-8 shows the comparison of the time variations of averaged heat fluxes over the upper pool region among Cases A, B, C and D. The result of Case C indicates very high heat flux of about  $13 \text{ MW/m}^2$  around at 0.14 s, although its upper pool has half the amount of molten-steel compared with that in Case B. On the other hand, Cases A and D show similar lower heat flux change. Considering the difference in initial duct surface area contacting the molten steel, these results suggest that the amount of molten steel in the pool has less influence on the duct-wall heat flux, while the thermal load induced by the molten pool strongly depends on local molten-steel/duct-wall contact. As a matter of course, the larger the steel volume fraction, the larger the steel-wall contact area.

### 3.3.3 Crust formation behavior

In all of the parametric cases to investigate the effect of molten steel on pool-wall heat transfer, as explained above, the duct wall in lower pool region was intentionally covered by the fuel crust with initial thickness of 1 mm. This condition was based on the discussion with SIMMER-III results (Toyooka *et al.*, 2013), where more fuel accumulated in the lower pool region after the molten pool formation. Since the melting point of fuel is much higher than that of steel, the molten fuel can solidify first on the cold duct wall surface by time and spatial variation. In the present study, the crust formation model, as explained in Chapter 3, modeled this fuel crust formation behavior.

Figure 3.3-9 shows the axial distribution of local crust thickness at 0.3 s in Cases A and B. After the start of pool-wall heat transfer, the fuel crust with initial thickness of 1 mm grows in the lower pool regions, while the new crust is formed even in the upper pool region locally and discretely. In Case B, the crust formation is rather sparse in the upper pool region due to a larger fraction of molten steel, and hence the molten steel can contact

larger area of the duct wall surface directly in comparison with Case A. This direct molten-steel contact should enhance the pool-wall heat transfer in the upper pool region.

In Fig. 3.3-10, the axial distributions of spatial-average crust thickness are presented at 0.1 s, 0.3 s, 0.5 s and 0.7 s in Cases A and B. Here, they were evaluated as the average thickness for every 2.0 cm axial length along the duct wall. In the lower pool region the fuel crust grows rapidly, while remarkable crust growth cannot be seen in the upper region. In addition, the comparison between Cases A and B indicates that the crust growth rate depends on the fraction of molten fuel in the pool. These crust formation on the duct wall surface could deteriorate the molten pool-duct wall heat transfer, and the present results on the crust behavior are consistent with the resultant heat flux in Cases A and B, which are shown in Fig. 3.3-5.

The time variations of averaged crust thickness over the upper and lower pool regions in Cases A and B are indicated in Fig. 3.3-11. It can be seen that the fuel crust gradually becomes thicker in the lower pool region, while in the upper pool region the crust growth almost stagnates. These crust growth behaviors might arise from the difference of fuel fraction adjacent to the crust formed on the duct wall. As can be seen in Figs. 3.3-9, 10 and 11, in the lower pool region, the crust growth in Case A is much larger than that in Case B, although the smaller fraction of molten fuel in the lower pool region in Case A. This is because larger nuclear heat in the lower pool region makes the pool temperature higher.

#### *3.3.4 Duct wall failure*

In the ID1 test, the early duct wall failure was observed at about 0.7 s after the start of the melt contact to the duct wall under the high heat flux of about 10 MW/m<sup>2</sup>. In the posttest analysis using the TAC2D code (Toyooka *et al.*, 2013), it was deduced that the duct wall failure might occur when the surface temperature of duct wall reached 1,625 K,

and the SIMMER-III calculation with this criterion showed a consistent result with the experimental one on the timing of wall failure.

Figure 3.3-12 indicates the results of Case C on the duct wall temperatures at the pool-side surface and at the center of wall thickness in the upper and lower pool regions. The temperatures in the lower and upper pool regions were evaluated as the temperature averaged over the axial length of 2.0 cm along the duct wall at 5.0 cm and 15.0 cm above the pool bottom, respectively. In the lower pool region, the temperature increases are slower than those in the upper pool due to thermal resistance of fuel crust on the duct wall. On the other hand, the duct-wall surface temperature in the upper pool region increases rapidly due to large heat transfer during the early transient, and reaches to 1,625 K at 0.27 s after the start of the pool-wall heat transfer. This rapid temperature increase was caused by the direct contact of molten steel to the duct wall as well as discrete formation of fuel crust on the duct wall in the upper pool region. In the present molten pool simulations, we assumed the instantaneous mixture pool formation as an initial condition, and hence the wall failure timing cannot be compared with the experimental result directly. However, based on the experimental fact that the duct wall failure occurred at about 0.3 s after all of the pins disrupted finally and the fuel/steel mixture was formed, the present result indicates the possibility of early duct wall failure due to effects of molten steel in the mixture pool.

### *3.3.5 Effect of steel droplet size*

In the above parametric cases, solid fuel, liquid fuel and liquid steel were homogeneously mixed in the pool with initial random configuration of numerical particles, of which size was equivalent to 1 mm square in the present 2D simulations. Therefore, the minimum size of dispersed phases in the pool can be also 1 mm square. Since this size could change heat transfer behavior, an additional parametric simulation

was performed to investigate the effect of molten steel dispersion in the mixture pool using larger smaller steel droplets. In this case, steel droplets of 5 mm in width, each of which consists of 21 numerical particles, were mixed with fuel in liquid and solid phases. Therefore, the steel droplets dispersed coarsely in the mixture pool compared with other cases. Although the initial area fraction of molten steel-wall contact was 30% in the upper pool region, the other initial conditions were the same as those in Case A. Figure 3.3-13 shows the initial material configurations in the case of larger steel droplets. It is noted that the initial contact area between molten steel and duct wall was exactly similar to that in Case A.

The axial distributions of heat flux through the duct wall at 0.1 s, 0.3 s, 0.5 s and 0.7 s in the case of larger steel droplets is shown in Fig. 3.3-14. It can be seen that the heat flux distributions are similar to those in Case A, which is shown in Fig. 3.3-5 (a). Figure 3.3-15 compares the time variations of averaged heat fluxes over the upper and lower pool regions between Case A and the case of larger steel droplets. There is no essential difference between them. These results demonstrate that the coarse mixing of steel droplets in the pool does not change the heat transfer characteristics, although the heat transfer area between steel and fuel is smaller than that in Case A.

### 3.3.6 *Effect of fuel-steel mixing*

In the above simulations, the rheological behavior in the molten pool mixture was calculated using Eq. (2.37), which determines the viscosity of each numerical particle based on its specific enthalpy. The simulation results showed almost no mixture movement in the pool because the fraction of solid fuel with low enthalpy is large in the mixture pool. At present, the validity of this pool behavior is not verified, and hence for comparison we introduced the effective viscosity of solid-liquid mixture based on the Frankel-Acrivos model, Eq. (2.36), into the simulations in place of the rheology model.

Figure 3.3-16 illustrates the material distribution in the computational domain at 0.1 s, 0.3 s, 0.5 s and 0.7 s in Case B with the effective viscosity model. It can be seen that the molten steel driven by buoyancy is going to accumulate near the surface of the upper pool. This is because the present effective viscosity depends on solid fraction, which is smaller in the upper pool region.

The molten steel movement would change the heat transfer behavior as well as fuel and steel mixing behavior in the pool. Figure 3.3-17 shows the comparison of the upper pool heat fluxes through the duct wall between the simulations with the rheology model and the effective viscosity model in Cases A and B. It can be seen that in general the heat fluxes are a little bit higher in the cases using the effective viscosity model. In Fig. 3.3-18, the calculation results on the average temperatures of molten fuel and steel in the mixture pool are compared between the simulations with the rheology model and the effective viscosity model in Case A. There is no large difference in the average temperatures of both molten fuel and steel between two cases. These results suggest that the fuel and steel mixing behavior in the pool does not much change the duct surface area contacting the molten steel, and has less significant effect on heat transfer from the pool to the duct wall under the present calculation conditions.

### 3.4 Discussion

The potential thermal load to the duct wall should be caused by the heat transfer due to the temperature difference between the wall and the mixture pool, and the nuclear heating in the fuel. Therefore, the possible heat flux to the duct wall can be expressed by

$$q_{wall} = h_{eff} \Delta T + q_{nuci} \quad (3.4)$$

where  $h_{eff}$  is the effective heat transfer coefficient, which includes both conductive and convective effects,  $\Delta T$  is the temperature difference between the duct wall surface and



the bulk of mixture pool, and  $q_{nuc}$  is the heat flux caused by the nuclear heating in the fuel. It is noted that the direct heat transfer to the wall caused by the nuclear heating is possible without undergoing heat transfer processes among the pool materials.

As we discussed in Section 3.2.3, about half the fuel in the mixture pool is estimated in solid phase at the start of the pool-wall heat transfer. It is expected that the convection flows in the mixture pool might not develop largely in a short period of time. This might be bone out by the simulation result on solid fraction in fuel. Figure 3.4-1 shows the time variation of solid-phase volume fraction in fuel in Case A. As discussed in Section 3.2.3, its initial faction is set to 47%. After the start of molten pool-wall heat transfer, part of molten fuel freezes into solid phase due to cooling by sodium through the duct wall and heat transfer to the colder pool materials. It can be seen from Fig. 3.4-1 that the solid fraction reaches to 77% at 0.15 s, and gradually decreases due to the nuclear heating in the fuel. This large solid fraction might hider the fluid movement due to small mobility of fuel material in the mixture pool during the early stage of pool-wall heat transfer. Therefore, we assume that development of convection flows is not enough to enhance the bulk heat transfer before the duct wall failure and contribution of convective heat transfer to the total heat flux becomes relatively smaller than others. On the other hand, the conductive heat transfer from the bulk of mixture pool to the duct wall can be enhanced by the molten steel mixed with fuel in the pool. If the mixture pool consists of the molten fuel and steel, we can simply estimate  $h_{eff}$  as

$$h_{eff} = \frac{k_m}{L/2} \quad (3.5)$$

where  $k_m$  is the effective thermal conductivity of the pool mixture and  $L$  is the pool characteristic length for heat transfer. The value of  $k_m$  was evaluated approximately

using the following conventional Maxwell-Garnett's model (Lee J. *et al.*, 2010), although it is applicable to dilute solid-liquid mixtures of relatively large particles:

$$k_m = \frac{k_s + 2k_f + 2(k_s - k_f)\alpha}{k_s + 2k_f - (k_s - k_f)\alpha} k_f \quad (3.6)$$

where  $k_f$  and  $k_s$  are the thermal conductivity of fuel and steel, respectively, and  $\alpha$  is the volume fraction of steel in the mixture. By taking  $\Delta T = 2,430$  K as the initial temperature difference between the molten fuel and the duct wall,  $L = 0.04$  m as the pool width,  $k_f = 5.0$  W/(m·K) and  $k_s = 20.6$  W/(m·K), the potential heat flux caused by the temperature difference between the wall and the mixture pool is estimated as 0.97 MW/m<sup>2</sup> for  $\alpha = 0.33$  and 1.5 MW/m<sup>2</sup> for  $\alpha = 0.66$ . These values are fairly smaller than the calculated heat flux, which can be more than 10 MW/m<sup>2</sup> in the upper pool region. The present rough estimation suggests that enhancement of conductive heat transfer due to molten steel with high thermal conductivity has a relatively smaller contribution to such high heat flux.

According to the above discussion, it is deduced that the thermal load to the duct wall is mainly induced by the nuclear heating in the fuel, and that the convective and conductive heat transfers from the bulk to the duct wall contribute less to it. This is demonstrated by the simulation case with coarse mixing of steel droplets in the mixture pool, where the steel droplet size had less effect of pool-duct heat transfer as presented in Section 3.3. On the other hand, the nuclear heat in the fuel can be effectively transferred through the local contact of liquid steel to the duct wall. Therefore, larger contact area between the molten steel and the duct wall can enhance the local heat transfer near the duct wall. This might be the main mechanism of effective heat transfer with high heat flux to the duct wall, which is caused by the molten steel in the mixture pool. In the upper pool region, although the fuel crust can be formed on the cold duct wall surface, it

develops discretely due to relatively larger fraction of molten steel there, and hence the molten steel contact to the duct wall is not prevented largely. This mechanism is also attributed to one of the molten steel effects, which enhance the pool-duct heat transfer.

Table 3.2-1 Non-equilibrium phase changes modeled in molten pool simulation.

Interface	Dominant phase change	Interface temperature
• Liquid fuel/liquid steel	Fuel freezing	Eq. (2.63)
• Liquid fuel/solid fuel	Fuel melting and freezing	Eq. (2.61)
• Liquid fuel/steel wall	Fuel freezing (crust formation)	Eq. (2.63)
• Liquid steel/solid fuel	No phase change	Eq. (2.65)
• Liquid steel/steel wall	Steel melting and freezing	Eq. (2.61)
• Solid fuel/steel wall	No phase change	Eq. (2.65)
• Steel wall/sodium	No phase change	Eq. (2.65)

Table 3.2-2 Conditions of molten pool simulation.

Mixture pool		
Height × Width	[mm]	192 × 41
Total volume	[m <sup>3</sup> ]	7.87×10 <sup>-3</sup>
(Fuel)	[m <sup>3</sup> ]	5.91×10 <sup>-3</sup>
(Steel)	[m <sup>3</sup> ]	1.96×10 <sup>-3</sup>
Total mass	[kg]	70.8
(Fuel)	[kg]	56.6
(Steel)	[kg]	14.2
Duct wall		
Thickness	[mm]	2.0
Initial temperature	[K]	720
Sodium channel		
Width	[mm]	10
Initial temperature	[K]	720

Table 3.2-3 Initial conditions of solid fuel in mixture pool.

Temperature of solid fuel	Mass fraction of solid phase in fuel
1,750 K	0.47
2,250 K	0.59
2,500 K	0.69

Table 3.3-1 Molten steel fractions in upper and lower pool regions.

	Upper pool region		Lower pool region
	Volume fraction of molten steel [%]	Area fraction of molten steel-wall contact [%]	Volume fraction of molten steel [%]
Case A	33	33	21
Case B	66	68	4
Case C	33	70	21
Case D	66	30	4

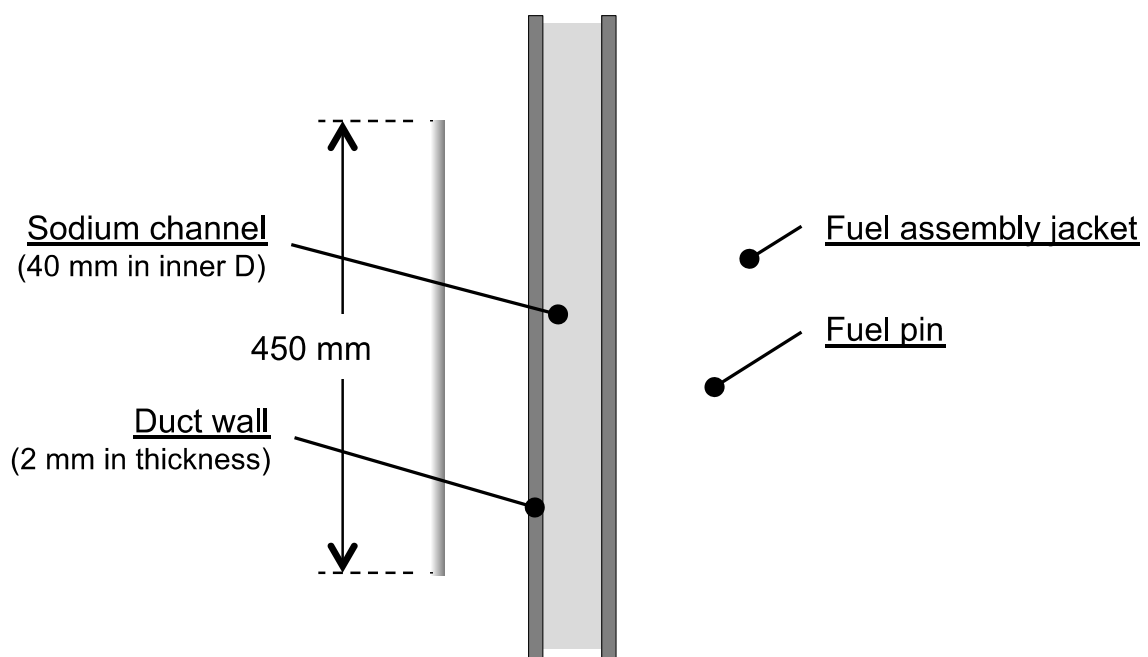


Figure 3.1-1 Schematic of main test section for ID1 test.

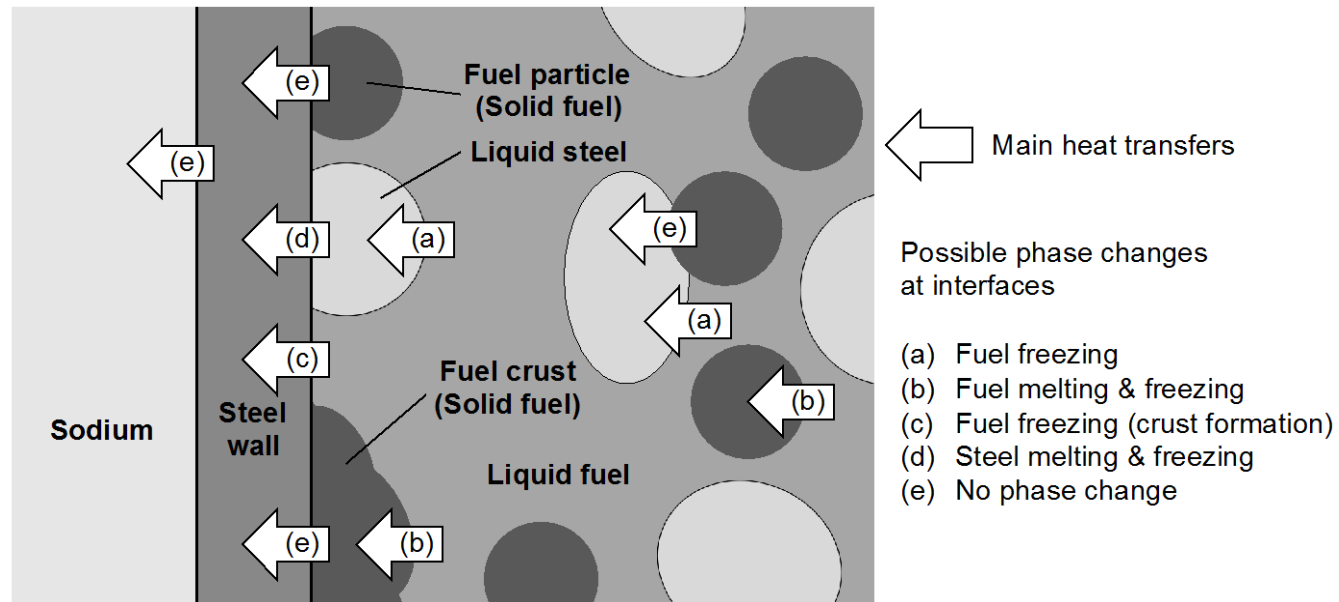


Figure 3.2-1 Possible phase changes modeled as non-equilibrium transfers.



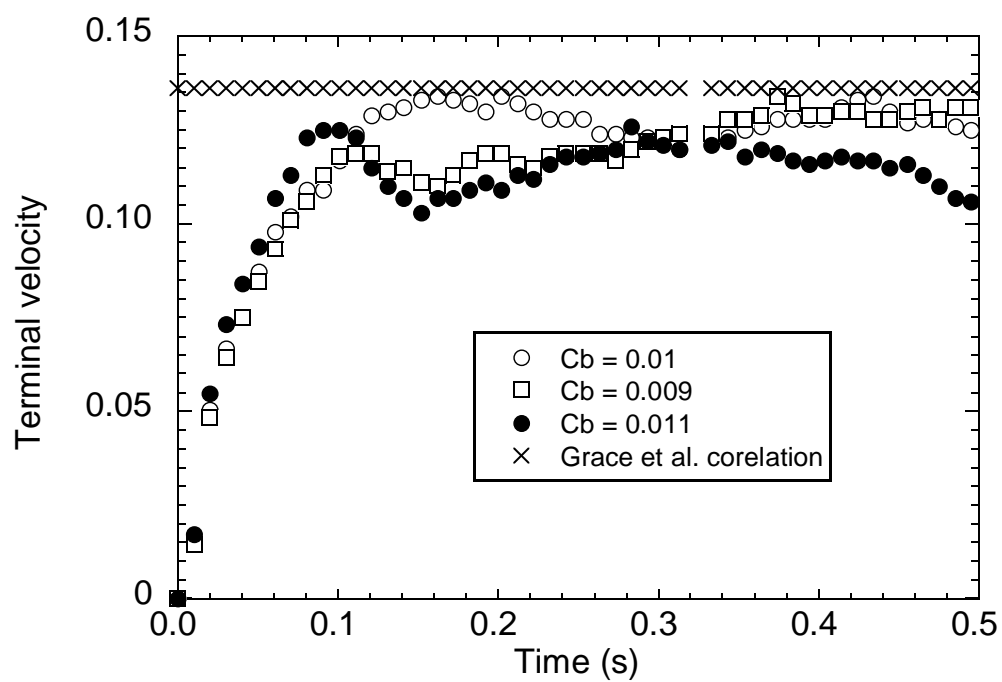


Figure 3.2-2 Test calculation result of a single SS droplet rising

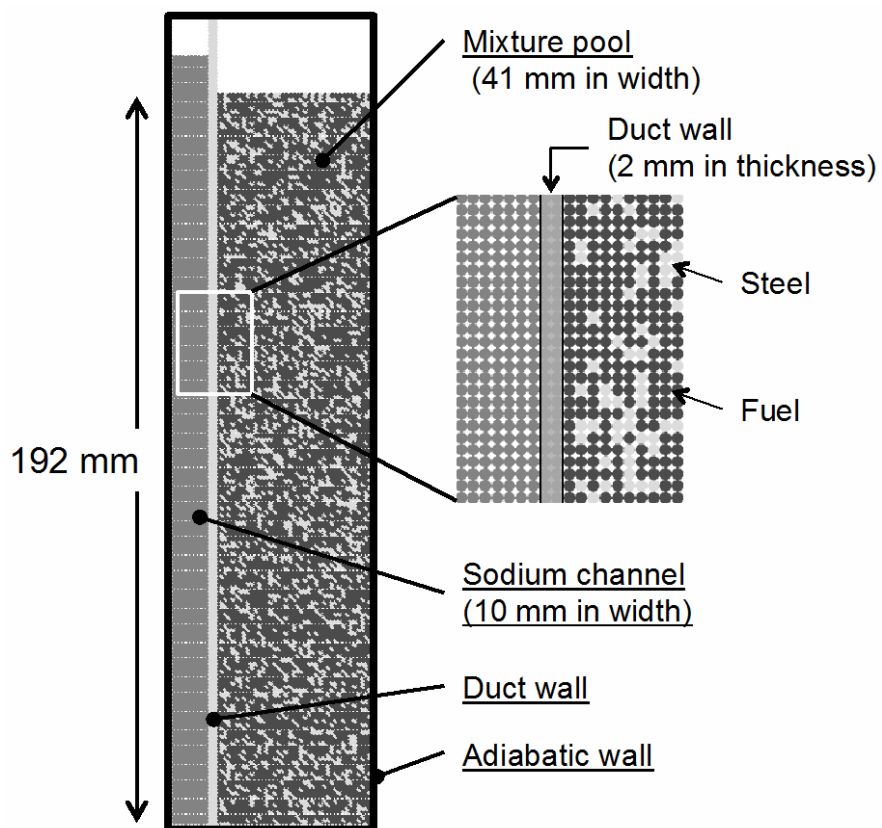


Figure 3.2-3 Geometrical conditions for molten pool simulation.

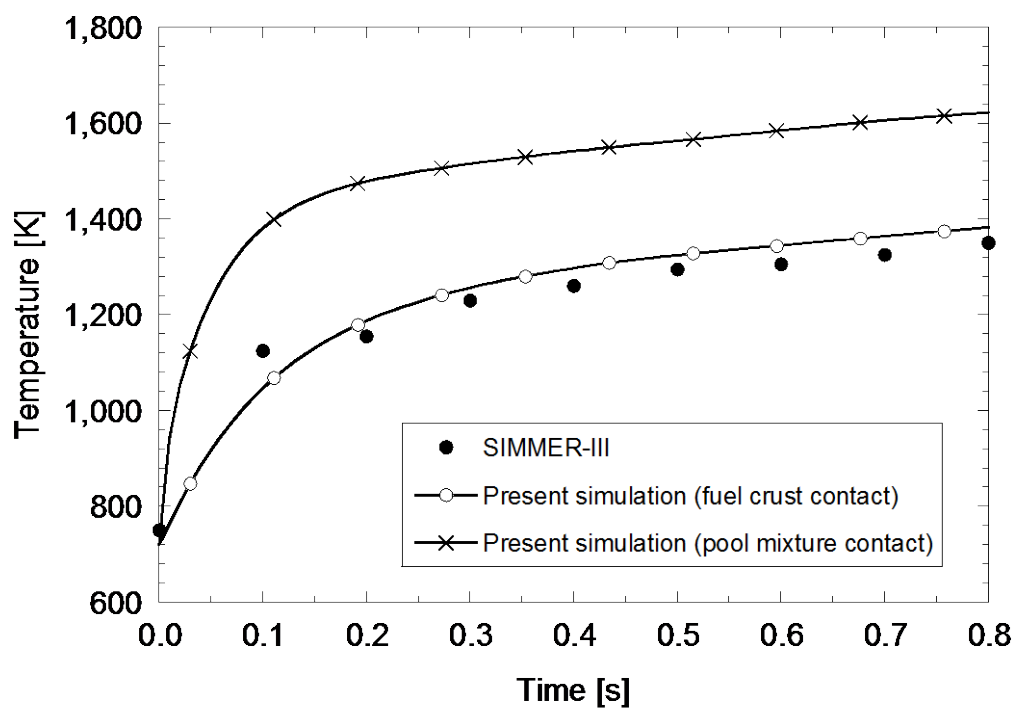
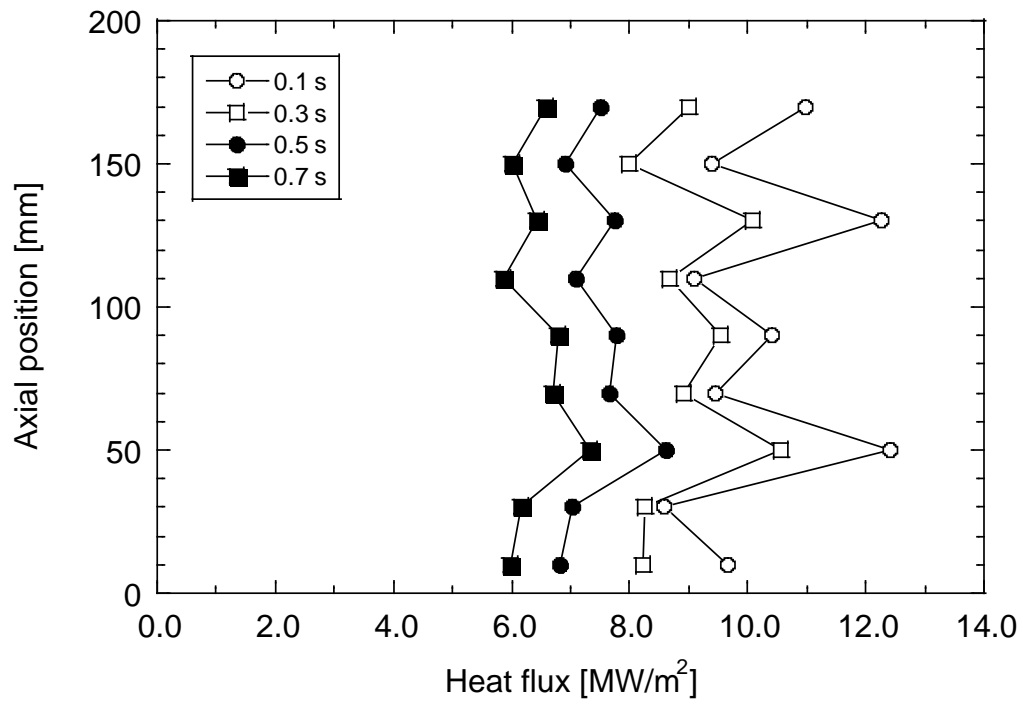
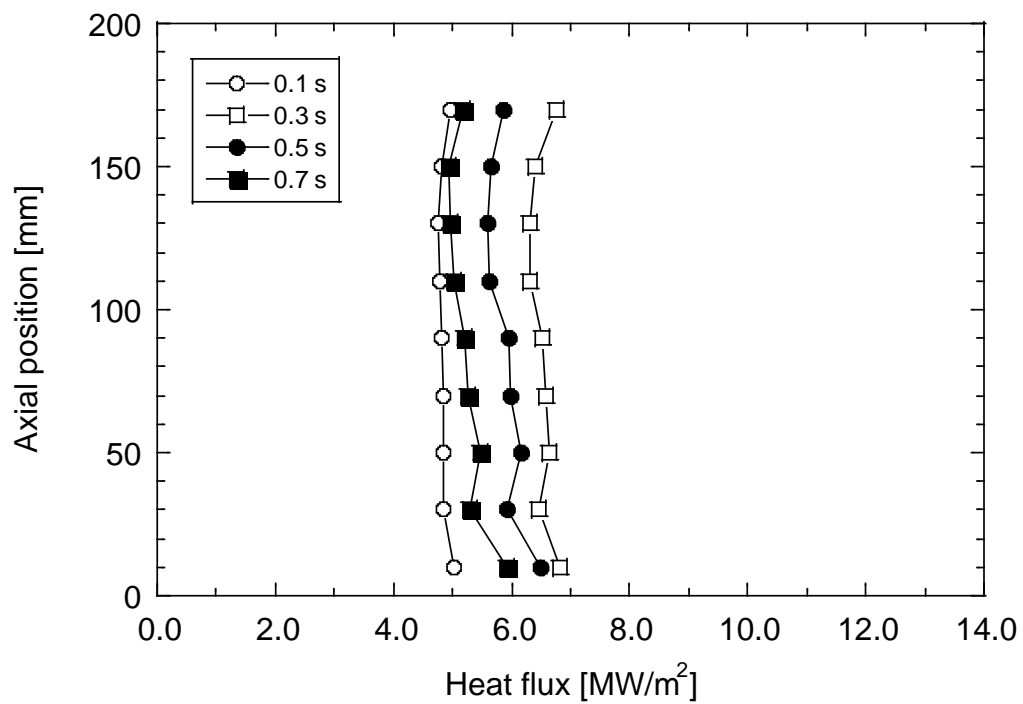


Figure 3.3-1 Duct-wall surface temperature after the start of pool-wall heat transfer.



(a) pool mixture contact



(b) fuel crust contact

Figure 3.3-2 Axial distributions of spatial average heat fluxes in the cases of pool mixture contact and fuel crust contact.

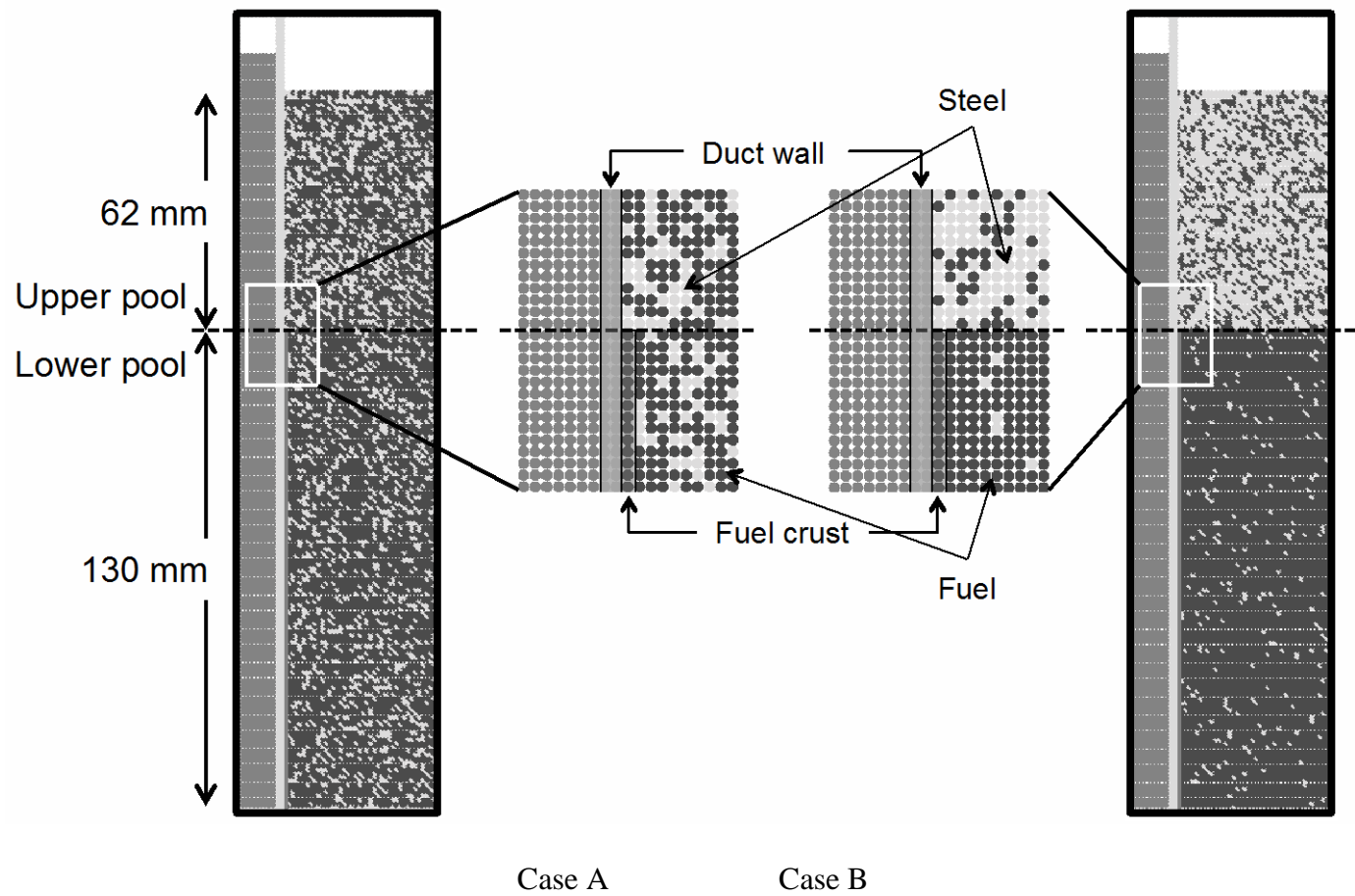


Figure 3.3-3 Initial material configurations in Cases A and B.

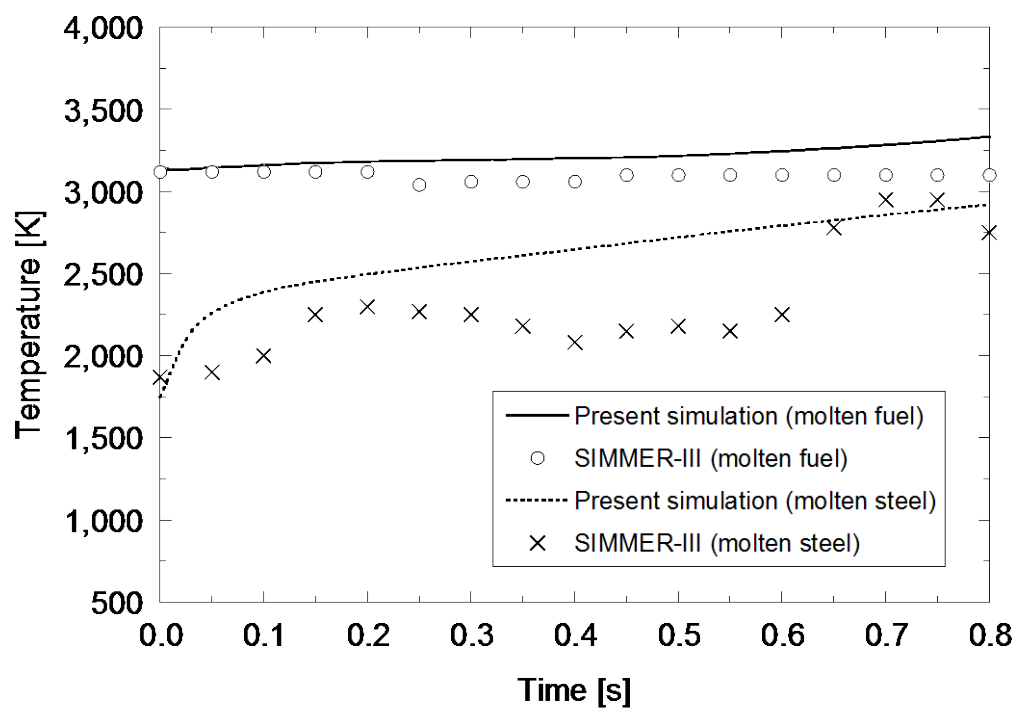
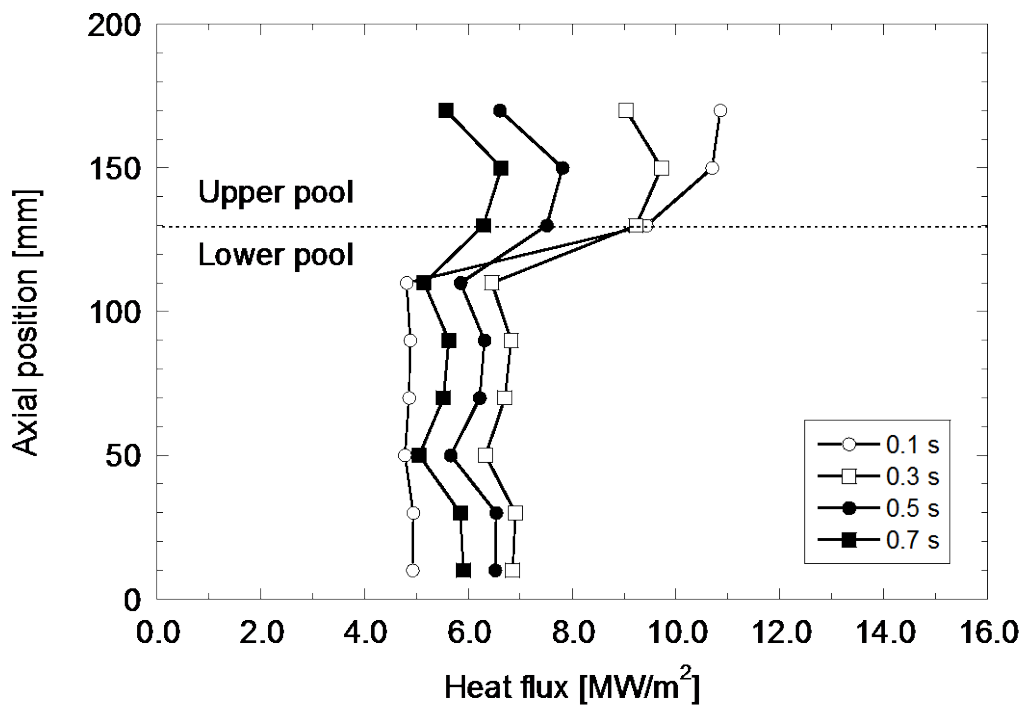
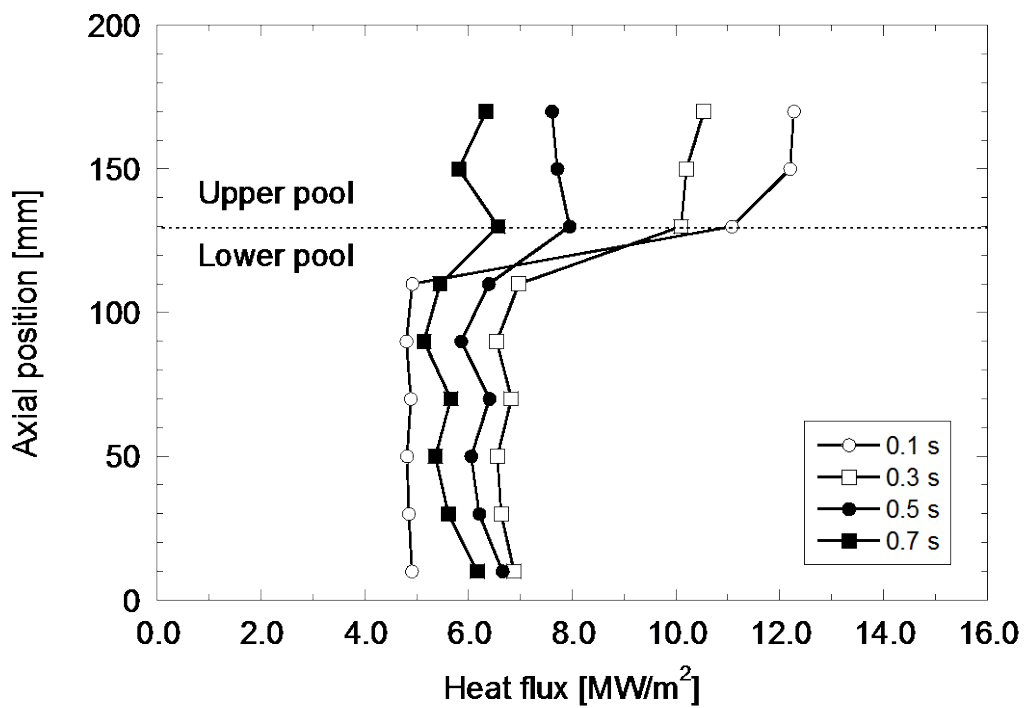


Figure 3.3-4 Time variations of average temperatures of molten fuel and steel in Case A.



(a) Case A



(b) Case B

Figure 3.3-5 Axial distributions of spatial average heat flux in Cases A and B.

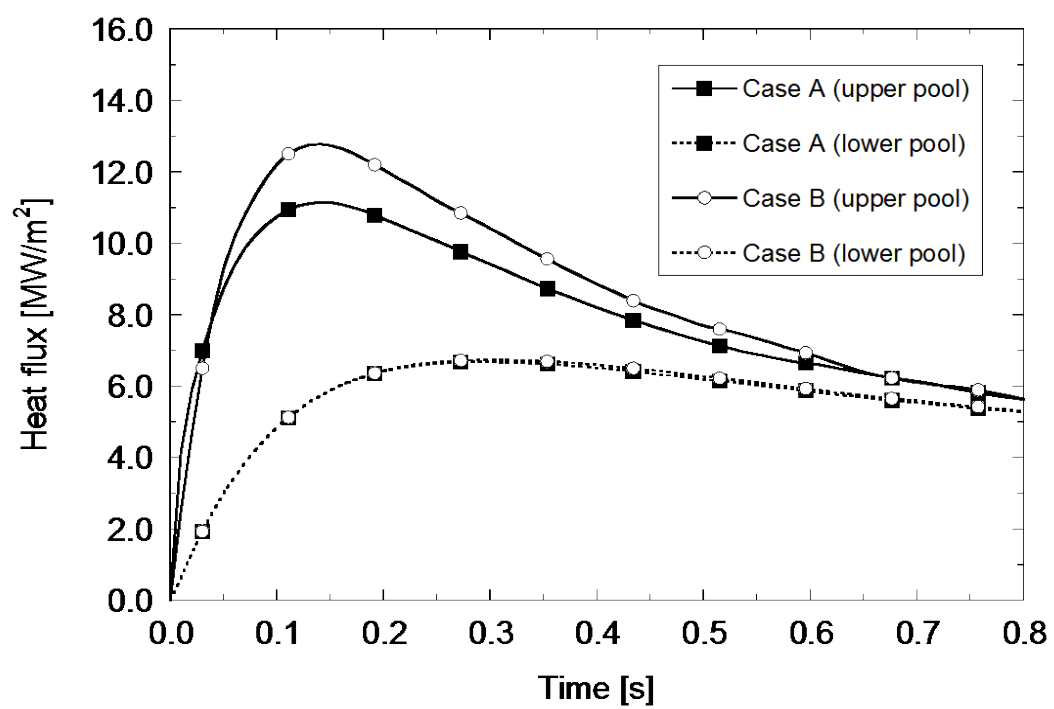
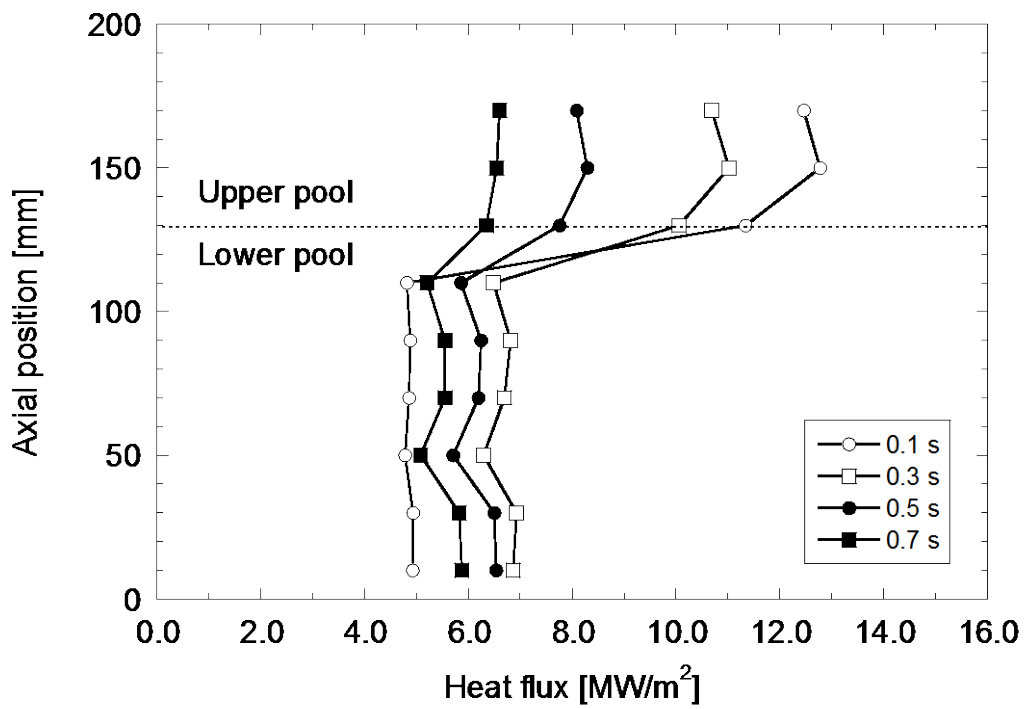
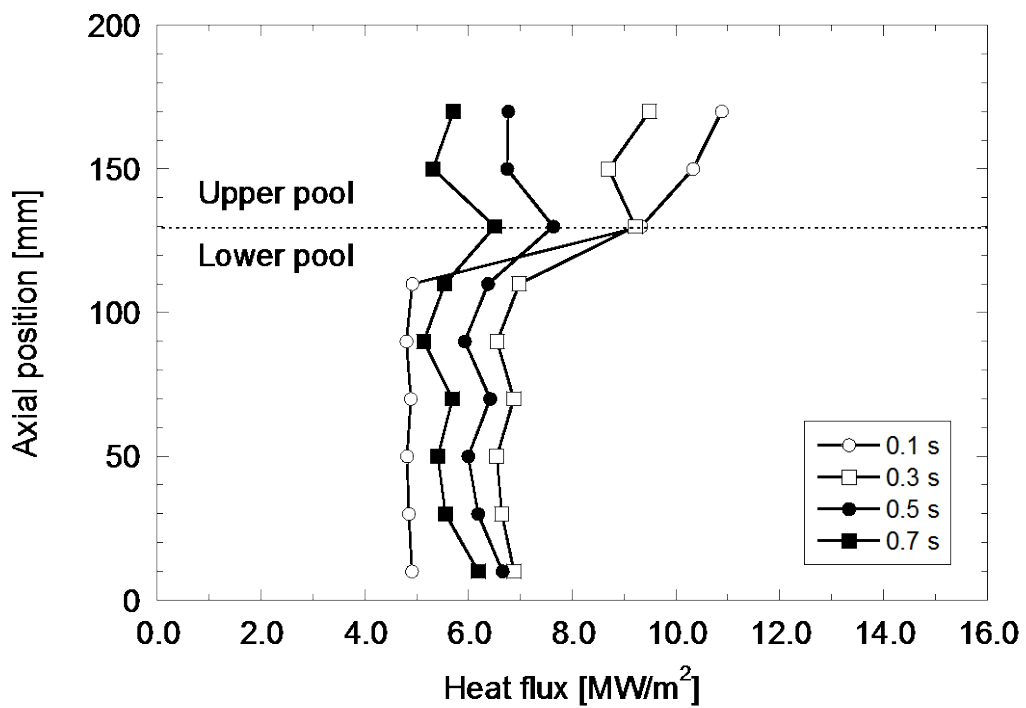


Figure 3.3-6 Time variations of upper- and lower-pool heat fluxes in Cases A and B.



(a) Case C



(b) Case D

Figure 3.3-7 Axial distributions of spatial average heat fluxes in Cases C and D.



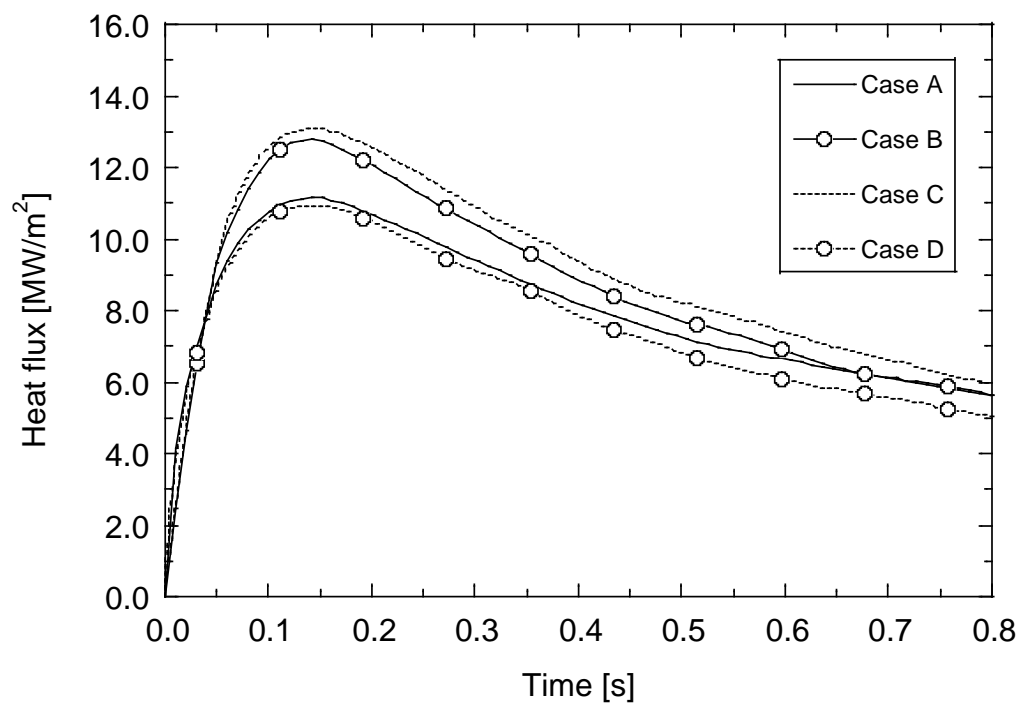
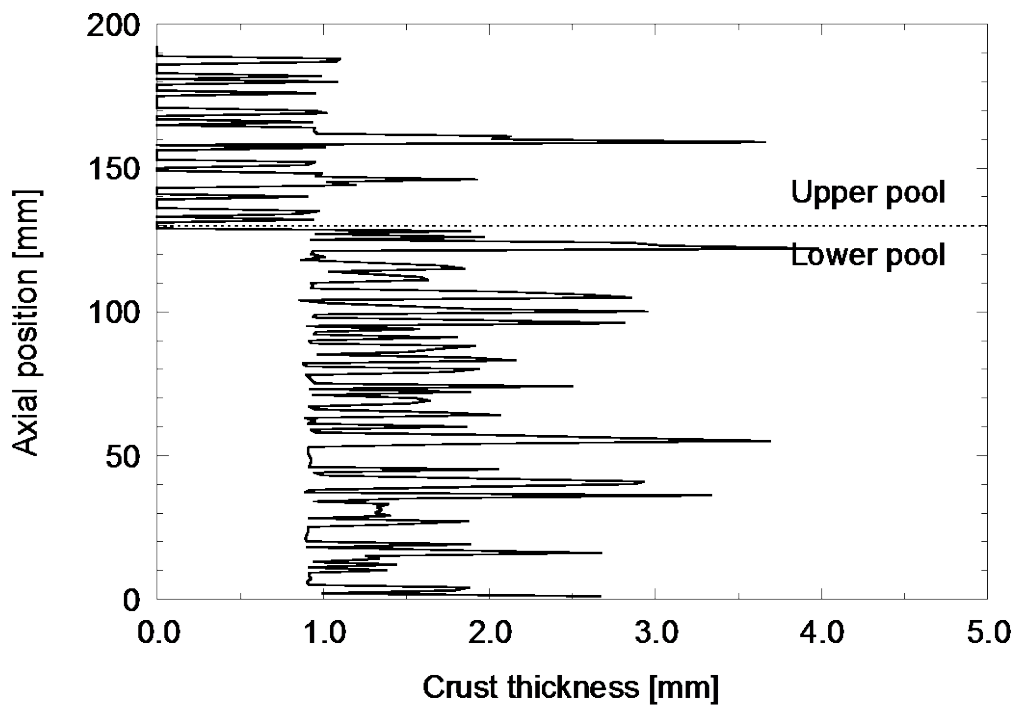
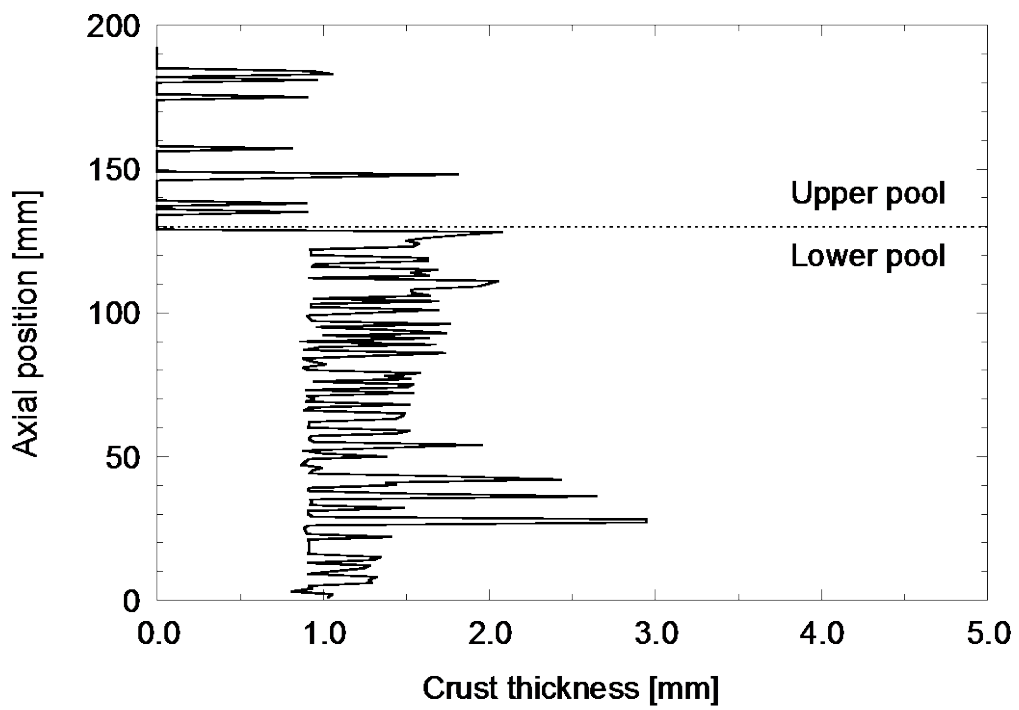


Figure 3.3-8 Comparison of upper-pool heat fluxes among Cases A, B, C and D.

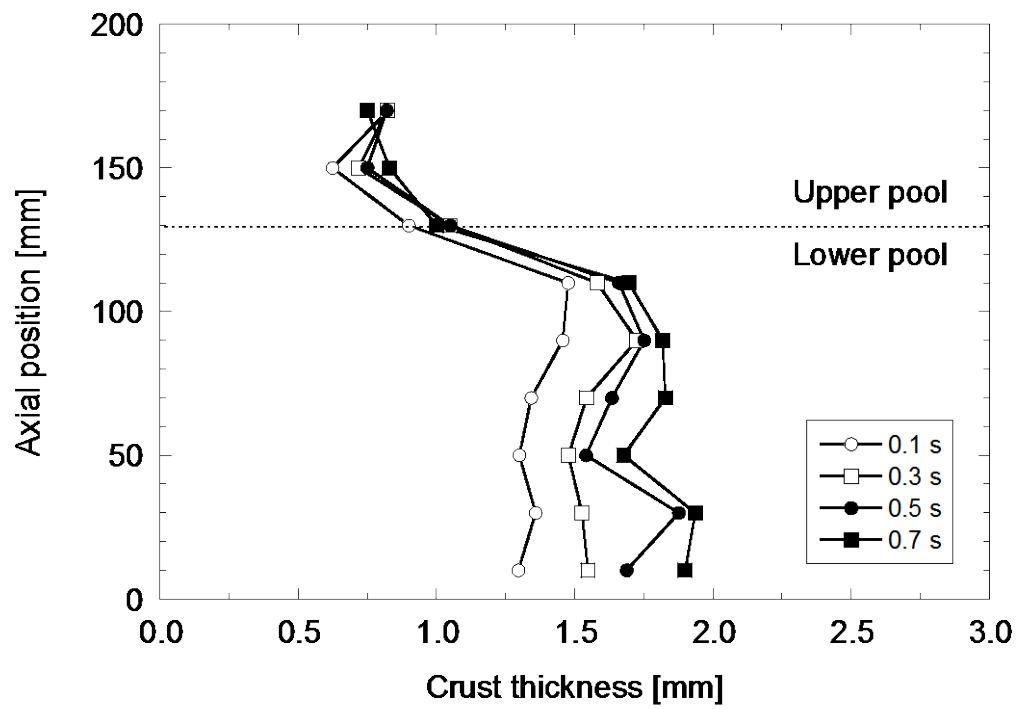


(a) Case A

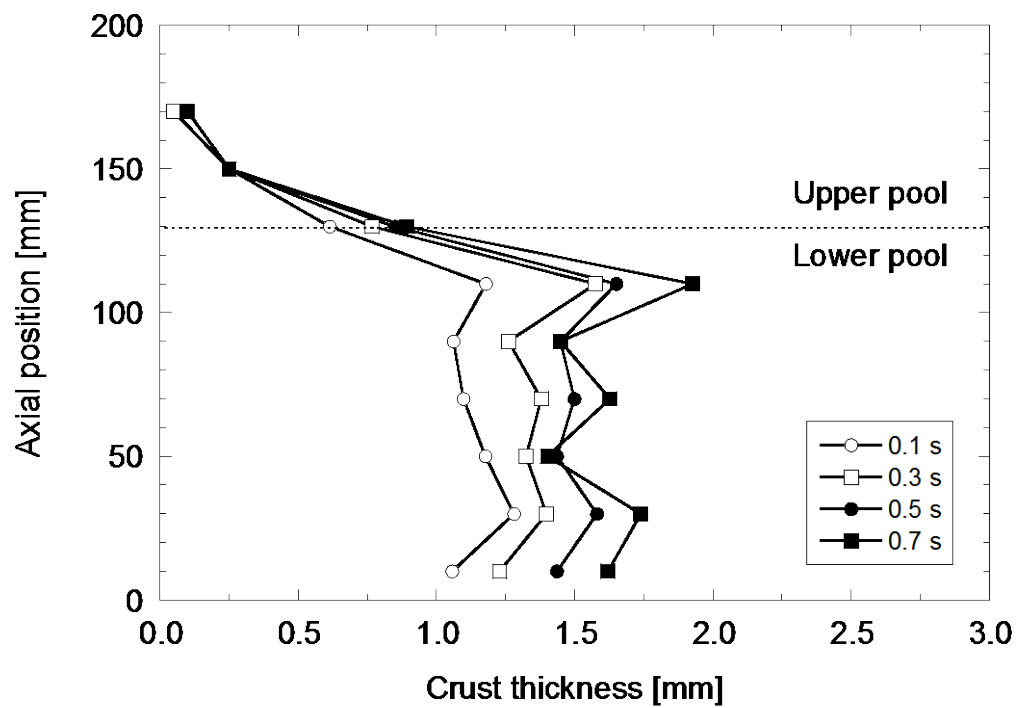


(b) Case B

Figure 3.3-9 Axial distributions of local crust thickness at 0.3 s in Cases A and B.



(a) Case A



(b) Case B

Figure 3.3-10 Axial distributions of spatial-average crust thickness in Cases A and B.

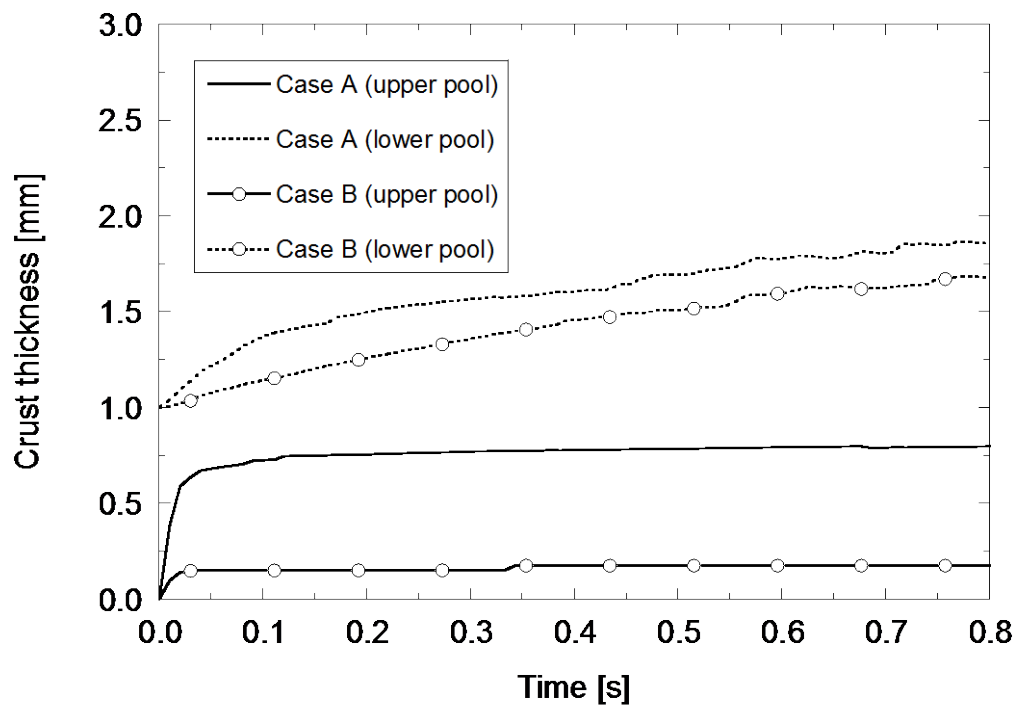


Figure 3.3-11 Time variations of upper- and lower-pool crust thickness in Cases A and B.

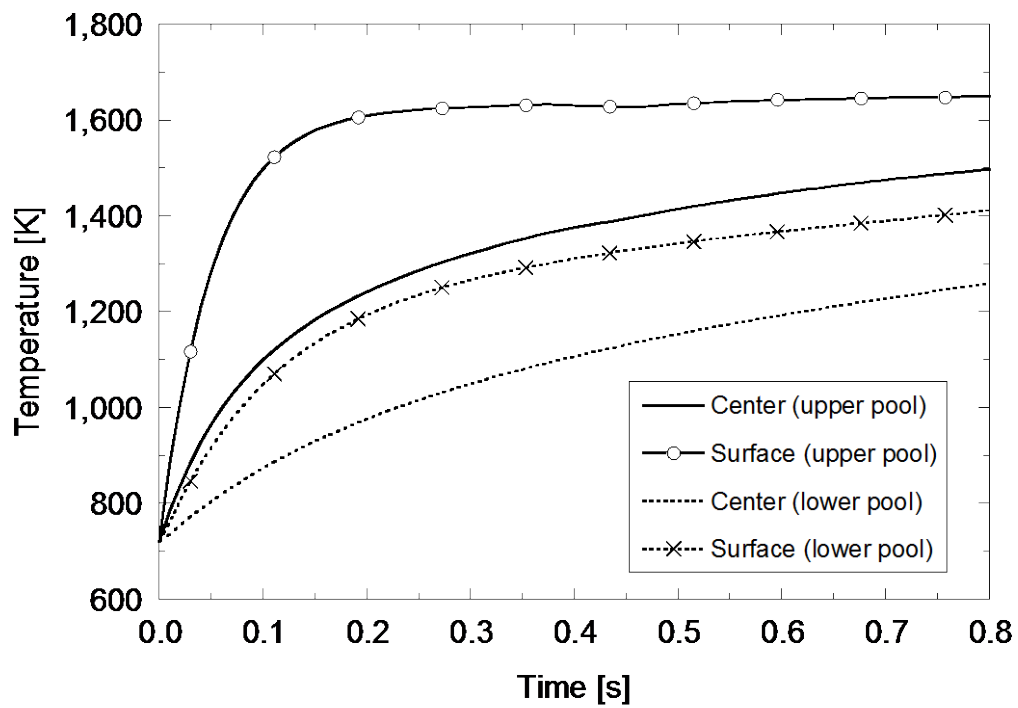


Figure 3.3-12 Time variations of duct wall temperatures in Case C.

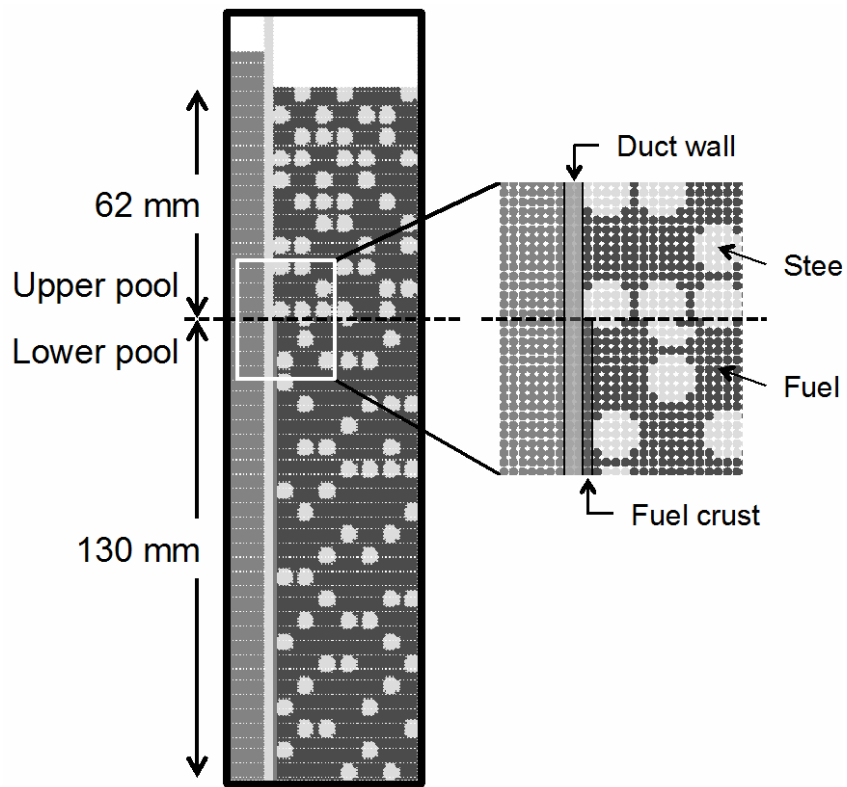


Figure 3.3-13 Initial material configurations in the case of larger steel droplets.

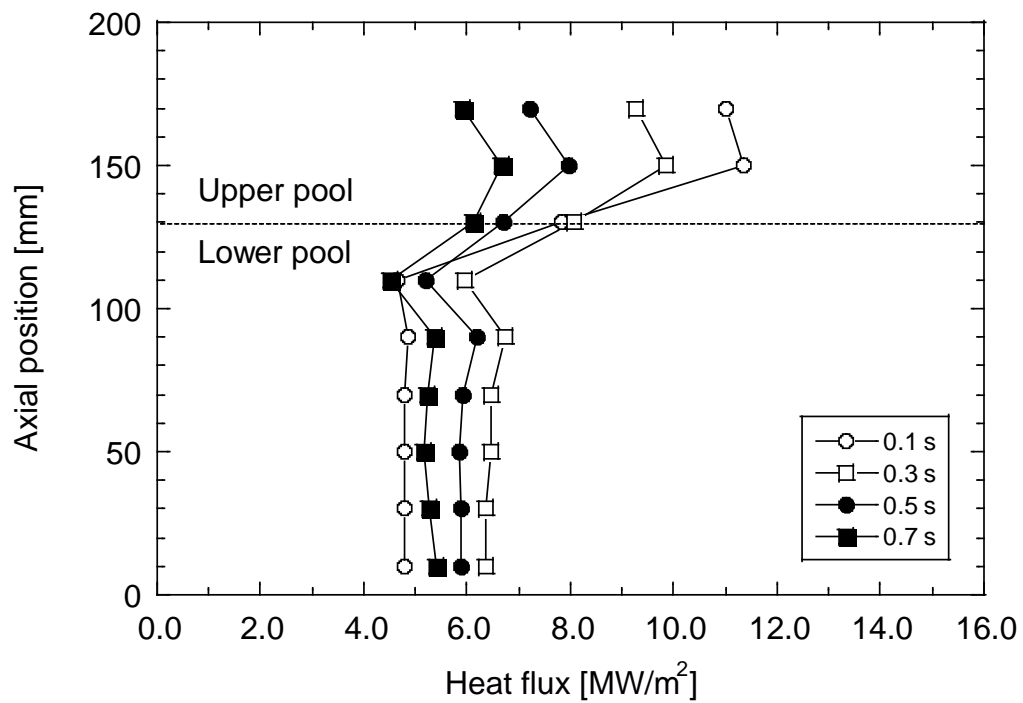


Figure 3.3-14 Axial distributions of spatial average heat fluxes in the case of larger steel droplets.

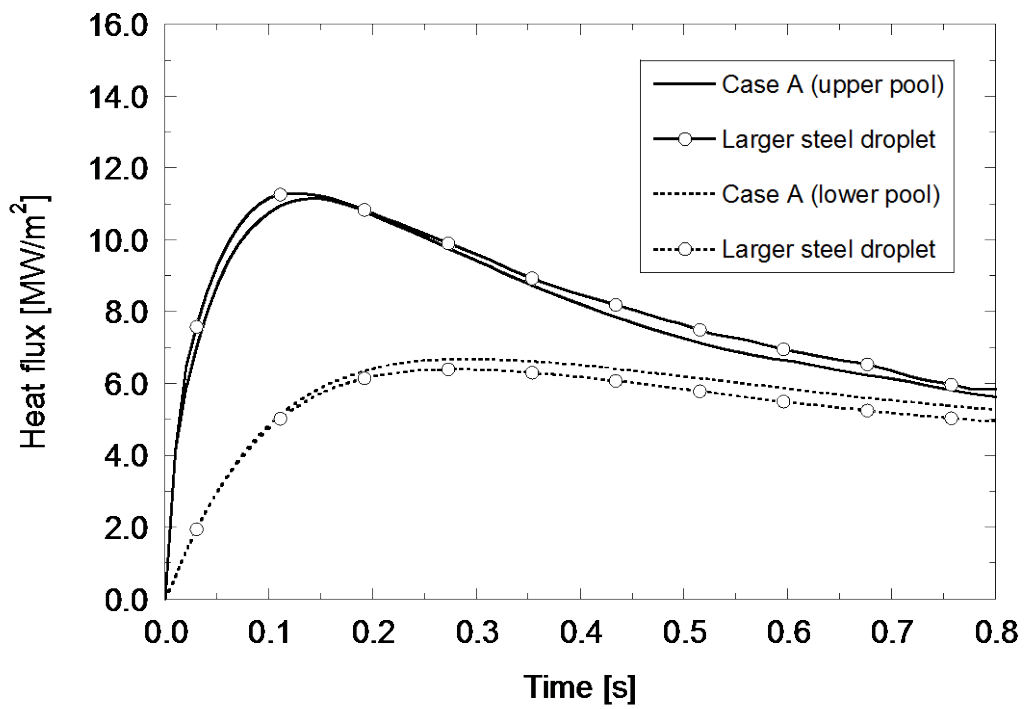


Figure 3.3-15 Comparison of upper- and lower-pool heat fluxes between Case A and the case with larger steel droplets.

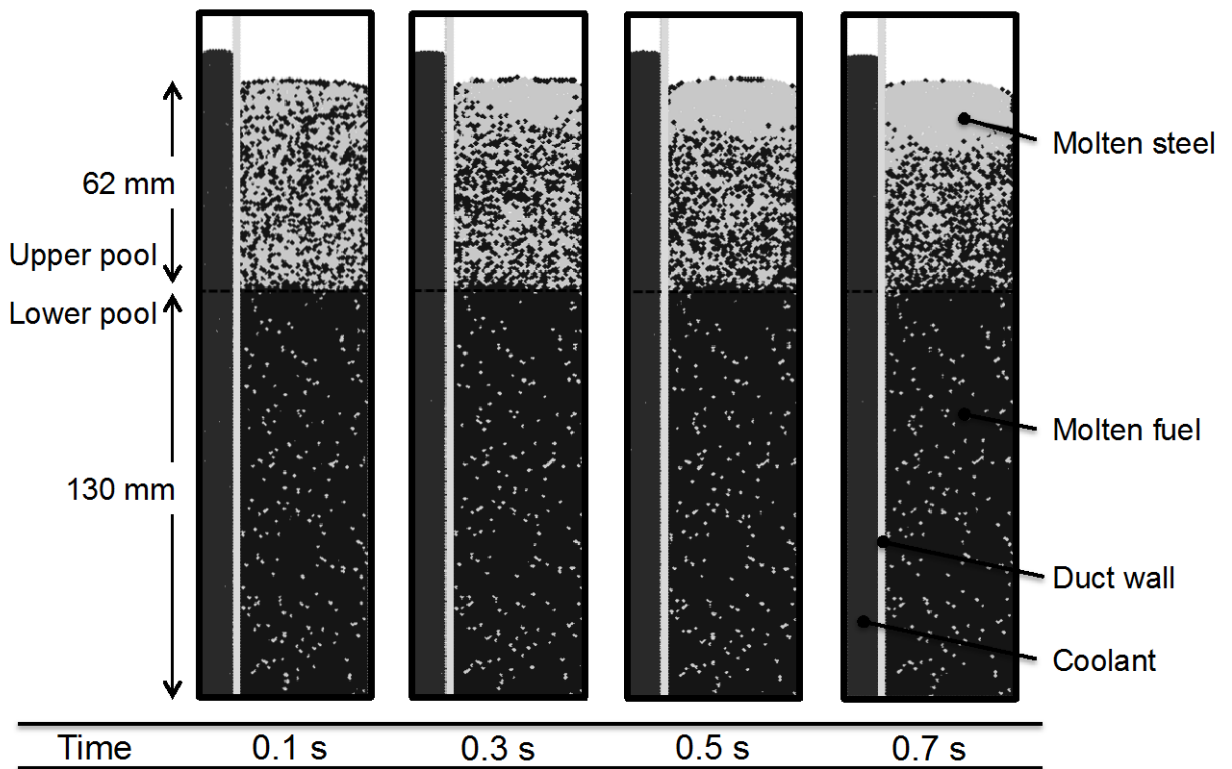


Figure 3.3-16 Material distribution in Case B with effective viscosity model

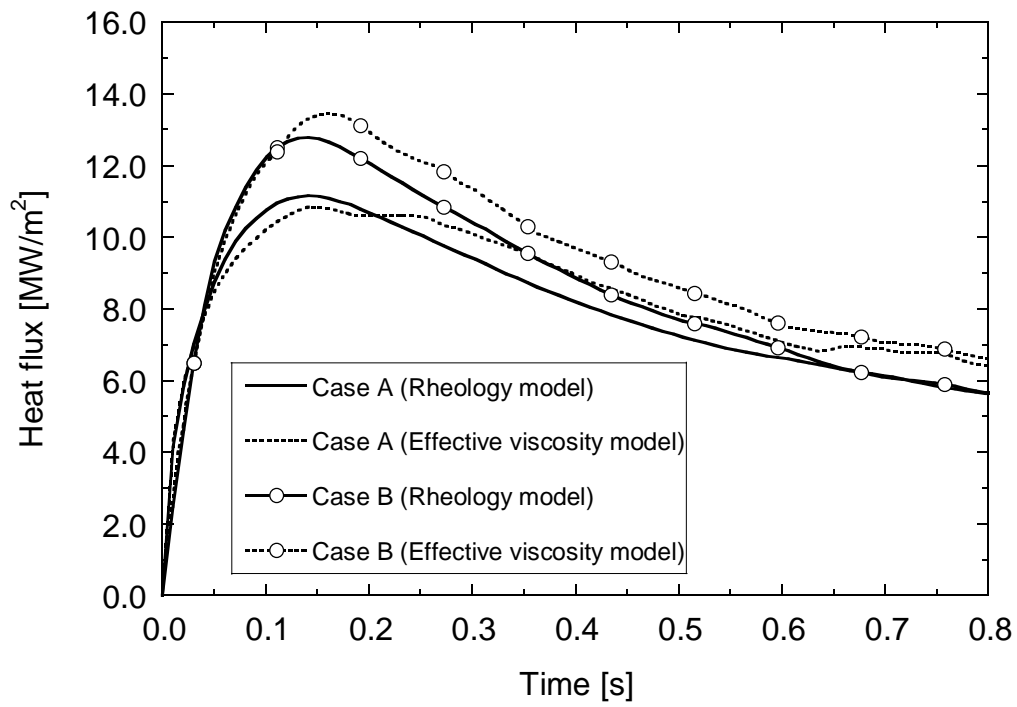


Figure 3.3-17 Comparison of upper-pool heat fluxes in Cases A and B

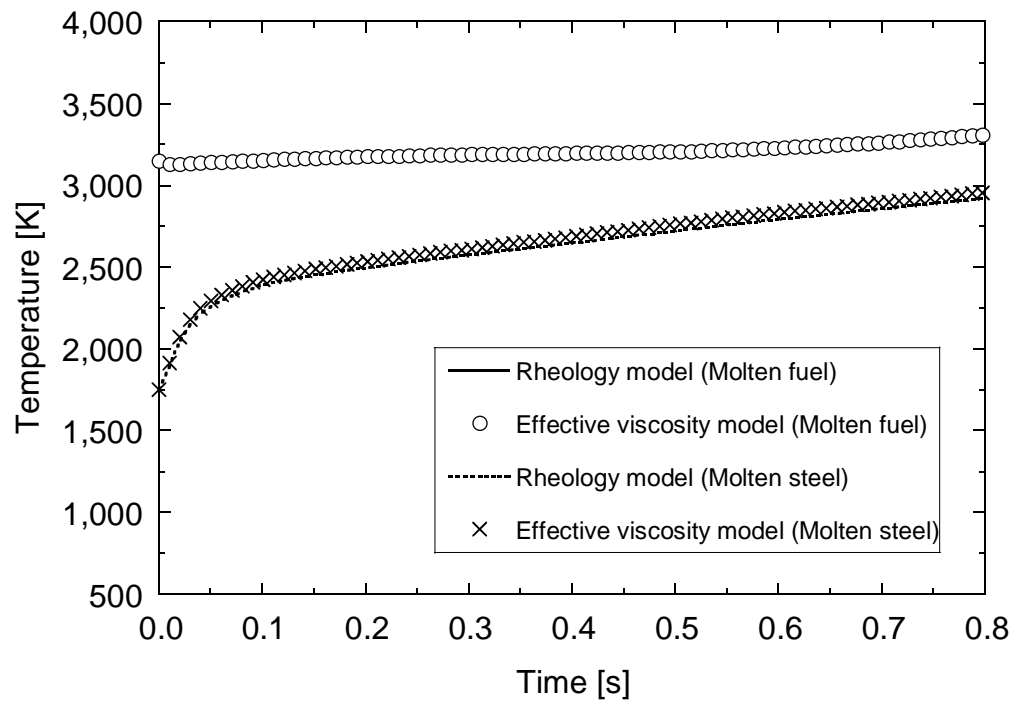


Figure 3.3-18 Time variations comparison of average temperatures of molten fuel and steel in Case A

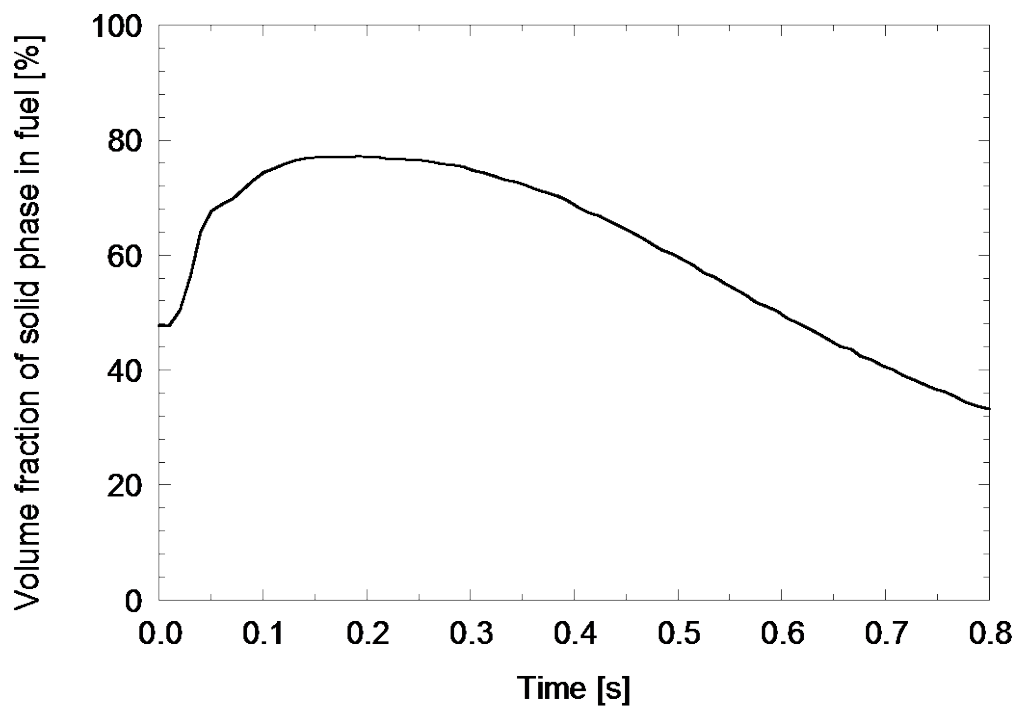


Figure 3.4-1 Time variation of solid-phase volume fraction in fuel in Case A.



## Chapter 4

### Analysis of Melt Freezing behavior

#### 4.1 Overview of pin bundle experiments

Many studies on freezing behaviors of molten core materials have been conducted to understand the thermal-hydraulic phenomena in CDA of LMRs. A series of melt freezing experiments was performed by Sonar *et al.* (2011) to investigate the fundamental characteristics of melt penetration and solidification in a narrow flow channel similar to a reactor bundle. In the experiments, a fusible metal of Bi-Sn-In alloy with a low melting point of 78.8 °C was used as a simulant melt, and a seven-pin bundle of stainless steel (SS) tubes was used as a flow channel. In addition to the melt of molten metal, its mixture with solid bronze particles with 0.5 mm in diameter were also used to measure the mixture penetration and freezing behavior under the influence of solid particles. Hereafter, the experiments using the fusible metal and its mixture with solid particles as a melt simulant are called the pure- and mixed-melt freezing experiments, respectively.

Figure 4.1-1 shows schematic diagrams of the melt freezing experiments in the seven-pin bundle. The apparatus consists of a flow channel, a melt holder, and a melt tank with a plug for melt release. The length of the flow channel was 500 mm. The annular pins, each closed off at the top, were encased by an outer glass tube to allow for visual observations. In the experiments, a thin fusible metal plate, also made of Bi-Sn-In alloy, with 0.5-mm thickness was initially set at the base of the melt holder to ensure smooth injection of melt into the flow channel. After obtaining the desired temperatures for both the pins and the melt, the plug of the melt tank was pulled up to release the melt into the melt holder as shown in Fig. 4.1-1 (a). As melting of the fusible metal plate, the melt

starts to penetrate into the channel downward under the influence of gravity. After the melt freezing in the channel, local melt penetration lengths at six subchannel positions in the pin bundle (see Fig. 4.1-1 (b)) were measured, and their average value was used to represent the penetration length of the bulk melt flow.

In previous study (Sonar *et al.*, 2011), numerical simulations were also performed using the SIMMER-III code (Tobita *et al.*, 2002). Although their simulations show reasonable agreement with observed experimental results, in general, Eulerian methods are limited in reproducing local freezing processes in detail because such methods cannot model interface phenomena directly. In addition, particular shapes of flowing molten metal cannot be represented by mesh methods. The present study is therefore aimed at simulating local meso-scale freezing and penetration behavior of melt flowing into narrow channel geometry in detail.

## **4.2 Modeling of pin bundle conditions**

In the present 3D particle-based simulation code, the main constitutive models to solve thermal-hydraulic phenomena of multiphase flows are formulated based on the previous works (Guo *et al.*, 2010; Mahmudah *et al.*, 2011). The surface tension force in Eq. (2.10) is expressed using a model based on the free surface energy (Kondo *et al.*, 2007). The interactions between liquid and solid phases are evaluated by solving Eq. (2.10) for both the liquid and solid phases. The phase change processes of melting and freezing are represented by a non-equilibrium model (Mahmudah *et al.*, 2011). The melt rheological behavior is represented by the apparent viscosity model, Eq. (2.39), which is formulated as a function of solid volume fraction.

In the present simulations of melt freezing experiments, the initial particle distance  $\Delta l$  was set to 1 mm, and the time step size was 0.1 ms. Figure 4.2-1 shows the geometric

setup for the present simulation of pure-melt freezing experiments. With the initial particle distance of 1 mm, one moving particle has a volume of  $10^{-3} \text{ cm}^3$ , and hence, the melt are represented by about 20,000 numerical particles for the melt mass of 175 g in the pure-melt freezing experiments. Each pin is represented by an annular tube of  $300 \times 64$  numerical particles corresponding to the length of 300 mm and the cross section, respectively. In the simulation of mixed-melt freezing experiments, the solid particles mixed with the molten metal, of which diameter is 0.5 mm, were represented approximately by twice-sized numerical particles. The present simulations did not model the heat transfer from the melt and the pin to the surrounding air because its effect on penetration and freezing behavior of melt should be negligibly small over the short time period that the present experiments took.

For the fluid dynamics calculation,  $2.1\Delta t$  was chosen for the cut-off radius  $r_e$ . In the fluid dynamics calculation, we applied homogeneous Neumann boundary condition to velocity divergences in determining the pressure for numerical particles on the free surface. The melt freezing experiments were simulated from melt release in the melt holder to stoppage of melt penetration in the flow channel. Initial homogeneous mixtures of molten metal with solid particles were assumed in the melt holder for the simulation of the mixed-melt freezing experiments. The initial velocity of the melt in the melt holder was set to zero and was allowed to fall gravitationally after melting of the fusible metal plate at the base of the melt holder.

Melt penetration into the seven-pin bundle is a typical characteristic of freezing behavior of melt flows. Its measured length was compared with simulation results. In the simulations, the penetration length is defined as the length of the melt at the six subchannel positions as measured in the experiments. Simulation conditions for pure- and mixed-melt freezing experiments are summarized in Table 4.2-1.

### 4.3 Simulation results and discussions

#### 4.3.1 Pure-melt freezing

The simulation was performed for the pure-melt freezing experiments using the molten metal of 175 g. The value of  $A'$  in Eq. (2.39) for the melt rheological behavior is determined from the simulation of the pure-melt experiments as  $8.5 \times 10$  by comparing results with experiments. Figure 4.3-1 shows the transient penetration length in Case P-2. In the initial stages, the transient penetration length increases and then after a certain time the increase in penetration gradually reduces until the melt completely freezes with no change in the penetration length. As can be seen from this figure, the present simulation fairly well reproduces the experimental result.

The simulation results of melt and its temperature distributions in the pin bundle are shown for Case P-2 in Fig. 4.3-2 by the images at different times after the start of melt release in the melt holder. Here, the images indicate the views in the central vertical section inside the pin bundle. After melting of the fusible metal plate at the base of the melt holder, melt penetration develops in the pin bundle with heat transfer from the hot melt to the cold pin structures. Due to the rheological effect of the melt, the resulting temperature decrease leads to an increase in the viscosity force suppressing the melt velocity. The slower melt movement leads to a smaller change in penetration length. When the melt temperature reaches the freezing point, the melt viscosity becomes very large and the melt will completely stop penetrating along the pin surfaces. Figure 4.3-3 shows a visual comparison of the frozen-melt shape in the pin bundle between the simulation and experiment in Case P-1. The simulation and the experimental results indicate reasonable agreement, although the simulation does not reproduce frozen melts in long needle shape observed at the melt front. This might be because spatial resolution

in the simulation is insufficient to represent such shape due to relatively larger numerical particles.

Figures 4.3-4 shows the penetration lengths of pure melt as a function of initial melt temperature in the range of 90-130 °C, indicating a slight increase with increasing melt temperature. On the other hand, the penetration lengths are seen to vary a bit largely with initial pin temperature in the range of 25-50 °C, as shown in Fig. 4.3-5. The simulation results of melt flow and freezing behavior, which is represented by the melt penetration length, show fairly good agreement with the experimental ones depending on the initial melt and pin temperatures. In the present simulation of the pure-melt freezing experiments, all the poured melt freeze in the flow channel and adhered on the pin surface without melt separation. This is also consistent with the experimental results.

#### *4.3.2 Mixed-melt freezing*

The simulation was performed for the mixed-melt freezing experiments using the mixture melt of 175 g including solid particles. The initial pin and melt temperatures were 25 °C and 100 °C, respectively. Figure 4.3-6 shows that the melt penetration length of mixed melt decreases with increasing solid particles volume fraction in the range of 0-30%. The higher volume fraction of bronze particles with higher thermal conductivity might also enhance the effective thermal conductivity of the mixed melt. Although the present simulation underestimate the penetration lengths compared with the experimental ones, the tendency of their decrease with increasing particle fraction well reproduced under the effects of solid particles in the melts. Figure 4.3-7 shows a visual comparison of the frozen-melt shape in the pin bundle between the simulation and experiment in Case M-3. The simulation result indicates comparable agreement with the experimental one.

Typical simulation results are presented in Fig. 4.3-8 for the case of 30% volume fraction of solid particles in the mixture (Case M-3). In this figure, melt and its

temperature distributions in the pin bundle are indicated by the images at different times after the start of melt release in the melt holder. Figure 4.3-9 shows the downstream distribution of solid-particle volume fraction in the case corresponding to Fig. 4.3-8. As can be seen in these figures, particle rich regions develop locally around the leading surface of the bulk melt flow, and particle concentration in the mixture also increases in the downstream direction during the melt penetration and freezing. This behavior might lead to some contribution to the formation of tight blockage in the flow channel. Figure 4.3-10 presents the comparison of melt mass distribution in the downstream direction between the pure- and mixed-melt freezing simulations in Cases P-1 and M-3, respectively. The mixed melt causes tighter blockage because the solid particles of bronze with higher thermal conductivity could enhance the heat transfer from the hot mixture to the cold pin structures.

Figure 4.3-11 shows the visual information of material distribution in the cross section of the pin bundle and the radial distribution of solid-particle volume fraction around the central pin, which are integrated along the downstream direction at 0.4 s. There is also some local difference even in the radial distribution of particle concentration. The fusible metal component of the mixed melt tends to form a layer around the pin surfaces, while a particle rich region develops at the middle of the gaps in the pin bundle.

In the mixed-melt freezing experiments, a certain amount of the mixed melt separated from the bulk melt flow without adhesion on the pin surface. This melt separation is mainly due to fact that the pure melt can readily freeze onto pin surfaces but particles cannot. As a result, as molten metal freezes and mixed melt continues to fall, particle concentrations increase in downstream portions of the melt. Higher particle concentrations in the separated melt were also found than in melt adhesions. The above discussion based on the local behaviors of mixed-melt penetration and freezing shown in

Figs. 4.3-8 – 4.3-11 supports this experimental observation and consideration.

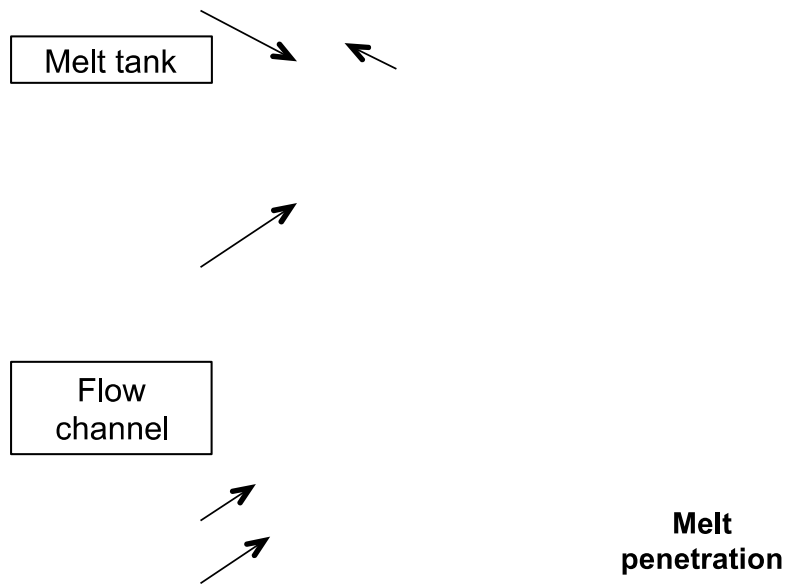
Figure 4.3-12 indicate a comparison of the mass separated from the bulk melt flow between the experiment and the simulation. In the experiments, the separated melt mass increases with increasing volume fraction of solid particles in the mixed melt, while the present simulation does not represent well this characteristic of the melt separation observed in the experiments. The melt separation behavior might relate strongly to interactions between the molten metal and the solid particles such as surface tension force. In the present simulation, however, the solid particles mixed with the molten metal were modeled by twice-sized numerical particles. This inconsistency might result in poor simulation of the melt separation behavior. On the other hand, the melt penetration lengths comparable with the experimental results are reproduced as shown in Fig. 4.3-6. These contrary results suggest that the melt penetration length depends mainly on the mass of molten metal, but not on that of solid particles in the mixed melt.

Further improvement of the present simulations would be necessary to reproduce the melt separation behavior observed in the mixed-melt freezing experiments under much reasonable simulation conditions.

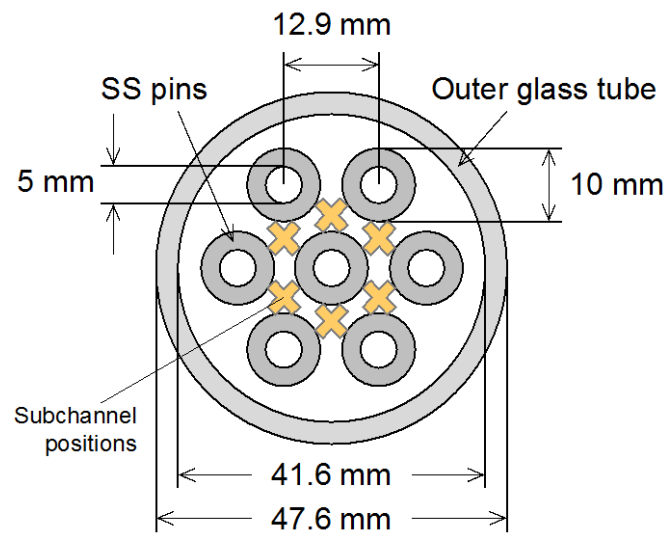
Table 4.2-1 Simulation conditions for pure- and mixed-melt freezing experiments

Case	Initial temperature [°C]		Volume fraction of solid particles [%]
	Melt	Pin	
P-1	100	25	0
P-2	110	25	0
P-3	130	25	0
P-4	100	35	0
P-5	100	45	0
M-1	100	25	10
M-2	100	25	20
M-3	100	25	30





(a) Side sectional view and experimental procedure



(b) Cross sectional view of flow channel

Figure 4.1-1 Schematic diagrams of melt freezing experiments in seven-pin bundle

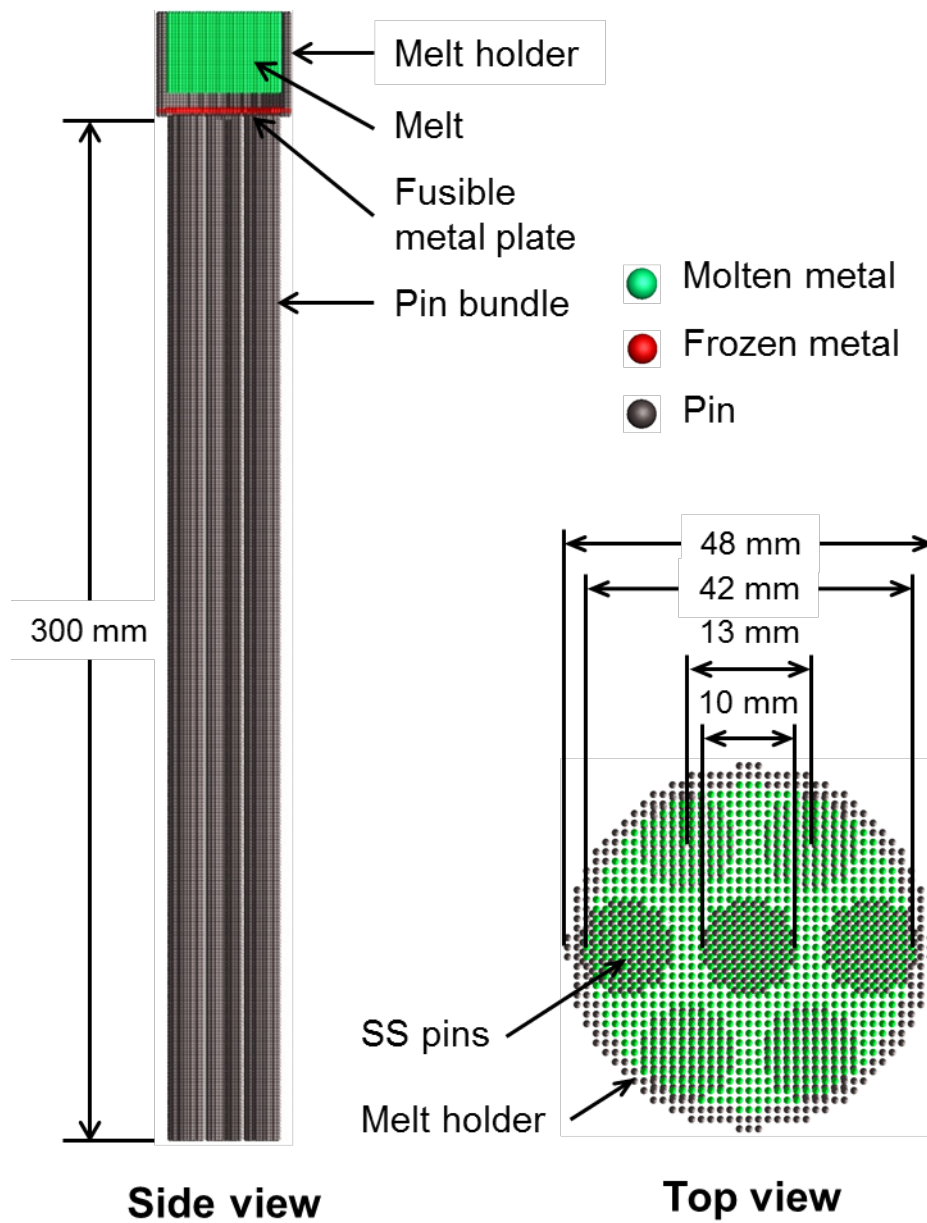


Figure 4.2-1 Geometrical setup for simulation of pure-melt freezing experiments

tial pin temperature : 25 °C

Figure 4.3-1 Transient penetration length in the case of pure melt (Case P-2)

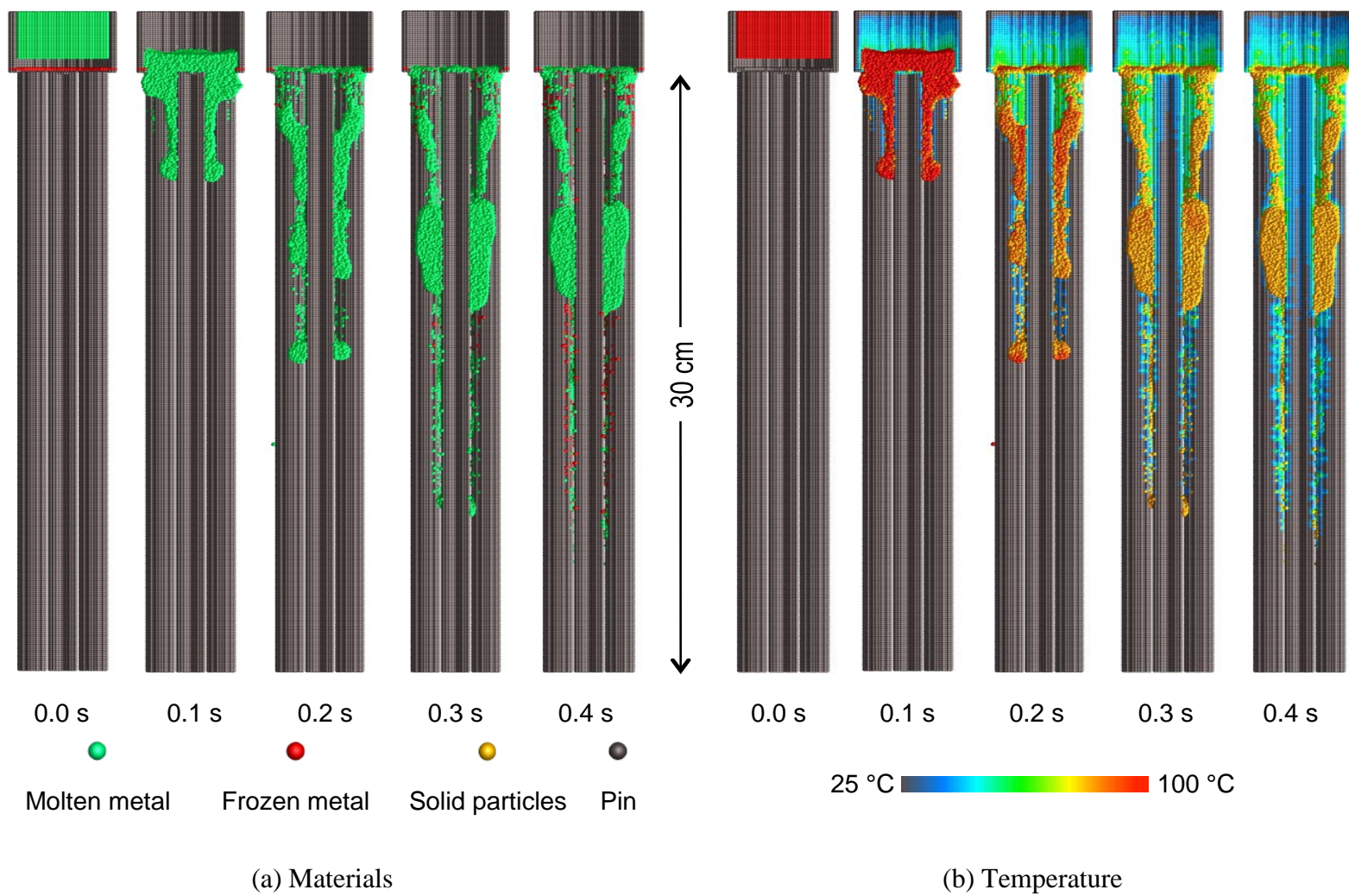


Figure 4.3-2 Simulation results of melt and its temperature distributions in the case of pure melt (Case P-2)



Figure 4.3-3 Comparison of frozen melt shape between experiment and simulation in the case of pure melt (Case P-1)

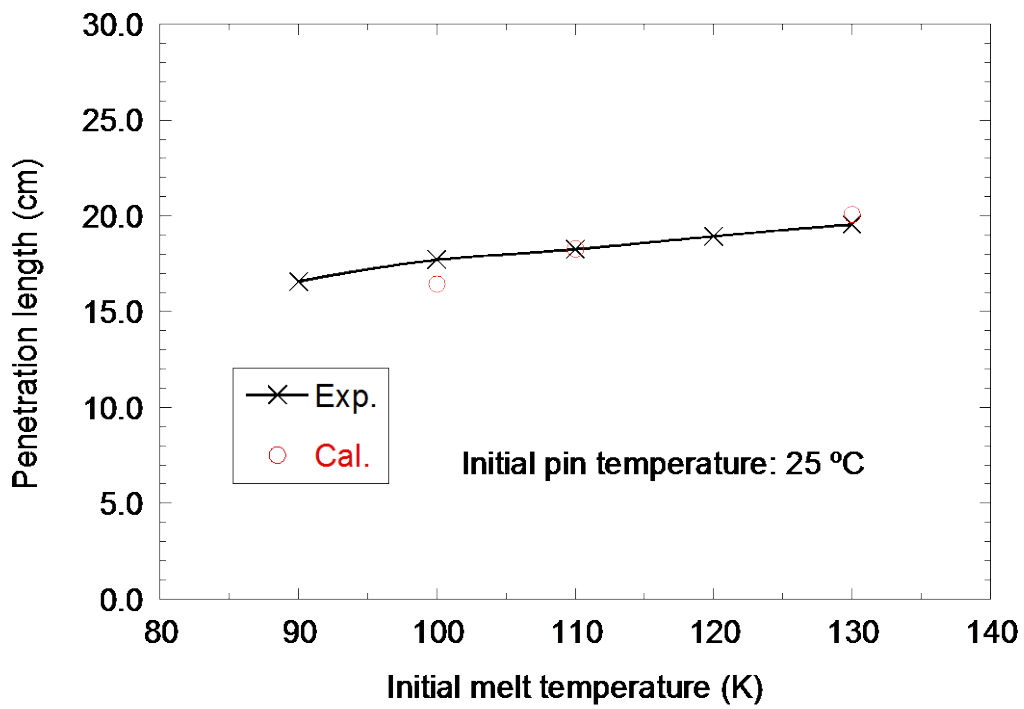


Figure 4.3-4 Penetration lengths at different initial melt temperatures in the case of pure melt (initial pin temperature: 25 °C)

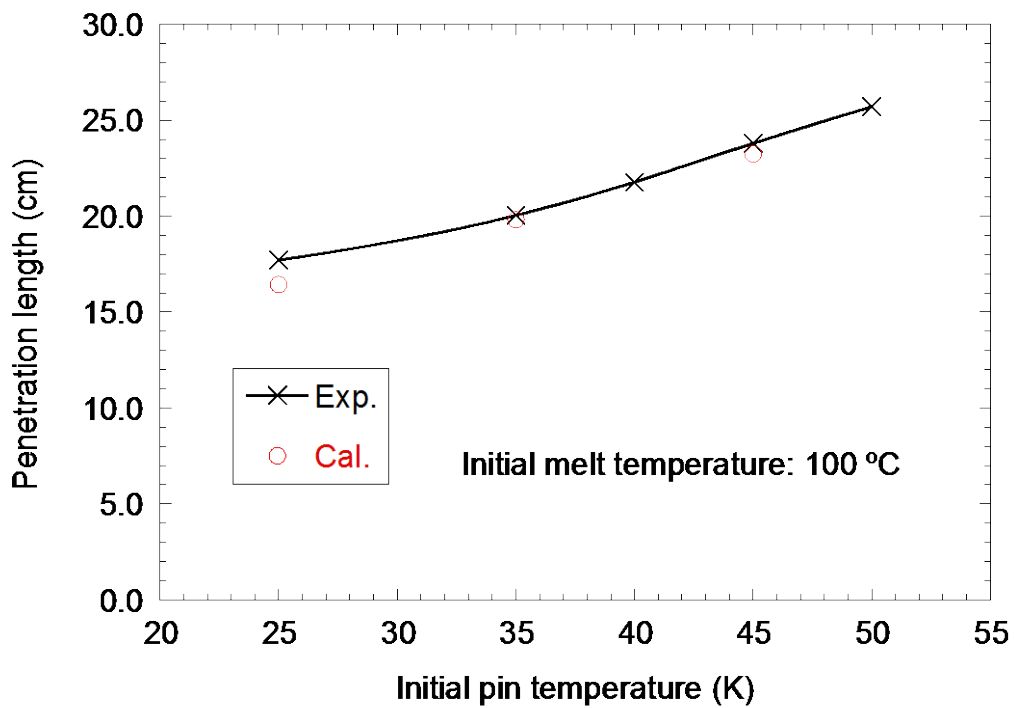


Figure 4.3-5 Penetration lengths at different initial melt temperatures in the case of pure melt (initial melt temperature: 100 °C)

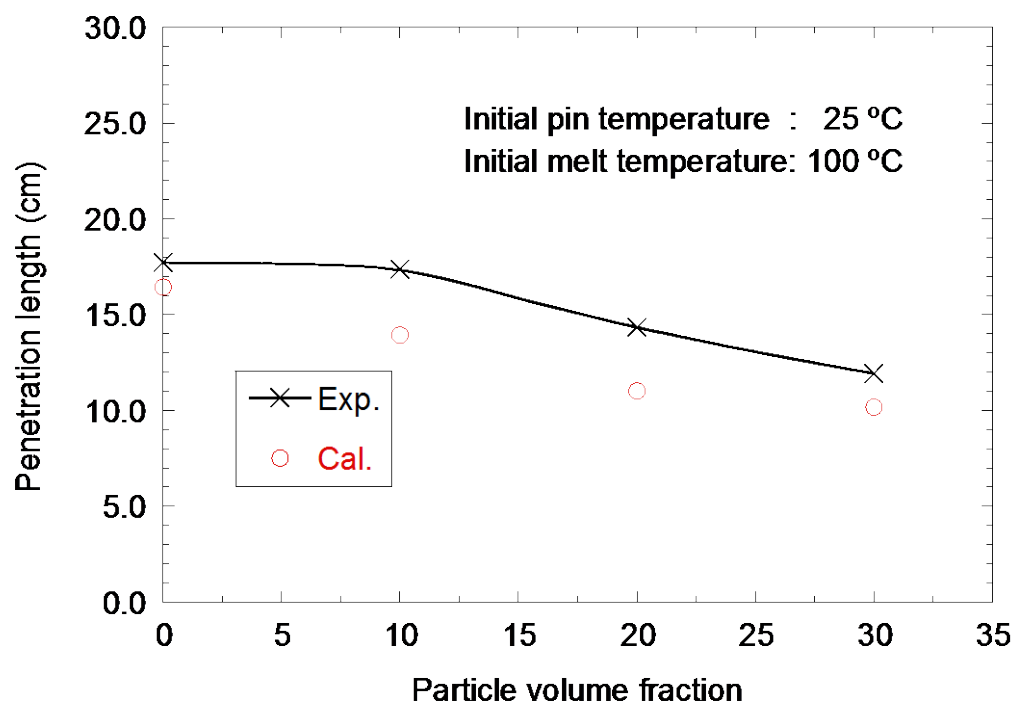


Figure 4.3-6 Penetration lengths at different volume fraction of solid particles in melt  
(initial pin temperature: 25 °C; initial melt temperature: 100 °C)

←→ Average penetration length: 11.9 cm



←→ Average penetration length: 10.2 cm

Figure 4.3-7 Comparison of frozen melt shape between experiment and simulation in the case of mixed melt (Case M-3)



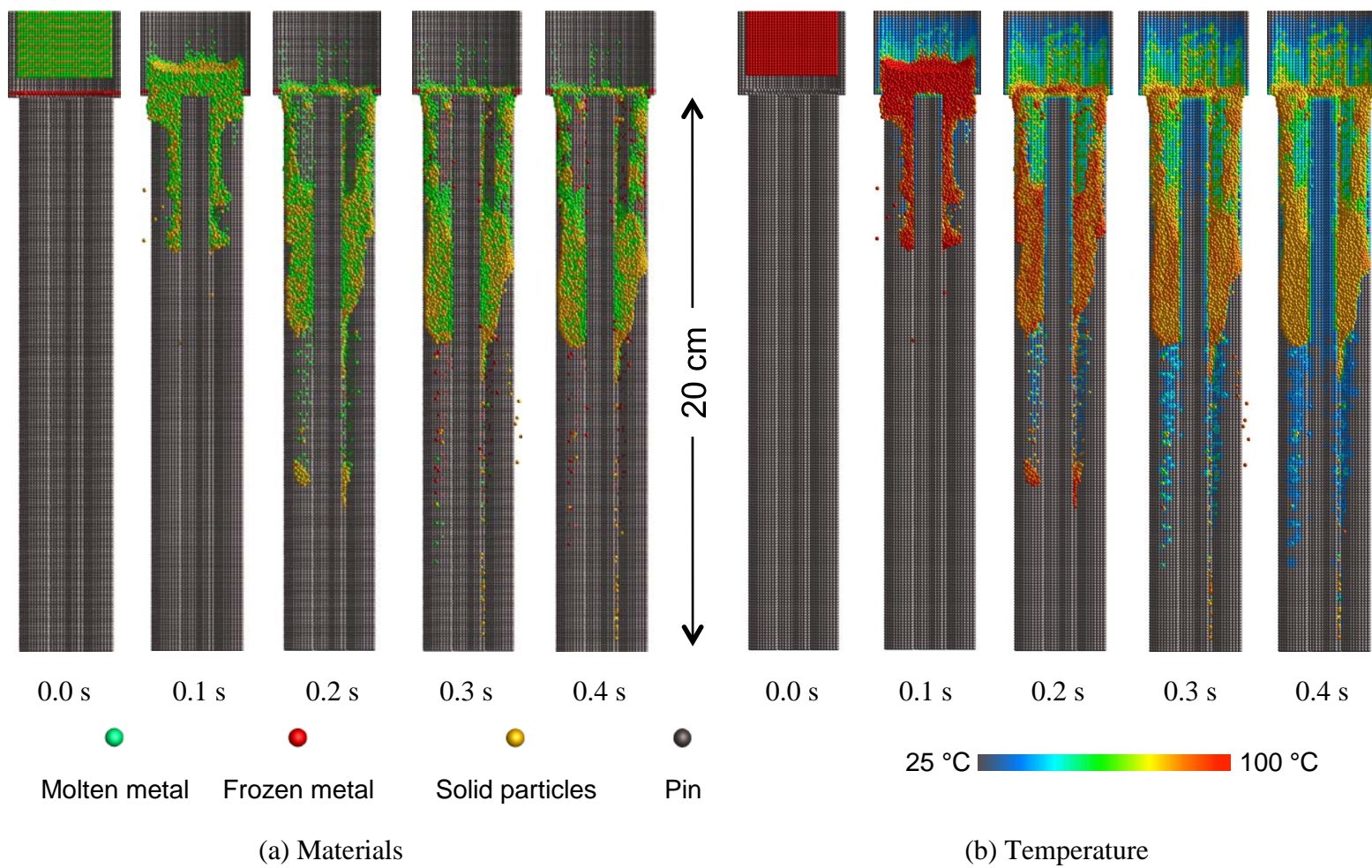


Figure 4.3-8 Simulation results of melt and its temperature distributions in the case of mixed melt (Case M-3)

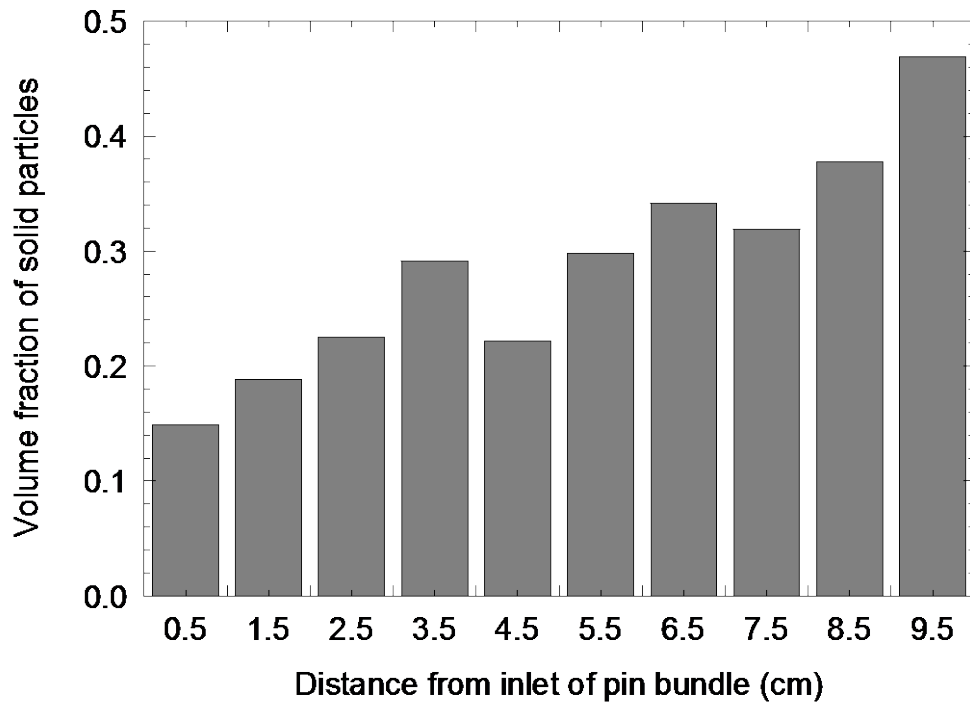


Figure 4.3-9 Downstream distributions of solid particles in mixed melt (Case M-3)

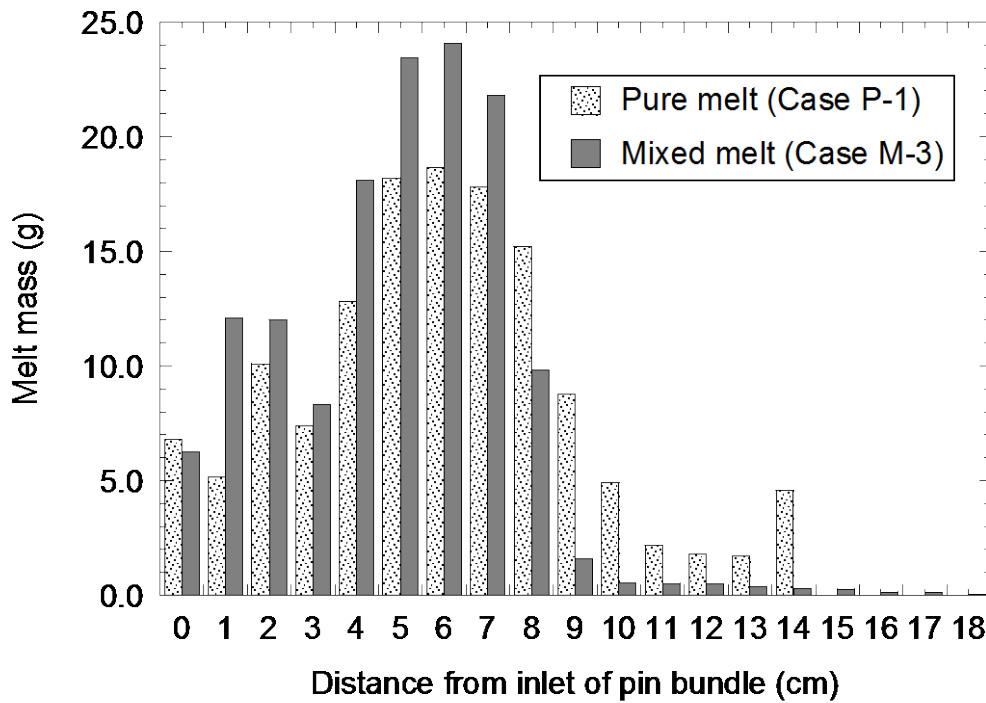
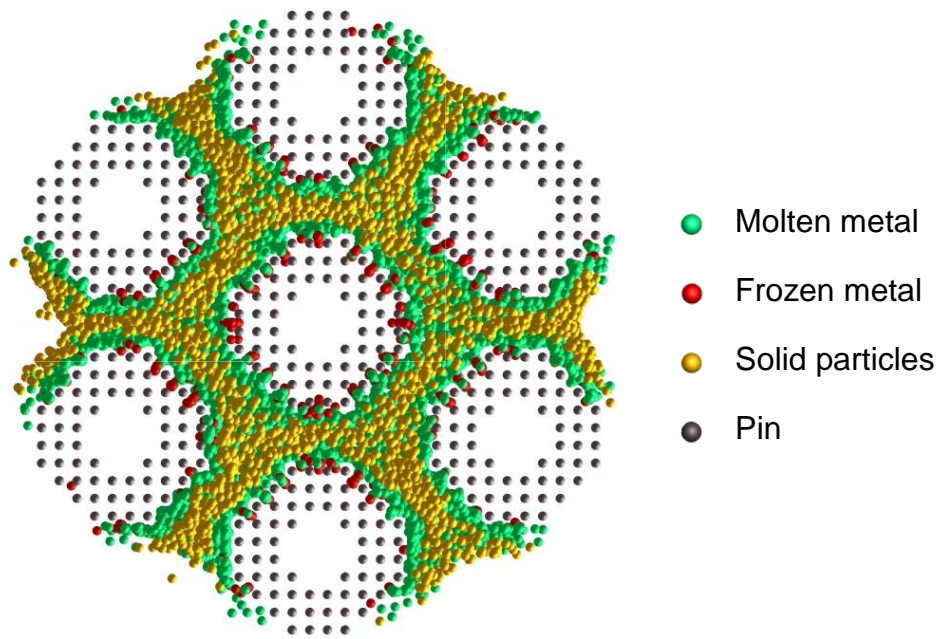
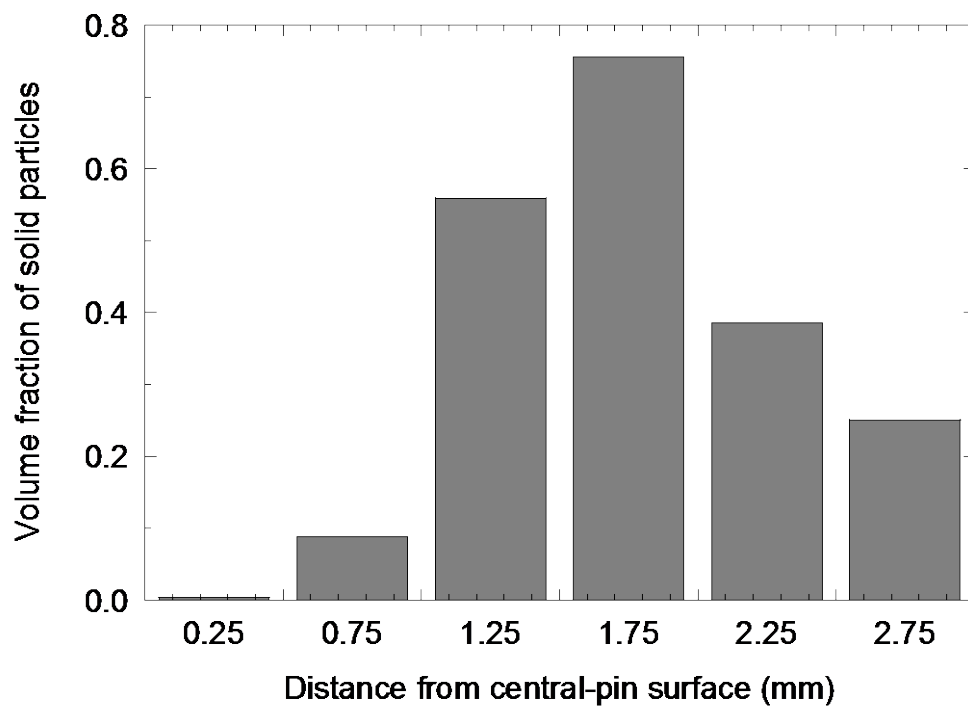


Figure 4.3-10 Comparison of downstream distribution of melt mass between Cases P-1 and M-3



(a) Visual image of material distribution



(b) Radial distribution of solid particles around central pin

Figure 4.3-11 Cross-sectional distributions of materials at 0.4 s (Case M-3)

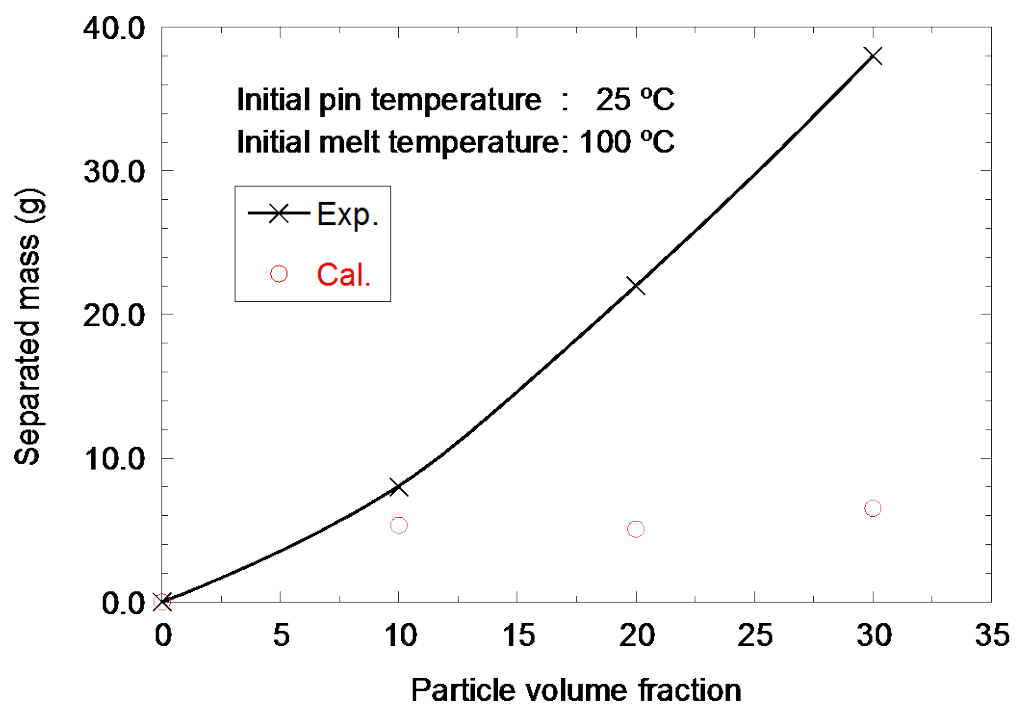


Figure 4.3-12 Separated mass at different volume fraction of solid particles (initial pin temperature: 25 °C; initial melt temperature: 100 °C)

## Chapter 5

### Conclusions

In this study, fully Lagrangian simulations based on the finite volume particle method for multi-component, multi-phase flows have been performed to analyze a set of heat transfer processes after the formation of fuel/steel mixture pool in the EAGLE in-pile ID1 test, and local meso-scale freezing and penetration behavior of melt flowing into narrow channel geometry in a seven-pin bundle. The main outcome of the present study is summarized as follow:

1. The simulation methods used for the analyses of the EAGLE in-pile ID1 can represent key thermal hydraulic behaviors involved in local thermal attack of the molten pool mixture to the duct wall, fuel crust formation on the wall surface and so on without empirical models such as flow regime map and heat-transfer correlations;
  - a. Mechanisms of effective heat transfer from the molten pool to the duct wall were clarified through parametric simulations on material distribution in the molten pool after its formation.
  - b. The simulation results indicate that effective pool-to-duct wall heat transfer is caused by local contact of molten steel with high thermal conductivity to the duct wall. As a result, the duct wall is exposed by large thermal load with heat flux more than 10 MW/m<sup>2</sup>, which is driven by nuclear heat in the fuel.
  - c. Although the molten fuel can freeze on the duct wall surface as crust, it would not deteriorate the pool-to-duct wall heat transfer largely due to its local and discrete formation.

- d. The present results ensure a better phenomenological understanding of the duct wall failure leading to early fuel discharge from a fuel subassembly with an inner duct structure (FAIDUS), which is the design measure to prevent severe re-criticality events during core disruptive accidents of a sodium-cooled fast reactor.
- e. An extended heat and mass transfer models were introduced to represent key thermal hydraulic behaviors.

2. In the study of melt freezing behavior, the simulation results reasonably reproduced observed penetration and freezing characteristics of not only molten metal (pure melt), but also its mixture with solid particles (mixed melt). Local melt freezing behaviors such as blockage formation due to melt adhesion on pin surface and their difference between pure and mixed melts were clarified by the present simulations. It is expected that the particle-based simulation for multicomponent, multiphase flows could be a powerful CFD tool to understand and clarify local thermal-hydraulic behaviors involved in core disruptive accidents of liquid-metal-cooled reactors.

The followings are some ideas for the future works:

1. The EAGLE-1 ID-1 test simulation, which starts from the pin disruption condition, should be performed. The present study did not consider the effects of molten material mixing caused by pin disruption. It is strongly recommended to introduce PMS model, which is developed to calculate the interaction effects between solid and fluid particles, in order to improve the simulation results, especially in treating solids phase during the pin disruption process. It is believed that this model and some other improvement will show better results than the present model in treating solid particles.

2. Validation on material mixture behavior should be performed. In the present study, material movement was simulated in case of effective viscosity model, while no material movement showed in Rheology model. It is necessary to consider an experimental model to validate its behavior in the future study.

3. The numerical instability should be solved more reasonably in the future calculation of ID-1 test. In order to reach numerical stability during the calculation, it is recommended to calculate the pressure calculations of two pools, molten pool and coolant pool, separately in the same time.

4. Further improvement on reproduce more reasonable melt separation behavior simulation observed in the mixed-melt freezing experiment.

## Acknowledgement

Finishing this PhD study has been one of the most significant academic challenges I have ever had to face. Without blesses from God that I grateful for, as well as support, patience and guidance of the following people, this study would not have been completed. It is to them that I owe my deepest gratitude.

- Prof. Koji Morita of Kyushu University who undertook to act as my supervisor despite his many other academic and professional commitments. His guidance, support, knowledge and commitment to the highest standards greatly inspired and motivated me.
- Prof. Yasuyuki Takata, Prof. Kazuya Idemitsu, and Prof. Hideaki Matsuura of Kyushu University for their willingness to act as my examination committee.
- Assistant Prof. Tatsuya Matsumoto of Morita Laboratory, Kyushu University who help in administrations
- Dr. Liancheng Guo, Dr. Bin Zhang and Dr. Cheng for helpful advices and discussions
- My colleagues, Oshima Wataru, Akihiro Morita, Xiaoxing Liu, Mr. Shamsuzaman, and other members for help, time and cooperation during my study as well as to Yuuya Nakamura, Tomoya Takeda, and Ichiro Miya for help and friendships in the beginning of my study and life in Japan.
- Ministry of Education, Culture, Sports, Science and Technology of Japan for the Monkakusho scholarship that cover all expenses during my life and study in Japan.
- Mr. Akira Yoshikai and his mother, Mrs. Junko Yoshikai, who support my Japanese study and treat me like their family during life in Japan. Their kindness



as well as the time we spent together will be a great memorable for me in the future.

- My friends in Japan, Prabha, Natsuki Yoshida, Damar, Liana, Mutia, Nana Yuda, Jin Chen for sweet friendship as well as to Bin Chen and Dr. Kaijiang Yu, who inspired me a lot of things related to the PhD program.
- My family for their patient, support and unlimited love that made me strong and live one of my dreams.

# Nomenclature

$A$	rheology parameter [ $K^{-1}$ ]
$a$	heat transfer area per unit volume [ $m^{-1}$ ]
$C_p$	specific heat capacity [ $J/(kg \cdot K)$ ]
$c_B$	model parameter for buoyancy [-]
$\vec{f}$	volumetric force [ $N/m^3$ ]
$\vec{f}_g$	gravity force per unit volume [ $N/m^3$ ]
$\bar{g}$	gravity [ $m/s^2$ ]
$H$	specific enthalpy [ $J/kg$ ]
$H_f$	specific latent heat of fusion [ $J/kg$ ]
$H_{liq}$	Specific enthalpy at liquidus point [ $J/kg$ ]
$h$	heat transfer coefficient [ $W/(m^2 \cdot K)$ ]
$h_{eff}$	effective heat transfer coefficient [ $W/(m^2 \cdot K)$ ]
$k$	thermal conductivity [ $W/(m \cdot K)$ ]
$k_f$	thermal conductivity of fuel [ $W/(m \cdot K)$ ]
$k_m$	thermal conductivity of mixture pool [ $W/(m \cdot K)$ ]
$k_s$	thermal conductivity of steel [ $W/(m \cdot K)$ ]
$L$	pool characteristic length for heat transfer [m]
$m$	mass [kg]
$n^0$	initial number density of particles [-]
$\bar{n}$	unit vector [-]
$p$	pressure [Pa]

$Q$	volumetric heat source [W/m <sup>3</sup> ]
$Q^h$	heat transfer rate per unit volume at interface [W/m <sup>3</sup> ]
$Q^m$	energy transfer rate per unit volume due to phase change [W/m <sup>3</sup> ]
$Q^n$	volumetric heat source due to nuclear heating [W/m <sup>3</sup> ]
$Q^I$	net heat flow rate at interface [W/m <sup>3</sup> ]
$q_{nucI}$	heat flux caused by nuclear heating [W/m <sup>2</sup> ]
$q_{wall}$	heat flux to duct wall [W/m <sup>2</sup> ]
$R$	radius of control volume [m]
$\vec{r}$	particle position [m]
$r_e$	cut-off radius [m]
$S$	surface of control volume [m <sup>2</sup> ]
$T$	temperature [K]
$T_0$	reference temperature [K]
$T^I$	interface temperature [K]
$T^N$	interface temperature without phase change [K]
$T_{liq}$	liquidus temperature [K]
$T_{sol}$	solidus temperature [K]
$t$	time [s]
$\vec{u}$	velocity [m/s]
$V$	control volume [m <sup>3</sup> ]

### **Greek Letters**

$\alpha$	volume fraction [-]
$\alpha_{max}$	maximum solid volume fraction [-]

$\beta$	volumetric thermal expansion coefficient [K <sup>-1</sup> ]
$\Delta l$	initial particle distance [m]
$\Delta S$	interaction surface [m <sup>2</sup> ]
$\Delta T$	temperature difference [K]
$\Delta t$	time step size [s]
$\delta$	crust thickness [m]
$\theta$	contact angle [-]
$\mu$	dynamic viscosity [Pa·s]
$\mu_{app}$	apparent dynamic viscosity [Pa.s]
$\mu_{max}$	maximum apparent dynamic viscosity [Pa.s]
$\rho$	density [kg/m <sup>3</sup> ]
$\sigma$	surface tension
$\Gamma_{freezing}$	freezing rate per unit volume [kg/(m <sup>3</sup> ·s)]
$\Gamma_{melting}$	melting rate per unit volume [kg/(m <sup>3</sup> ·s)]
$\phi$	arbitrary scalar function [-]
$\phi_{sur}$	function value on the surface of control volume [-]
$\omega$	kernel function [-]

### Subscripts

$i$	particle $i$
$ij$	between particles $i$ and $j$
$j$	particle $j$
$l$	liquid
$ls$	liquid-solid

<i>Liq</i>	liquidus
$M(i)$	material that constitutes of particle $i$
$n$	normal direction
$s$	solid
$sl$	solid-liquid
$sol$	solidus
$surf$	surface

## References

- Ajiz M. A. and Jennings A., A Robust Incomplete Choleski-Conjugate Gradient Algorithm, *Int. J. Numer. Meth. In Eng.*, Vol. 20, pp. 949-966 (1984)
- Aoto K. et al., Design Study and R&D Progress on Japan Sodium-Cooled Fast Reactor, *Journal of Nuclear Science and Technology*, 48, pp. 463-471 (2011).
- Clift R., Grace J.R. et al., *Bubbles, Drops, and Particles*, Academic Press, New York (1978).
- Charles D.F., *Nuclear Energy: What Everyone Needs to Know*, Oxford University Press, New York (2012).
- Carey Van P., *Liquid-Vapor Phase-Change Phenomena*, Second Edition, Taylor & Francis, New York (2008).
- Endo H., Kubo S. et al., Elimination of Recriticality Potential for the Self-Consistent Nuclear Energy System, *Prog. Nucl. Energy*, Vol.40, No.3/4, pp.577-586 (2002).
- Frankel N. A. and Acrivos A., On The Viscosity of A Concentrated Suspension of Solid Spheres, *Chemical Engineering Science*, Vol. 22, pp. 847-853 (1967).
- Gingold R.A., Monaghan J., Smooth Particle Hydrodynamics: Theory and Application to Non-spherical Stars, *Mon. Not. R. Astron. Soc.*, 181, pp. 375-89 (1977).
- Guo L. et al., Fundamental Validation of the Finite Volume Particle Method for 3D Sloshing Dynamics, *Int. J. Numer. Meth. Fluids*, 68(1), pp. 1-17 (2012).
- Guo L., Kawano Y. et al., Numerical Simulation of Rheological Behavior in Melting Metal Using Finite Volume Particle Method, *J. Nucl. Sci. Technol.*, Vol.47, No.11, pp. 1011-1022 (2010).
- Hossain M.K. et al., Experimental Study of Molten Metal Penetration and Freezing Behavior in Pin-Bundle Geometry, *J. Nucl. Sci. Technol.*, 46(8), pp. 163-174 (2009).

International Atomic Energy Agency (IAEA), Thermophysical Properties of Materials for Nuclear Engineering: A Tutorial and Collection of Data, Vienna, Austria, IAEA-THPH (2008).

Issa R. I., Solution of The Implicity Discretised Fluid Flow Equations by Operator-Splitting, J. Comp. Physics, Vol. 62, pp. 40-65 (1985).

Jose G., Energy: What Everyone Needs to Know, Oxford University Press, New York (2012).

Kamiyama K. et al., EAGLE Project: Experimental Study for Advanced Safety of Fast Reactors - Progress on the out-of-pile experiments and results of the melt discharge experiment -, JNC TY9400 2004-030, Japan Nuclear Fuel Cycle Development Institute report (2001), [in Japanese].

Kondo M. et al., Surface Tension Model using Inter-particle Force in Particle Method, FEDSM 2007 I Symposia (Part A), San Diego, USA, Jul. 30-Aug. 2, 2007, pp. 93-98 (2007).

Kondo Sa. et al., Phase 2 Code Assessment of SIMMER-III, A Computer Program for LMFR Core Disruptive Accident Analysis, Japan Nuclear Cycle Development Institute, Ibaraki, JNC TN9400 2000-105 (2000).

Konishi K., Kubo S. et al., The EAGLE Project to Eliminate the Recriticality Issue of Fast Reactors -Progress and Results of In-pile Tests-,” Proc. 5th Korea-Japan Symposium on Nuclear Thermal Hydraulics and Safety (NTHAS5), Jeju, Korea, Nov. 26-29, 2006, NTHAS5-F001 (2006).

Konishi K., Toyooka J. et al., Progress in Establishment of the Innovative Safety Logic for SFR Eliminating the Recriticality Issue with the EAGLE Experimental Program, Int. Scientific-Practical Conf. "Nuclear Power Engineering in Kazakhstan," Kurchatov, Kazakhstan, June 11-13 (2008).

- Konomura M, Severe Accident Countermeasures of SFR (on Monju), Proc. JAEA-IAEA International workshop on prevention and mitigation of severe accidents in sodium-cooled fast reactors, Tsuruga, June 11-13 (2012).
- Koshizuka S., Oka Y. Moving-particle Semi-implicit Method for Fragmentation of Incompressible Fluid, Nucl. Sci. Eng., 123, pp. 421-434 (1996).
- Kubo S. et al., Safety Design Requirements for Safety Systems and Components of JSFR, Journal of Nuclear Science and Technology, 48, pp. 547-555 (2011).
- Lee J., Lee S. et al., A Review of Thermal Conductivity Data, Mechanisms and Models for Nanofluids, Int. J. Macro-Nano Scale Transport, Vol.1, No.4, pp.269-322 (2010).
- Mahmudah R.S., Kumabe M. et al., 3D Simulation of Solid-Melt Mixture Flow with Melt Solidification Using a Finite Volume Particle Method," J. Nucl. Sci. Technol., Vol.48, No.10, pp. 1300-1312 (2011).
- Morita K., Development of Heat and Mass Transfer Model for Multiphase Multicomponent Flows in Reactor Safety Analysis, PhD Thesis, Kyushu University, Fukuoka (1998).
- Morita K. et al., Detailed Analyses of Key Phenomena in Core Disruptive Accidents of Sodium-cooled Fast Reactors by the COMPASS Code, Nucl. Eng. Des., 241(12), pp. 4672-4681 (2011).
- Rahman, M.M. et al., Experimental Investigation of Molten Metal Freezing on to a Structure, Exp. Thermal Fluid Sci., 32(1), pp. 198-213 (2007).
- Rahman M.M. et al., Simulation of Molten Metal Freezing Behavior on to a Structure, Nucl. Eng. Des., 238(10), pp. 2706-2717 (2008).
- Sato I., Tobita Y. et al., Safety Strategy of JSFR Eliminating Severe Recriticality Events and Establishing In-Vessel Retention in the Core Disruptive Accident, J. Nucl. Sci. Technol., Vol.48, No.4, pp.556-566 (2011).



- Shirakawa N., Yamamoto Y. et al., Analysis of Subcooled Boiling with the Two-Fluid Particle Interaction Method, J. Nucl. Sci. Technol., Vol.40, No.3, pp.125-135 (2003).
- Sofu T., Importance of Passive Safety and Role of Monju for The Future SFRs, Proc. JAEA-IAEA International workshop on prevention and mitigation of severe accidents in sodium-cooled fast reactors, Tsuruga, June 11-13 (2012).
- Sonar M. et al., Particle Effects on Penetration and Solidification of Flowing Mixed Melts on Metal Structures, J. Nucl. Sci. Technol., 48(8), pp. 1214-1222 (2011a).
- Sonar M. et al., Experimental Investigation of Solid-liquid Mixtures Freezing Behavior in Flow Channels, Nucl. Eng. Des., 241(10), pp. 4223-4235 (2011b).
- Sonar M. et al., Simulation of Solid-Liquid Multiphase Flows with Fuel Relocation and Freezing Behavior in Pin Bundle Geometry, 19th Int. Conf. on Nucl. Eng., Osaka, Japan, Oct. 24-25, ICONE19-43982 (2011c).
- Takeda T. et al., Review of Safety Improvement on Sodium-Cooled Fast Reactors after Fukushima Accident, Natural Science, Vol.4, Special Issue, pp. 929-935 (2012).
- Tobita Y. et al., The Development of SIMMER-III, an Advanced Computer Program for LMFR Safety Analysis, Joint IAEA/NEA Technical Meeting on the Use of Computational Fluid Dynamics Codes for Safety Analysis of Reactor Systems, Including Containment, Pisa, Italy, Nov. 11-14 (2002).
- Toyooka J., Endo H. et al., A Study on Mechanism of Early Failure of Inner Duct Wall within Fuel Subassembly with High Heat Flux from Molten Core Materials based on Analysis of an EAGLE Experiment Simulating Core Disruptive Accidents in an LMFBR, Transactions of the Atomic Energy Society of Japan, Vol.12, No.1, pp.50-66 (2013), [in Japanese].
- Toyooka J., Kamiyama K. et al., SIMMER-III Analysis of EAGLE-1 In-pile Tests Focusing on Heat Transfer from Molten Core Material to Steel-Wall Structure, Proc.

- 7th Korea-Japan Symposium on Nuclear Thermal Hydraulics and Safety (NTHAS7),  
Chuncheon, Korea, Nov. 14-17, N7P0058 (2010).
- Wang Q. et al., Efficient rendering of breaking waves using MPS method, Journal of  
Zhejiang University SCIENCE A, 7(6), pp. 1018-1025 (2006).
- Xiao F. et al., An Algorithm for Simulating Solid Objects Suspended in Stratified Flow,  
Comput. Phys. Commun., 102(1-3), pp. 147-160 (1997).
- Yabushita K., Hibi S., A Finite Volume Particle Method for an Incompressible Fluid  
Flow, Proc. Comput. Eng. Conf., Vol.10, pp.419-421 (2005), [in Japanese].
- Zhang S., Morita K. et al., A New Algorithm for Surface Tension Model in Moving  
Particle Methods, Int. J. Numer. Methods in Fluid, Vol.55, No.3, pp.225-240 (2007).
- Zhang S., Development of Moving Particle Methods for Computational Fluid Dynamics,  
Ph.D. thesis, Kyushu University (2006).